

Organization principles of the embryonic cell cycle in *Drosophila melanogaster*

by

Victoria E. Deneke

Department of Cell Biology
Duke University

Date: _____

Approved:

Stefano Di Talia, Supervisor

Blanche Capel

Daniel J. Lew

Daniel P. Kiehart

Dissertation submitted in partial fulfillment of
the requirements for the degree of Doctor
of Philosophy in the Department of
Cell Biology in the Graduate School
of Duke University

2019

ABSTRACT

Organization principles of the embryonic cell cycle in *Drosophila melanogaster*

by

Victoria E. Deneke

Department of Cell Biology
Duke University

Date: _____

Approved:

Stefano Di Talia, Supervisor

Blanche Capel

Daniel J. Lew

Daniel P. Kiehart

An abstract of a dissertation submitted in partial
fulfillment of the requirements for the degree
of Doctor of Philosophy in the Department of
Cell Biology in the Graduate School of
Duke University

2019

Copyright by
Victoria Eugenia Deneke Santana
2019

Abstract

Early development in most metazoans is characterized by remarkably fast and coordinated cell cycles. Nonetheless, it is unclear what organizational principles underlie cell cycle synchronization across a large developing embryo. We found that cell cycle synchronization in *Drosophila* arises through the self-organized positioning of nuclei, which is regulated by the spatiotemporal dynamics of the cell cycle, cortical contractions, and cytoplasmic streaming. First, local cyclin-dependent kinase 1 (Cdk1) downregulation at mitotic exit initiates the damped spreading of protein phosphatase 1 (PP1) activity, which is responsible for recruiting myosin II to cortical regions that surround the nuclei, where gradients of contractility are generated. These gradients drive cortical and cytoplasmic flows that properly position the nuclei across the embryo. Uniform positioning of nuclei across the embryo is required for the emergence of synchronous cell cycles. Once at the surface of the embryo, nuclei undergo four metachronous cell cycles, which spread in a wave-like manner with remarkable speed across the large distance of the egg. Using a Cdk1 biosensor, we found that travelling waves of Cdk1 activity propagate through the embryo and synchronize the cell cycle during S-phase through an active mechanism, while mitotic events simply follow S-phase synchronization with a delay. Taken together, a self-organized mechanism that spreads nuclei uniformly is required early on in development to give rise to

synchronous divisions. Cell cycle synchrony is then maintained by waves of Cdk1 activity, ensuring that all nuclei initiate the mid-blastula transition simultaneously. This work highlights the importance of chemical waves and cytoplasmic flows in the spatiotemporal regulation of the cell cycle of large embryos.

Contents

Abstract	iv
List of Tables	xi
List of Figures	xii
Dedication	xiv
Acknowledgements	xv
1. Introduction: Uncovering new organization principles in cell biology	1
1.1 A brief history of organization principles in biology	1
1.2 Chemical waves as an organization mechanism in biology	2
1.2.1 Theoretical framework of chemical waves	4
1.2.1.1 <i>Active and phase waves</i>	5
1.2.1.2 <i>Mathematical types of waves: Unstable, bistable, and excitable</i>	8
1.2.1.3 <i>Measuring chemical waves in biological systems</i>	13
1.2.2 Bistable and excitable waves in the regulation of the cell cycle, cytokinesis, and cell motility	14
1.2.2.1 Mitotic waves	14
1.2.2.2 Chemotaxis, cell migration and mechanical waves	20
1.2.3 Chemical waves in other developmental and physiological contexts	23
1.2.3.1 Waves of gene expression in the formation of somites	23
1.2.3.2 Waves in blood coagulation	28
1.2.3.3 Waves in patterning cell cycle and cell differentiation in <i>Drosophila</i>	29
1.3 Cytoplasmic flows as an organization mechanism in biology	30

1.4 Summary of the work included in this dissertation	31
2. Waves of Cdk1 activity in S-phase synchronize the cell cycle in <i>Drosophila</i> embryos ..	32
2.1 Summary.....	32
2.2 Introduction.....	33
2.3 Results	38
2.3.1 Visualization and quantification of Cdk1 and mitotic waves.....	38
2.3.2 Cdk1 activity during S-phase is predictive of mitotic and Cdk1 wave speed at cycles 12 and 13.....	43
2.3.3 Cdk1 activity during S-phase is predictive of mitotic and Cdk1 wave speed at cycles 12 and 13.....	46
2.3.4 A Cdk1/Chk1 double negative feedback controls Cdk1 waves.....	49
2.3.5 Mitotic switch ensures rapid activation of Cdk1 during mitosis but does not regulate S-phase Cdk1 activation rate	53
2.3.6 A new physical mechanism for the generation of waves captures the properties of Cdk1 waves.....	57
2.3.7 S-phase waves are generated by an active mechanism, while anaphase waves are a kinematic and passive process	60
2.4 Discussion.....	64
2.4.1 Cell cycle synchronization through chemical waves of Cdk1 activity	64
2.4.2 Quantitative analysis of chemical waves during embryonic development.....	68
2.5 Experimental Methods.....	69
2.5.1 Plasmids.....	69
2.5.2 Stocks.....	70
2.5.3 Microscopy	71

2.5.4 FRAP experiments.....	72
2.5.5 Validation and characterization of Cdk1 FRET sensor	72
2.5.6 Data and image analysis.....	73
2.5.7 Computational method to calculate Cdk1 and mitotic wave speeds	73
2.5.8 Embryo manipulations	74
2.5.9 Production of dsRNA	75
3. Self-organized nuclear positioning synchronizes the cell cycle in <i>Drosophila</i> embryos	76
3.1 Summary.....	76
3.2 Introduction.....	77
3.3 Results	83
3.3.1 Nuclei provide a spatial landmark for the oscillations of Cdk1 and PP1	83
3.3.2 The dynamics of the cell cycle oscillator is characterized by a graded distribution of PP1 activity.	87
3.3.3 Local PP1 activity couples nuclear and cortical dynamics by regulating cortical myosin II recruitment.	91
3.3.4 Myosin II gradients drive cortical contractions	96
3.3.5 Nuclear movements correlate with cytoplasmic flows.....	102
3.3.6 Optogenetic control of Rho signaling shows that cytoplasmic flows and nuclear movements are mainly driven by cortical contractions.....	109
3.3.7 Viscous dynamics captures the large-scale features of cytoplasmic flows	115
3.3.8 Proper nuclear positioning is required for synchronous cell cycles	118
3.4 Discussion.....	125
3.5 Experimental Methods.....	129

3.5.1 Experimental Model and Subject Details	129
3.5.2 Method Details.....	131
3.5.2.1 Embryo Manipulations	131
3.5.2.2 Microscopy.....	131
3.5.2.3 Production of <i>endos^{S68D}</i> and <i>I-2</i> mRNA.....	133
3.5.3 Quantification and Statistical Analysis	134
3.5.3.1 Image analysis	134
3.5.3.2 Identification of the phosphatase regulating the FRET biosensor	134
3.5.3.3 Quantification of the Cdk1/PP1 biosensor	135
3.5.3.4 Quantification of cortical and cytoplasmic flows.....	136
3.5.3.5 Validation of cortical and bulk cytoplasmic flow measurements.....	137
3.5.3.6 Prediction of cortical velocity from myosin gradients.....	139
3.5.3.7 Cytoplasmic F-actin and myosin II dynamics	141
3.5.3.8 Characterization of shackleton mutant.....	141
3.5.3.9 Analysis of traveling waves of Cdk1/PP1 activity	142
3.5.3.10 Statistical analysis	144
4. Conclusions: Chemical waves and cytoplasmic streaming as emerging self-organizing principles in cell and developmental biology	145
4.1 Summary.....	145
4.2 Future Directions	149
4.2.1 Dissect the mechanisms regulating cell cycle synchrony in early syncytial blastoderm.....	149
4.2.2 Dissect the mechanisms of regulation of contractility by the cell cycle.....	150

4.2.3 Dissect the self-organizing principles of nuclear positioning	151
4.2.4 Dissect the physical properties of cytoplasmic flows.....	152
4.2.5 Dissect the role of cytoplasmic flows on morphogen gradient formation and patterning	153
4.3 Perspectives	153
4.3.1 Chemical waves as a general strategy to organize cellular dynamics in space and time	153
4.3.2 The role of cytoplasmic flows in cellular and tissue organization	156
References	158
Biography	173

List of Tables

Table 1: Summary of physical parameters of key examples of chemical waves in biology	4
Table 2: List of stocks used in this Chapter	71
Table 3: Key Resources used in this Chapter	129

List of Figures

Figure 1: Sending biochemical signals in cells through chemical waves.	3
Figure 2: Active versus phase waves.	8
Figure 3: Unstable, bistable and excitable waves.	10
Figure 4: Examples of bistable and excitable chemical waves in biology.	16
Figure 5: Additional examples of chemical waves in biological systems.	25
Figure 6: Cdk1 waves drive mitotic waves.	40
Figure 7: Validation of the Cdk1 FRET sensor and computational method to calculate wave speed.	43
Figure 8: Cdk1 activity during S-phase is predictive of mitotic and Cdk1 wave speed. ...	44
Figure 9: PCNA-TagRFP as a marker of completion of S-phase.	45
Figure 10: Cdk1 waves are dependent on the Chk1/Wee1 pathway and on DNA content.	48
Figure 11: A Cdk1/Chk1 double negative feedback controls Cdk1 waves.	52
Figure 12: Validation of the Chk1 sensor.	53
Figure 13: Mitotic switch ensures rapid activation of Cdk1 during mitosis but does not regulate S-phase Cdk1 activation rate.	55
Figure 14: Positive feedback from the Cdk1 mitotic circuit regulates abruptness of Cdk1 activation.	56
Figure 15: Spatiotemporal patterns of Cdk1 activity differ in wild type and mutants of the mitotic switch.	58
Figure 16: Bistable waves are slow compared to sweep waves.	59
Figure 17: The dynamics of Cdk1 over a single cell cycle display three distinct phases. .	60
Figure 18: Mitotic waves are kinematic phase waves.	63

Figure 19: The rate of inactivation of Cdk1 during anaphase does not change during development.	64
Figure 20: Nuclei provide a spatial landmark for the oscillations of Cdk1 and PP1.....	80
Figure 21: Identification of PP1 as the phosphatase driving dephosphorylation and spatiotemporal dynamics of the Cdk1/PP1 biosensor.	85
Figure 22: The dynamics of the cell cycle oscillator is characterized by a graded distribution of PP1 activity.	89
Figure 23: Biosensor dynamics near the surface of early embryos is regulated by PP1 activity rather than Cdk1.	89
Figure 24: Local PP1 activity couples nuclear and cortical dynamics by regulating cortical myosin II recruitment.	93
Figure 25: Quantification of myosin II, F-actin and Rho activities in early development.	96
Figure 26: Myosin II gradients drive cortical contractions.....	99
Figure 27: Prediction of cortical velocity from myosin II gradients and quantification of gradients and cortical flows in PP1-heterozygous embryos.....	101
Figure 28: Cytoplasmic flows in wild type and PP1-heterozygous embryos.....	106
Figure 29: Nuclear movements correlate with cytoplasmic flows.	109
Figure 30: Optogenetic control of Rho signaling shows that cytoplasmic flows and nuclear movements are mainly driven by cortical contractions.	112
Figure 31: Optogenetic RhoGEF2-CRY2 recruitment to plasma membrane drives myosin II cortical accumulation upon blue light illumination.....	113
Figure 32: Proper nuclear positioning is required for synchronous cell cycles.	121
Figure 33: <i>shackleton</i> controls nuclear spreading without affecting the cell cycle; characterization of traveling waves of Cdk1/PP1 activity in early embryos.....	124

Dedication

“And above all these put on love,
which binds everything together in perfect harmony.”

Colossians 3:14 (English Standard Version)

“Y sobre todas estas cosas vestíos de amor, que es el vínculo perfecto.”

Colosenses 3:14 (Reina Valera 1960)

To my spiritual family, who has sustained me through their love and prayers.

Para mi familia espiritual, quien me ha sostenido por medio de su amor y sus
oraciones.

Acknowledgements

“I will give thanks to the Lord with my whole heart;

I will recount all of your wonderful deeds.”

Psalm 9:1 (English Standard Version)

“Te alabaré, oh Jehová, con todo mi corazón;

Contaré todas tus maravillas.”

Salmo 9:1 (Reina-Valera 1960)

Graduate School has been one of the most challenging and yet most fulfilling experiences for me. I was able to have such an enriching experience thanks to the help and guidance of many people, who I would like to acknowledge in this section.

First, I would like to thank God for blessing me in ways that I could have never imagined. For opening doors for me to be here and for giving me the abilities to obtain this degree. Lastly, for acting through people all around me to motivate me to keep going, especially during the toughest times.

Thank you, Stefano, for all your help and support during these last 5 years. For challenging me intellectually, for your incredible dedication to teach me the necessary skills to become a good scientist, for encouraging me to apply to many scientific

opportunities, for introducing me to many scientists in the field and giving me the opportunity to tell them about my work, and for supporting my engagement in activities outside of lab. It has been an honor to be one of the first trainees of the Di Talia lab. I will cherish every moment I spent in the lab and use the skills that I learned here in my future endeavors.

I'd also like to thank the past and present members of the Di Talia lab for making our lab experience an intellectually stimulating and fun environment. This has been a great group of people to work with and I would like to thank each one of you individually:

Thank you, Anna, for teaching me everything I know about fruit fly genetics as well as giving me advice on molecular biology experiments and always being so helpful and happy to help me out. The reason why half of our lab photos are cake photos is because Anna makes the most amazing cakes and she puts a great deal of care and love into each of them. Thank you, Anna, for all of your love and support.

Patrick, thank you for dressing up as a Cdk1 FRET sensor with me. That was amazing! And that just really shows the friendly and cheerful disposition that characterizes you. Thanks for always keeping the lab fun.

Woon, thank you for teaching me how to do everything in a better way: from image analysis to embryo injections, it amazes me how well you optimize everything you work on. Also, for always giving me advice on technological gadgets and for

helping me with the live stream of my defense. I don't know what I would have done without you.

Ben, thank you for being my lab sibling from day 1. Thanks for interviewing me for your radio station and for baking scones for us. It has been great to go through the different stages of Grad School together with another person in the same lab.

Alessandro, thank you for teaching me Italian and actively discussing scientific ideas with me.

Luke, I admire how efficient you are in lab. Thank you for showing me that it is actually possible to have a balanced work life schedule. Also, thank you for your thoughtful insights during lab meeting and during journal club. It has been amazing to work with you and learn from you.

Maya, thank you for showing me how to have grit in Grad School. For getting through your second year of grad school managing the hardest courses and yet being very productive in lab. Thank you for always coming to chat with me to get a break from work. It has been really awesome to get to know you.

To all my mentees throughout Grad School: thank you for working with me and for being so patient! Maggie Xing, thank you for all your help with imaging and for your cheerful disposition. Best wishes to you in Med School! Belanie Nagiel, thank you for all your help with image analysis! This was such a new experience for you and I'm happy I was able to introduce you to the world of biology for a few months. Thanks for your

patience and for your amazing work. Sruthi Valluru, thank you for coming to work with us for a summer! I admire your enthusiasm and energy and hope it carries you through college and potentially Grad School! Briana Davis: I'm so proud of you! You're such a motivated and talented scientist, I know you'll be able to achieve whatever you set your mind to. It has been an honor to be your mentor and your friend, can't wait to see how your professional career evolves! And finally, thank you to my sister Gisi! For spending a summer in our lab and teaching yourself MATLAB. You are one of the brightest and most independent young adults I have ever met. I'm so proud of you for following your true interests, regardless of what others might say. Keep doing that, you'll end up in a good place!

I'd also like to thank my previous mentors who have helped me get to Grad School and have encouraged me throughout the way. Thank you, Mr. Amadeo Cortés, for motivating me to study science and math and for constantly giving me advice and book recommendations. Thank you, Dr. Karen Cowden Dahl, for introducing me to the world of research and for patiently teaching me the scientific method, even though I had no previous experience before joining your lab. Thank you for always believing in me and serving as a role model for me. Thank you, Dr. Joanne Richards and Dr. Yi Ren, for mentoring me during my summer at Baylor College of Medicine. For being inspiring female scientists with a true love for science.

Thank you to all of my friends that I've made throughout my time at Duke. You all have been so instrumental to me and have taught me so many things. I'd like to highlight a few people:

Maria, thank you for flying all the way from New York City to be present at my defense. I appreciate your friendship so much and it has been so nice to have such a successful scientist friend to go through Grad School with. Thank you for all your advice and for all your positive support throughout this adventure!

Sydney, thank you for being so fun and for your personalized gifts. You have made Grad School easier to go through by celebrating each milestone along the way. Thank you for always being there.

Jesse and Alice, thank you for being the best roommates this year. It has been so much fun to share this past year with you both and I'm so happy you could share this experience with me.

Gizem, thank you for teaching me what true friendship is all about. For sharing good and bad times and learning how to grow from each opportunity life gives to you.

Kwaby, thank you for your vision. For always passionately discussing science with me and for your amazing ability to always put things in a different or unique perspective. I have learned so much from you and I appreciate the time we were able to share here at Duke.

Monica, thank you for recruiting me to Duke! For being my Latina mentor and helping me through Grad School. And Jamie, thank you for showing me how to be resilient and how to stay motivated, fit and healthy throughout Grad School.

And to everyone else who I don't have time to acknowledge individually. I have learned something from each one of you and my experience at Duke has been enriched by you.

I'd also like to thank Duke BioCoRE and the Office of Biomedical Graduate Diversity led by Sherilynn Black. I was given the opportunity to be part of the first cohort of BioCoRE scholars and the community that BioCoRE and OBGD built was invaluable to me. They provided support during the major milestones in Grad School and have always been there for us. Thank you, Sherilynn, and BioCoRE administrators for building this amazing community at Duke.

I'd also like to thank Duke INSPIRE, which is a student group that we started with Kwaby and Aaron during our first year of Grad School. INSPIRE has now become a space where grad students can come and talk about science or any other topic that really interests us. This group was instrumental to my development here at Duke and I'm grateful for the support we've received from faculty and administration to keep nurturing this group through the years.

I am very grateful to all the funding agencies that have supported my research and my professional development. Thank you to the Howard Hughes Medical Institute,

for supporting a phenomenal fellowship dedicated specifically to international students and for giving us the opportunity to attend an HHMI Science Meeting, which was of immense value to me. Thank you, Schlumberger Foundation, for supporting women from developing countries like El Salvador, to accomplish our academic dreams and for supporting our outreach activities in our respective home countries to encourage young women to become rising leaders in STEM. Also, for building a network of strong women from all over the world from whom I have learned so much and I continue to be inspired by day by day. Thank you, Boehringer Ingelheim, for funding the research collaboration with the De Renzis lab at EMBL Heidelberg. That experience was one of the most enriching experiences during my Graduate School career and it would have not been possible without the opportunities that were provided by this funding agency.

Last but not least, I'd like to thank my family. For supporting me throughout this journey even though they had no idea why I would spend five years of my life studying fruit flies. My parents have taught me how to have strength in the face of adversity. My older sister, Ana, is my best friend and my biggest cheerleader. She's also the mother of my adorable niece Nina, who was only 6 months when I graduated from undergrad and is now 6 years old. My sister Sofi designed the poster for my defense and has designed many cover images that we have submitted to scientific journals. She also designed the current CMB logo. My youngest sister, Gisi, was able to attend my defense, spending her first college spring break to be here celebrating with me. Finally, I'd like to thank my

extended family and my church family, for always keeping me in their thoughts and prayers.

1. Introduction: Uncovering new organization principles in cell biology

Chapter 1 was partly modified from a review article titled: “Chemical waves in cell and developmental biology” published in *J. Cell Biol.*, 217 (4) 1193-1204 (2018). doi: 10.1083/jcb.201701158. The authors were Victoria E. Deneke and Stefano Di Talia.

1.1 A brief history of organization principles in biology

One of the greatest challenges in biological systems is to determine how dynamic organization emerges in cells and tissues. Over the past few decades, cell and molecular biologists have characterized the molecules that make up a cell and more recently have started to study the dynamics of such molecules. As new technological advances allow biologists to better visualize the dynamical processes in living systems, the field is now able to address how complex biological processes emerge from the dynamics and interactions of individual molecules.

General principles of organization were first developed from studies in physics and chemistry in the early to mid-20th century. In 1937, two independent articles were published which mathematically showed how an advantageous allele could spread dynamically through a population (Fisher, 1937; Kolmogorov, 1991). Importantly, these studies showed that in theory, organization could arise by simply coupling diffusion to a set of reactive processes. These mathematical descriptions later became the basis of many biologically-relevant models now known as reaction-diffusion systems. In

addition to mathematical descriptions of emerging biological organization, in the 1950s, Boris Belousov discovered a chemical system that showed regular oscillations which resulted in visible spatiotemporal color patterns in the media (Belousov, 1958). This chemical reaction is known as the Belousov-Zhabotinsky reaction (Belousov, 1958; Zhabotinsky, 1964), and provided experimental evidence that a chemical reaction far from equilibrium could give rise to patterns. Finally, during the same time period, mathematician Alan Turing proposed that morphogenesis of an organism could be explained by molecules that diffuse and react together such that they generate patterns of chemical concentrations (Turing, 1952). Together, these studies laid the foundation for future work on the emergence of dynamic organization in biological systems.

Many studies keep revealing new mechanisms by which a group of individual molecules or agents can interact to give rise to a spatiotemporal coordination or organization (Karsenti, 2008). In this chapter, I will focus on two biophysical mechanisms that have been shown to coordinate collective dynamics and are major themes in my Ph.D. work: chemical waves and cytoplasmic flows.

1.2 Chemical waves as an organization mechanism in biology

Chemical waves arise from biochemical activities that diffuse over short distances and trigger rapid activation in neighboring regions via positive feedback (Gelens et al., 2014; Ishihara et al., 2014; Tyson and Keener, 1988; Winfree, 1972). The coupling of diffusion and positive feedback enables chemical waves to spread a signal

rapidly and maintain their amplitude as they travel (Figure 1A-C). Classical examples of chemical waves in biology are the propagation of action potentials in neurons, and calcium waves after fertilization in early embryos and during heart contractions (Bers, 2002; Hodgkin and Huxley, 1952; Stricker, 1999). The speed and range over which chemical waves operate highlights their potential to promote rapid communication. A list of the physical parameters that have been measured for numerous examples of chemical waves in biology is summarized in Table 1. Recent advances in imaging technologies and quantitative, interdisciplinary approaches have resulted in numerous new examples that further illustrate the importance of chemical waves as an essential means of communication in biological systems. In this section, I will provide a conceptual and theoretical introduction to chemical waves, as well as recent examples detailing the role of chemical waves in embryogenesis, cell motility, and wound healing.

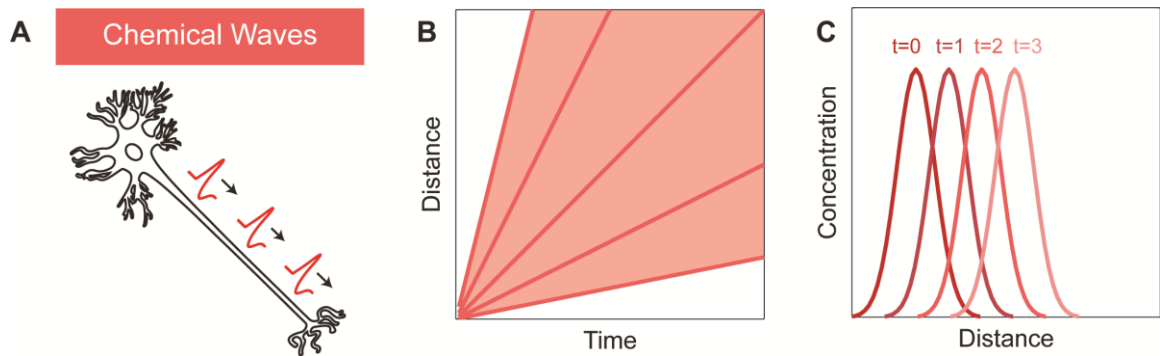


Figure 1: Sending biochemical signals in cells through chemical waves. A) Chemical waves are the basis by which action potentials can rapidly spread signals through a neuron. Depicted is a traveling action potential. B) Distanced traveled as a function of time by chemical waves. C) Propagation of the concentration profile of a biochemical signal by chemical waves. Diffusive transport dampens signal, whereas chemical waves preserve the amplitude of the traveling signal.

Table 1: Summary of physical parameters of key examples of chemical waves in biology

<i>System</i>	<i>Traveling activity</i>	<i>Estimated Diffusion</i>	<i>Wave speed</i>
<i>Xenopus extract cell cycle (Chang and Ferrell, 2013)</i>	Cdk1	10 $\mu\text{m}^2/\text{s}$	1 $\mu\text{m}/\text{s}$
<i>Starfish and Xenopus cytokinesis (Bement et al., 2015)</i>	Rho	$\sim 0.03\text{-}1 \mu\text{m}^2/\text{s}$	$\sim 0.2 \mu\text{m}/\text{s}$
<i>Drosophila syncytial cell cycles (Deneke et al., 2016)</i>	Cdk1	5 $\mu\text{m}^2/\text{s}$	2-6 $\mu\text{m}/\text{s}$
<i>Chemotaxis (Yang et al., 2016)</i>	Cdc42	$\sim 0.1\text{-}20 \mu\text{m}^2/\text{s}$	1 $\mu\text{m}/\text{s}$
<i>Actin waves (Weiner et al., 2007)</i>	Hem1	$\sim 0.5 \mu\text{m}^2/\text{s}$	3-5 $\mu\text{m}/\text{s}$
<i>Wound healing (Hiratsuka et al., 2015)</i>	ERK	$\sim 1 \mu\text{m}^2/\text{s}$	$\sim 0.02 \mu\text{m}/\text{s}$
<i>Growing epithelial culture (Serra-Picamal et al., 2012)</i>	Mechanical Stress	NA	$\sim 0.02 \mu\text{m}/\text{s}$
<i>Somitogenesis (Lauschke et al, 2013; Oates et al., 2012)</i>	Notch signaling	NA	$\sim 0.02 \mu\text{m}/\text{s}$
<i>Blood clotting (Dashkevich et al., 2012)</i>	Thrombin	$\sim 85 \mu\text{m}^2/\text{s}$	$\sim 0.6 \mu\text{m}/\text{s}$
<i>Eye imaginal disc (Roignant and Treisman, 2009)</i>	Dpp	$\sim 0.1\text{-}20 \mu\text{m}^2/\text{s}$	$\sim 10^{-3} \mu\text{m}/\text{s}$

1.2.1 Theoretical framework of chemical waves

Biological systems have an inherently dynamic nature: molecules are constantly reacting and diffusing. This dynamic behavior is captured by reaction-diffusion

equations, which can reproduce a wide range of processes, including traveling chemical waves and self-organizing patterns (Murray, 2002). Reaction-diffusion behaviors like self-patterning Turing systems (Turing, 1952), in which repeated patterns (e.g. stripes and spots) arise from the spatiotemporal interplay of activators and inhibitors in chemical pathways, have been reviewed elsewhere (Kondo and Miura, 2010; Meinhardt, 1982). Here, we focus on the distinction between active and passive waves and on the theoretical principles underlying the properties of different classes of waves.

1.2.1.1 *Active and phase waves*

In reaction-diffusion systems, diffusion generates mixing of molecules in space. Such mixing, when coupled to chemical reactions that rapidly amplify signals, can result in traveling waves of biochemical activities (Gelens et al., 2014; Tyson and Keener, 1988). Consider a large cell with inactivated proteins that are uniformly distributed. A pool of these proteins gets activated on one side of the cell through a phosphorylation event. For example, in the mitotic regulation of *Xenopus* egg extracts, inactive Cyclin-dependent kinase 1 (Cdk1) is believed to be first activated at the centrosome (Ishihara et al., 2014; Jackman et al., 2003), while in *Drosophila* embryos this activation happens at the poles (Deneke et al., 2016; Foe and Alberts, 1983). Activated Cdk1 can diffuse from the centrosome to neighboring regions. Furthermore, the reaction dynamics of Cdk1 is such that its activation leads to the catalytic activation of neighboring inactive Cdk1 through positive feedback (Morgan, 2007). The combination of local diffusion and the amplifying

signaling network can lead to a traveling wave of activation of Cdk1 throughout the extract or embryo (Chang and Ferrell, 2013; Deneke et al., 2016; Ishihara et al., 2014; Novak and Tyson, 1993). Waves of this nature are considered active waves and the central questions when studying such waves are identifying the molecules involved and dissecting the reaction kinetics necessary to drive the initiation and propagation of chemical waves.

Wave-like patterns do not necessarily indicate that there is a traveling chemical wave. For example, it is possible for a field of cells to be “pre-patterned” in such a way that individual cells will trigger some biochemical activity at a time determined by some internal timer. The internal timers could be set such that cells at one end of the field trigger first, and then their neighbors trigger a little later, and so on until cells at the other end of the field trigger last. A sensor for the biochemical activity would detect that activity apparently propagating from one end of the field to the other, in a manner indistinguishable from a traveling wave. Such apparent waves are called phase waves or kinematic waves, but are based on a pre-existing pattern of timer settings rather than a propagating signal as in traveling waves (Winfree, 2001). Such waves have been proposed as mechanisms to explain waves of gene expression in somitogenesis, the anaphase wave following the active mitotic entry wave in *Drosophila* embryos (see Chapter 2) and embryonic patterning of the short-germ beetle *Tribolium castaneum* by the Caudal morphogen gradient (El-Sherif et al., 2014). The difference between active waves

and phase waves is the first fundamental question that needs to be addressed when determining the mechanisms of wave-like spreading in biological contexts. The mechanisms can be distinguished by introducing a physical (diffusion) barrier within the system. Active waves cannot proceed past a barrier, so the two physically uncoupled compartments would become uncoordinated (Figure 2A). By contrast, if a phase wave is pre-patterned by the delays introduced by a previous chemical activity then the wave-like propagation would be unperturbed by the presence of the diffusion barrier (Figure 2B).

Chapter 2 of this dissertation will delve into several types of waves. I would like to briefly define the wave terms used:

Trigger waves are bistable waves (see below for mathematical description) that are characterized by two stable states and arise by the coupling of diffusion and positive feedback. Bistable waves have a characteristic travelling front that propagates through space and exhibits two stable states. Bistable waves are active waves that are impeded upon introduction of a diffusion barrier.

Sweep waves are characterized by a sweeping activity profile over time. They are composed of 3 phases and can spread faster than trigger/bistable waves. Phase I of sweep waves involves diffusion and therefore is also considered an active wave. Introduction of a barrier during Phase I of a sweep wave prevents the wave to propagate through the barrier.

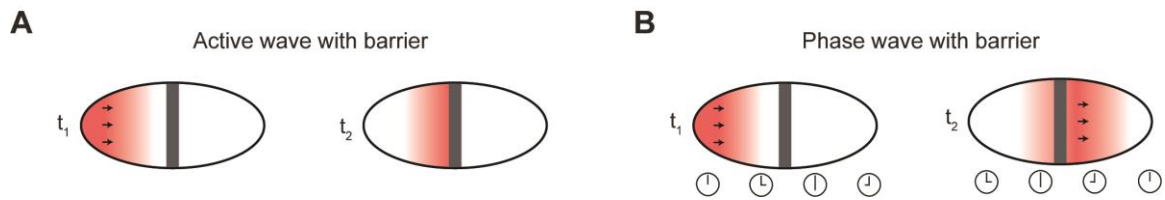


Figure 2: Active versus phase waves. Introduction of a physical barrier in a tissue/embryo allows the distinction between an active (A) and a phase wave (B).

1.2.1.2 Mathematical types of waves: Unstable, bistable, and excitable

Chemical waves can have many types of reaction dynamics and these determine the physical properties of the wave. They fall under three major mathematical classes: unstable waves, bistable waves, and excitable waves (Murray, 2002; van Saarloos, 2003). These three wave types can be distinguished mathematically by analyzing the concentration dynamics of a key regulator in the system.

Unstable waves arise in systems that are initially in a state where any small fluctuation will shift them towards a more stable state. These unstable systems can be intuitively understood by models of population growth. In these models, a population will first grow exponentially when few individuals are present and eventually will slow down and reach its carrying capacity. Mathematically, the population dynamics can be described by a logistic growth equation which produces an S-shaped curve. The most notable example of unstable waves are Fisher-Kolmogorov waves which were first used by Fisher in 1937 to describe the spatial spreading of an advantageous allele through a population (Fisher, 1937; Kolmogorov, 1991). Advantageous alleles can diffuse to neighboring regions, start growing exponentially in these regions and thereby spread in

a wave-like pattern (Figure 3A-C). Fisher-Kolmogorov waves have found wide applications in population genetics and social studies, where they have been used to describe gene drives, the spreading of farming throughout Europe (Figure 3C) and migratory waves of people in the United States (Ammerman and Cavalli-Sforza, 1971; Baggaley et al., 2012; Tanaka et al., 2017). Nonetheless, the importance of unstable waves in cell and developmental biology remains unclear. In principle, unstable waves would be very sensitive to noise, which can easily drive a system away from the unstable point and randomly initiate wave propagation. A possible way by which cellular pathways could use unstable waves more accurately is by the regulated activation of a pathway that causes a stable state to become unstable, thereby achieving control of the spreading of an unstable wave.

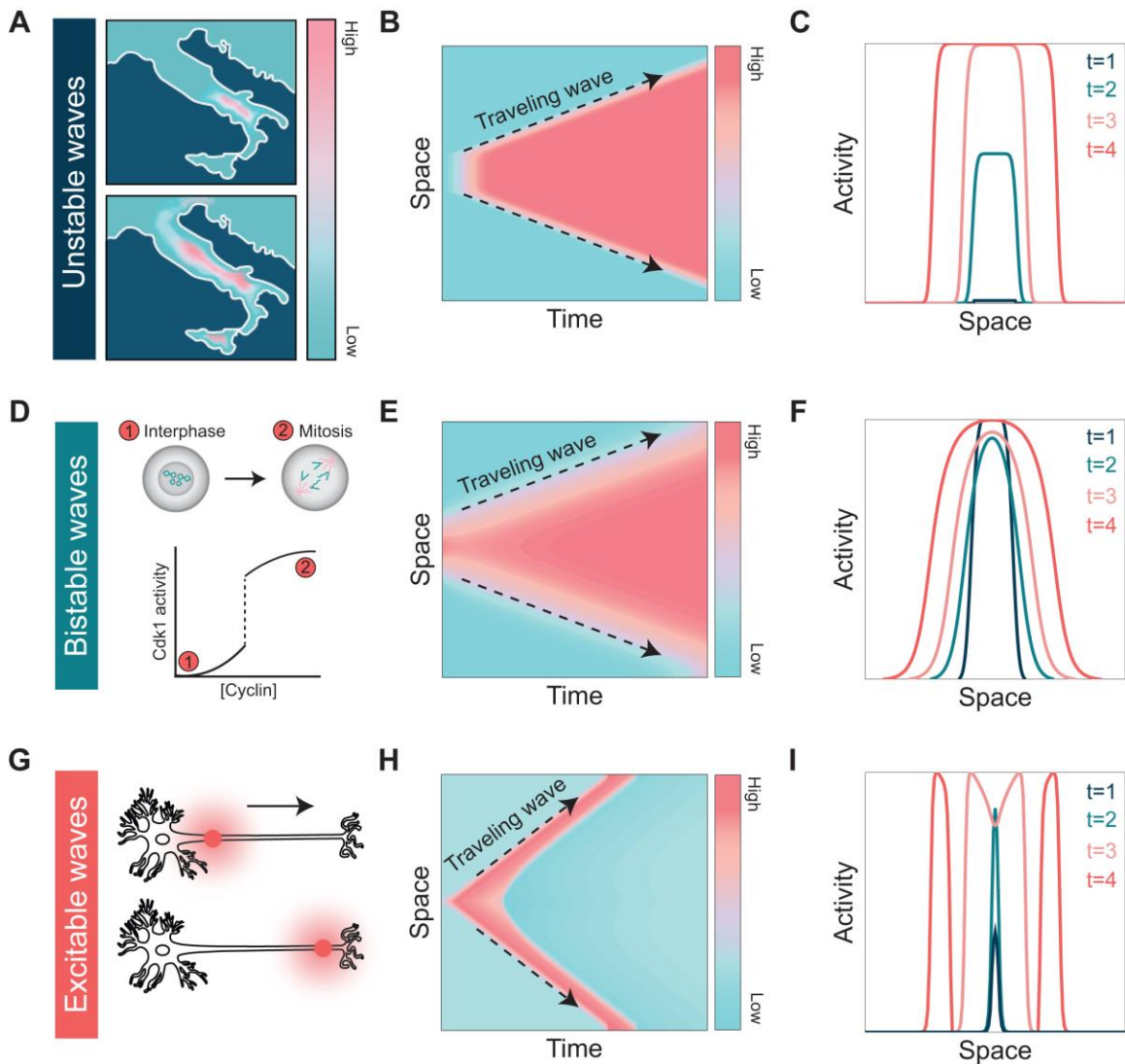


Figure 3: Unstable, bistable and excitable waves. A) Wave-like spreading of farming through Italy, adapted from (Baggaley et al., 2012). B-C) Propagation of Fisher-Kolmogorov unstable waves spreading through space. D) Diagram representing bistable regulation of the cell cycle transition from interphase to mitosis. Cdk1 activity exhibits a switch-like/bistable response as a function of cyclin concentration. E-F) Propagation of bistable chemical waves. G) Diagram representing the spreading of an action potential through an axon in a neuron. H-I) Excitable wave spreading through space and time.

Bistable and excitable waves have so far been more widely observed in cellular and developmental systems. A bistable system is characterized by two stable states, e.g.

a low and high state of activity. In biological systems, bistability usually arises from non-linear positive feedback (Ferrell and Ha, 2014). For concentration values between the two stable states, the concentration will either increase or decrease. A threshold exists such that values below the threshold evolve to the low steady state and values above the threshold evolve to the high steady state. As soon as the transition from low to high state is triggered in a given region, activity can diffuse to neighboring regions, shifting these regions above the activation threshold and therefore causing the transition from low to high. The new activity in this region can then itself propagate and initiate the transition in the next region and so on, effectively generating a traveling wave (Figure 3E). In physics, a typical example of traveling waves observed in a bistable medium are the waves driving solidification in supercooled liquids (van Saarloos, 1998), where solid and liquid phases represent the two stable states. The cell cycle control network is a canonical biological example of a bistable system, with interphase and mitotic cyclin-dependent kinase activity represent the two states (Figure 3D) (Morgan, 2007).

Much theoretical work has been developed to understand the properties of waves spreading in bistable media (van Saarloos, 1998). Most of the work in the physical literature has focused on bistable systems in which the parameters that characterize bistability are not time-dependent (van Saarloos, 1998). For supercooled liquids, experiments are conducted by slowly cooling the liquid and then very rapidly perturbing it to induce solidification, so that the wave propagates at a fixed temperature.

However, this assumption is not always justified for biological systems, which tend to display bistability only transiently, for example in transitions that are controlled by the accumulation of proteins. Our theoretical understanding of chemical waves spreading through transiently bistable media remains limited and it is likely that new mechanisms of wave-like spreading will emerge in biological systems that are driven rapidly out-of-equilibrium.

An excitable medium is a system which has only one stable state but two modes of returning to that state, which are established by non-linear feedback dynamics (Murray, 2002; Strogatz, 2000b). Positive feedback operates to generate a threshold-like response and negative feedback acts to reset the system to steady state. One prominent example of an excitable system in biology is the neuron. Neurons are normally at a resting potential. As a neuron is stimulated, its potential changes until it reaches a threshold. At this point, the neuron emits a spike, i.e. a large electrical signal, before relaxing back to its resting potential. The spike is then able to rapidly travel down the axon as a wave (Figure 3G) through a mechanism that emerges from the coupling of diffusion and excitability (Murray, 2002). Excitable waves are characterized by constant speed, constant wave amplitude, and a threshold for activation. In cell and developmental contexts, genetic networks characterized by positive and negative feedback can, under the appropriate conditions, generate an excitable system (Lindner et al., 2004; Suel et al., 2006). In neurons, an increase in the membrane potential leads to the

opening of ion channels, which results in a further rise in the membrane potential. This positive feedback drives the system past the threshold in neighboring areas. Once the membrane potential is at its peak, ion channels rapidly inactivate and another set of ion channels open in order to reset the initially “excited” region back to equilibrium. The net effect of these dynamics is a pulse of high activity traveling as a wave (Figure 3H-I) (Murray, 2002). Similarly, the aggregation of individual *Dictyostelium* amoebae is driven by traveling excitable waves of cAMP (Alcantara and Monk, 1974; Gregor et al., 2010; Kamino et al., 2011; Siegert and Weijer, 1995).

1.2.1.3 Measuring chemical waves in biological systems

Experimentally, the analysis of chemical waves, arising in reaction-diffusion systems, requires the ability to measure both the reaction and diffusion processes independently. Several optical methods have been developed for measuring the diffusion of molecules in biological tissues (Lippincott-Schwartz et al., 2001; Miyawaki, 2011). Measuring the reaction processes could be experimentally more difficult depending on the nature of the molecular mechanisms that control the reactions that generate waves. For systems in which the waves arise from feedbacks in signaling dynamics, optical techniques to measure the activity of biological molecules are required. The recent development of biosensors for several of the central pathways in cell and developmental systems makes it possible to analyze their dynamics quantitatively and with high spatiotemporal resolution (Regot et al., 2014). The

combination of these techniques with theoretical models will allow us to test the importance of chemical waves as a mechanism for spatiotemporal coordination in different contexts (Bement et al., 2015; Deneke et al., 2016). Below, I highlight recent work in which chemical waves have emerged as a central feature of biological regulation at cellular and multicellular scales.

1.2.2 Bistable and excitable waves in the regulation of the cell cycle, cytokinesis, and cell motility

1.2.2.1 Mitotic waves

Chemical waves have ideal properties for systems that require very rapid propagation of a signal across a large distance. One common example is found in developing eggs that are laid externally, such as those of insects, amphibians, and fish. Despite their large size (0.5-1.2 mm), these eggs execute the fastest cell cycles observed in biology (~8-25 min/cycle) (Foe and Alberts, 1983; Graham and Morgan, 1966; Kane and Kimmel, 1993; Kimmel et al., 1995). Even more remarkably, cell divisions in these eggs are coordinated with one another in synchronized “mitotic waves” (Foe and Alberts, 1983; Hara, 1971; Ogura and Sasakura, 2017; Rankin and Kirschner, 1997; Shinagawa et al., 1989). This global synchrony is important to ensure the proper execution of morphogenesis later in development.

The idea that the coupling of bistability and diffusion in the regulation of Cdk1 (cyclin-dependent kinase 1), the main driver of mitosis, could generate traveling chemical waves that would account for the observed mitotic waves was first proposed

theoretically by Novak and Tyson (Novak and Tyson, 1993). More recently, *in vitro* experiments using a *Xenopus* extract system confirmed that chemical waves of activity synchronize the cell cycles (Chang and Ferrell, 2013). When *Xenopus* egg cytoplasm was combined with nuclear-targeted GFP and chromatin in a Teflon tube, waves of nuclear envelope breakdown and reformation were observed to propagate at a constant speed of $\sim 1 \mu\text{m}/\text{sec}$ (Figure 4A-B). Importantly, when the tube was bisected, the nuclei on one half became uncoupled from the nuclei on the other half, suggesting that an active wave coupling mechanism which requires local diffusion was in place (Figure 4C). The mitotic waves in *Xenopus* were proposed to arise from a bistable system centered on Cdk1 and its regulation by two positive feedback loops involving Wee1 and Cdc25 during M-phase. In order to determine if this mechanism occurred *in vivo*, Chang et al. measured the speed of surface contraction waves, a downstream cytoskeletal effect of Cdk1, in fertilized eggs. Indeed, the speed of these waves matched the speed observed in the cycling extracts and followed the spatiotemporal dynamics predicted by an active wave mechanism (Chang and Ferrell, 2013).

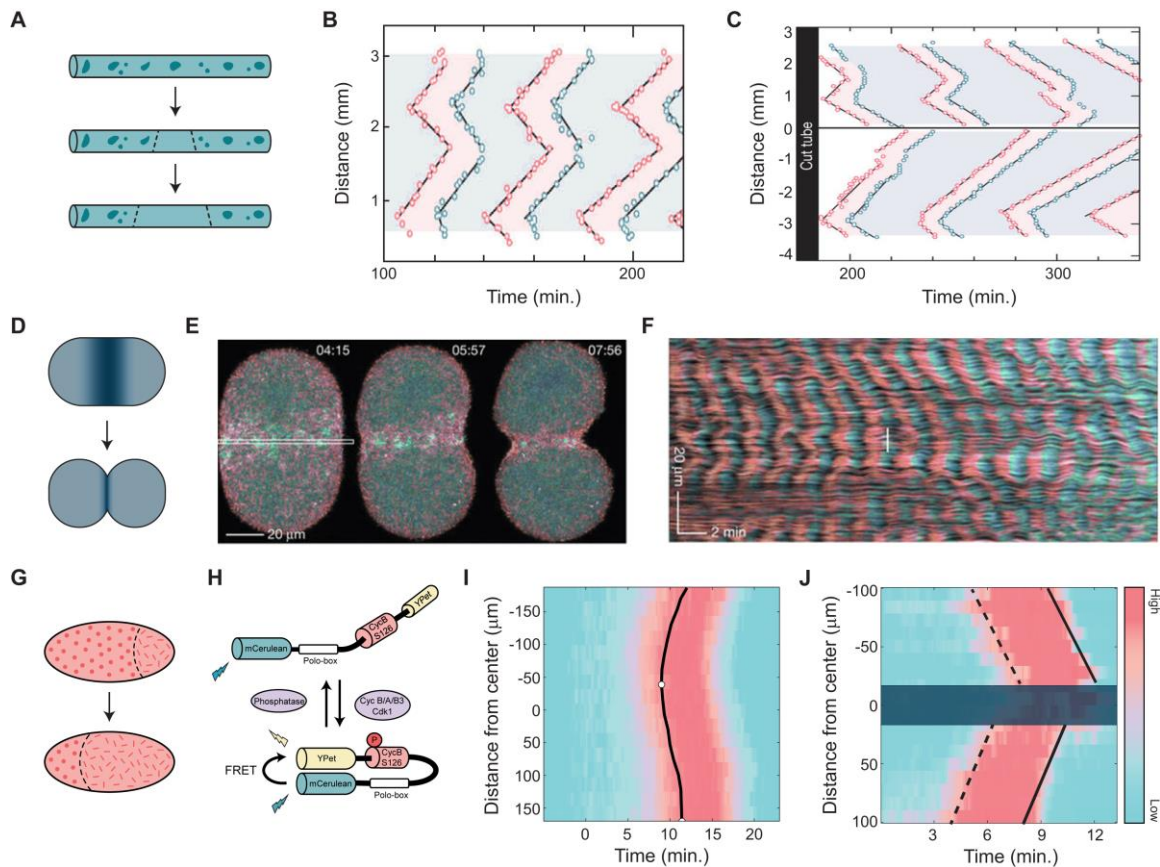


Figure 4: Examples of bistable and excitable chemical waves in biology. A) Schematic of mitotic waves in *Xenopus* egg extracts. Teal blobs represent interphase assemblies of sperm chromatin and nuclear-targeted GFP in a Teflon tube. Upon mitotic entry, blobs disassemble in a wave-like fashion. B) Waves of mitotic entry (pink circles) and exit (blue circles) in *Xenopus* egg extracts (adapted from (Chang and Ferrell, 2013)). C) Uncoupled mitotic waves upon physical separation of the extract in two halves (adapted from (Chang and Ferrell, 2013)). D) Schematic of cytokinetic ring formation. E) Starfish embryo co-expressing GFP-rGBD (cyan; Rho activity) and GFP-Utr (pink; F-actin) undergoing cytokinesis (adapted from (Bement et al., 2015)). F) Kymograph of an activated frog egg overexpressing Ect-2 depicting Rho-activity (cyan) and actin (pink) waves (adapted from (Bement et al., 2015)). G) Schematic of mitotic waves in a developing *Drosophila* embryo. H) Schematic of Cdk1 FRET sensor: active Cdk1 complex induces a conformational change that increases FRET efficiency. I) Heatmap of Cdk1 wave in a cell cycle 13 *Drosophila* embryo. Black line: mitotic entry wavefront; white circles: wave origins. J) Uncoupled Cdk1 waves following the introduction of a barrier during S-phase. Dotted line: mitotic entry front; solid line: mitotic exit front; shaded region: barrier (adapted from (Deneke et al., 2016)).

Further insights into these contraction waves and their relation to cytokinesis in both frog and starfish embryos was obtained via the demonstration that coordinated waves of Rho activity and F-actin assembly generate an excitable cortex which can orchestrate cytokinesis (Figure 4D) (Bement et al., 2015). The Rho-actin waves propagate at speeds of $\sim 0.2 \mu\text{m}/\text{sec}$ and have a fixed time delay, with F-actin waves following Rho activity waves (Figure 4E-F). Mathematical modeling suggests that waves arise in a reaction-diffusion system, in which Rho acts as an activator and F-actin as an inhibitor (Bement et al., 2015). The model displays a weak global excitability early on, which progresses to a strong localized excitability at the equator. This local excitability is thought to enable the cortex to rapidly adapt to signals from dynamic spindle orientation, suggesting that excitable chemical waves play a role in the spatial coordination of cytokinesis. Rho and F-actin excitability are modulated by Cdk1 activity, thus providing a link to cell cycle dynamics (Bement et al., 2015). This coupling might arise from a traveling wave of Cdk1 activity in frog embryos (Chang and Ferrell, 2013) and a gradient of Cdk1 activity in starfish embryos (Bischof et al., 2017). In cultured adherent cells, mitotic cortical waves of Cdc42 activity and of the F-BAR protein FBP17 might provide both positional and size information to specify the cell division plane (Xiao et al., 2017), suggesting a role for chemical waves in cell size control. It has been

speculated that linear waves in reaction-diffusion systems represent a strategy for size control in biological systems (Laughlin, 2015).

The experiments described above provide evidence for chemical waves in the long-range spatial coordination of the first cell cycle of frog embryos. Importantly, these mechanisms might only apply to the first cell cycle of *Xenopus* embryos, when the cell is very large and positive feedback plays an important role in the regulation of the cell cycle. Application of a steep temperature gradient across a frog egg allows the desynchronization of cell division, suggesting that cells are not spatially coupled and behave as independent oscillators (Anderson et al., 2017). Therefore, in *Xenopus* embryos, long-range spatial coordination takes place only during the first cell cycle and not in later stages when cells become small, are separated by membranes, and positive feedback is less important (Tsai et al., 2014).

The role of chemical waves in the synchronization of embryonic cleavage cycles and the mechanistic dissection of these waves can be addressed in the syncytial *Drosophila* embryo, a multinucleated cell with a shared cytoplasm, which is amenable to sophisticated live imaging approaches. The *Drosophila* embryo develops as a syncytium for the first 2 hours of development, during which it divides 13 times in a synchronized fashion (Figure 4G) (Farrell and O'Farrell, 2014; Ferree et al., 2016; Foe and Alberts, 1983; Rabinowitz, 1941). In 2016, we showed that chemical waves of Cdk1 activity synchronize the cell cycles (Deneke et al., 2016). Using a Fluorescence Resonance Energy Transfer

(FRET) biosensor of Cdk1 activity (Gavet and Pines, 2010a; Gavet and Pines, 2010b), Cdk1 waves were visualized directly for the first time (Figure 4H). Waves were found to propagate at speeds of $\sim 2\text{-}6 \mu\text{m}/\text{sec}$ (Figure 4I). The wave speed progressively slowed down as the embryo approached the maternal-to-zygotic transition (Deneke et al., 2016; Idema et al., 2013), which corresponds to a switch from rapid cell cycles, driven by maternal products and independent of transcription, to patterned cell cycle events (Farrell and O'Farrell, 2014; Ferree et al., 2016). It is intuitive to assume that the speed of the wave would be controlled by the rate of Cdk1 activity during mitotic entry. However, in *Drosophila* embryos, the activity of Cdk1 during mitosis was found to be invariant throughout development and could therefore not account for the observed slowdown of the wave speed. Surprisingly, changes in the rate of Cdk1 activation during S-phase do account for the physical properties of the waves. The importance of S-phase regulation of Cdk1 waves was demonstrated by introducing a barrier between two regions of the embryo during S-phase or M-phase. When the barrier was introduced during interphase, the two sides became asynchronous (Figure 4J), but when the barrier was introduced at the onset of mitosis, the wave of anaphase traveled unperturbed. This observation implies that Cdk1 waves observed during S-phase are active waves, which can be described by a bistable reaction-diffusion system (Deneke et al., 2016), while the mitotic waves are kinematic waves that follow after a fixed delay. This demonstrated a fundamental distinction between the mitotic waves in *Xenopus*, which were proposed to

be coupled during M-phase and the Cdk1 waves in *Drosophila*, which were shown to be coupled during S-phase. Chapter 2 of this dissertation will elaborate on these research findings. A similar phenomenon where an apparent mitotic wave is controlled by a wave-like pattern during S-phase has been observed during neurulation of ascidian *Ciona intestinalis* embryos, demonstrating an interesting parallel strategy for the generation of a mitotic wave across an embryo (Ogura and Sasakura, 2016).

Interestingly, both the M-phase and S-phase waves arise in the context of bistable regulation of Cdk1, suggesting that dissecting the control of mitotic waves requires careful analysis of possible mechanisms of regulation of bistable waves. These waves allow efficient synchronization and provide temporal accuracy by reducing the variability and noise sensitivity, intrinsic to bistable systems (Balazsi et al., 2011).

1.2.2.2 Chemotaxis, cell migration and mechanical waves

Another interesting system where wave-like patterns have been observed is steering cells during chemotaxis, where a locally excitable Cdc42 signal precedes cell turning and hence serves as a local compass to direct the cell to migrate towards the chemoattractant (Yang et al., 2016). In this study, Yang et al. investigated the migration dynamics of neutrophil-like cells in response to a gradient of chemically caged-chemoattractant that was released upon ultraviolet illumination (Collins et al., 2015). They found that Cdc42 is steeply polarized at the leading edge of chemotaxing cells and that this signal is wave-like and propagates at a speed of $\sim 1.1 \mu\text{m}/\text{sec}$. The locally

excitable Cdc42 signal, therefore, allows a cell to rapidly generate one or more protrusive fronts that can then become restricted to a single front through additional mechanisms. It remains to be elucidated whether the wave-like phenomena observed in this system serve a functional role or whether they are a by-product of the existence of positive and negative feedbacks. At a tissue level, waves could mediate the coupling of neighboring cells in order to facilitate collective cell migration.

Similarly, actin traveling waves that arise through cycles of activation and inhibition of actin nucleation, have emerged as major regulators of cell migration. One of the first examples of actin waves was in human neutrophils (Weiner et al., 2007). The dynamics of a key regulator of actin nucleation, Hem-1, showed cycles of activation and inhibition that generated propagating actin waves. Since then, actin waves have been observed and proposed as a fundamental feature of cell migration in many systems such as fibroblasts, *Dictyostelium*, and keratocytes (Allard and Mogilner, 2013; Barnhart et al., 2017; Devreotes et al., 2017; Inagaki and Katsuno, 2017; Machacek et al., 2009; Vicker and Grutsch, 2008). More recently it was shown that in fish keratocytes, local excitable dynamics of actin polymerization lead to protrusions at the leading edge (Barnhart et al., 2017). Given the small size of these cells, it is not intuitive that the role of the waves in this system is to propagate a signal faster than diffusion. However, waves can enhance the ability of a cell to steer by propagating signals that are locally amplified. The

development of quantitative models will be crucial to dissect the molecular mechanisms of the waves and to extend these insights to complex geometries such as 3D systems.

An important role for chemical waves has also emerged in the coordination of collective cell migration during wound healing. For example, the existence of calcium waves driving cytoskeletal reorganization in this context has long been recognized (Benink and Bement, 2005; Cordeiro and Jacinto, 2013; Xu and Chisholm, 2011). Such is the case in the *Drosophila* notum, where a wave of actomyosin apical constriction that is associated with a calcium wave is observed in response to injury (Antunes et al., 2013). Traveling waves of extracellular signal-related kinase (ERK) signaling have been proposed to play a role in collective cell migration following wound healing (Hiratsuka et al., 2015). First observed during skin renewal in mice (Hiratsuka et al., 2015), these waves travel outwards from the injury site and may arise from a mechanism similar to the one described above for bistable waves. An *in vitro* model can recapitulate features of the *in vivo* system, arguing that actomyosin contractility and collective cell migration are regulated by the ERK signaling wave, so that cells migrate in the opposite direction of the wave (Aoki et al., 2017). Remarkably, induction of an ERK signaling wave using an optogenetic tool results in collective migration in the direction opposite to the wave (Aoki et al., 2017).

Wave-like cellular reorganization and patterning of tissues could also be generated by mechanical signals. In epithelial tissues, adhesive forces are able to

propagate mechanical stresses across cells and wave-like propagations of mechanical stresses have been observed in the expansion of epithelial monolayers (Serra-Picamal et al., 2012). Cytoskeletal reinforcement and relaxation of the stresses are required to generate these waves, which travel at a very slow speed and are, therefore, likely to play a role in coordinating tissue growth on long timescales.

1.2.3 Chemical waves in other developmental and physiological contexts

The chemical waves described above in the regulation of the cell cycle, cytokinesis, and cell motility can be dissected theoretically through the analysis of bistable and excitable reaction-diffusion systems. The function of these waves is to transfer information rapidly across tissues or cells. In this Section, I briefly discuss chemical waves that might originate from different theoretical models and display a wider range of timescales, suggesting that chemical waves have roles in the regulation of multicellular organization that extend beyond the rapid transfer of information.

1.2.3.1 Waves of gene expression in the formation of somites

In vertebrates, somites are specified in the presomitic mesoderm (PSM) in a recurring, sequential manner resulting in a segmented pattern (Hubaud and Pourquie, 2014; Oates et al., 2012). The prevailing model for somite formation is the clock-wavefront model (Figure 5A) (Cooke and Zeeman, 1976; Hubaud and Pourquie, 2014). In this model, formation of somites requires two major components: a cell autonomous oscillator (the clock) and a wavefront, which represents a wave of maturation across the

PSM set by dynamical signaling gradients of proteins or small molecules (Fgf, Wnt, RA, etc.). Once the clock meets the wavefront in the right conditions (phase of the clock and levels of the gradients forming the wavefront), cells differentiate into somites. During this process, waves of gene expression span from the posterior to anterior of the PSM and lead to the specification of a somite at the anterior side (Aulehla et al., 2008; Masamizu et al., 2006). The traveling waves are generated by both a frequency and a phase gradient along the anterior-posterior axis (Gomez et al., 2008; Lauschke et al., 2013; Oates et al., 2012; Shimojo and Kageyama, 2016; Soroldoni et al., 2014). This is illustrated in Figures 5B-C, where the signaling activity of cells, oscillating in a frequency gradient, is plotted as a function of space and time, and gives rise to a wave pattern (Figure 5C).

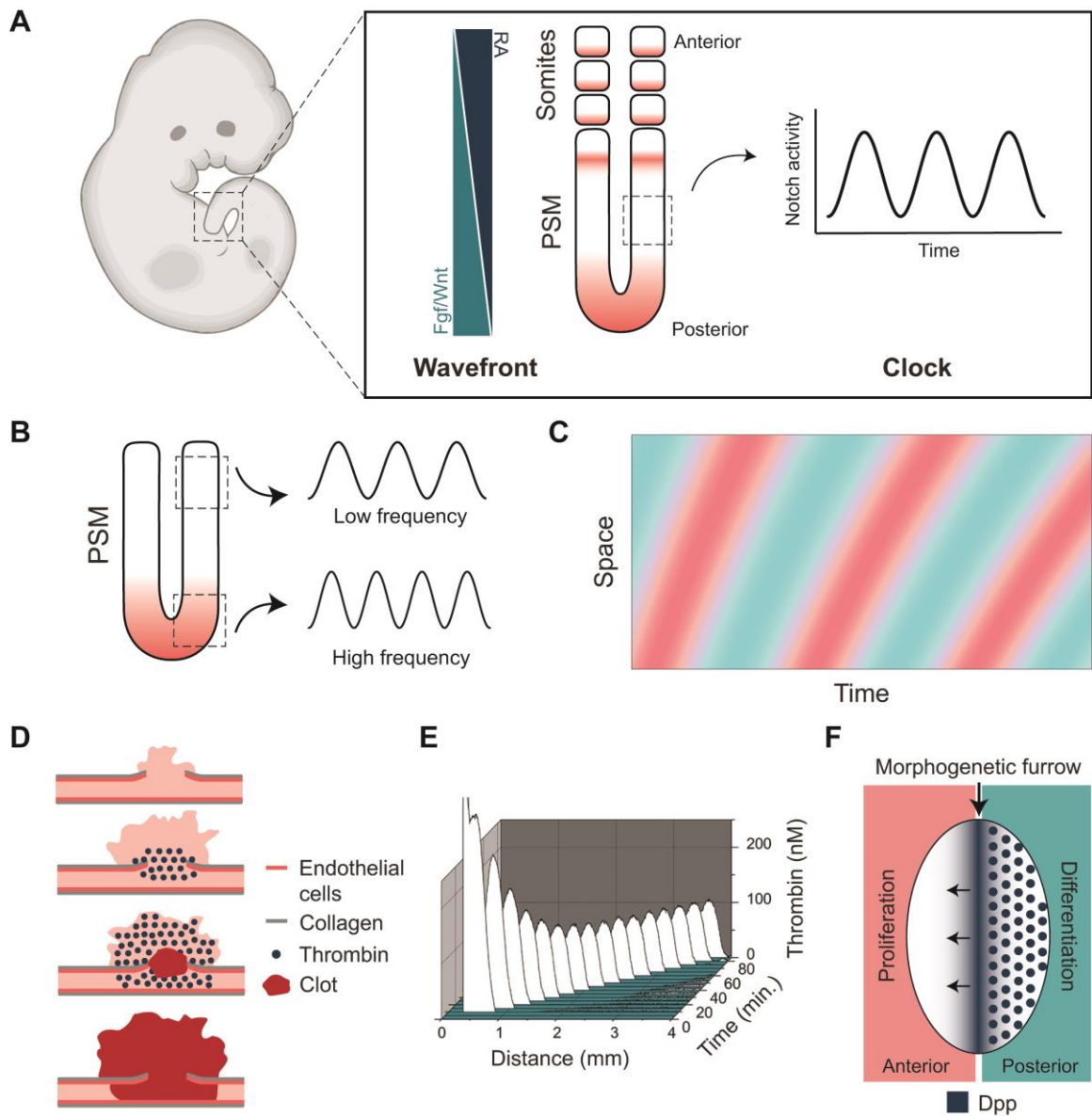


Figure 5: Additional examples of chemical waves in biological systems. A) Schematic of clock-wavefront model for somitogenesis. The presomitic mesoderm (PSM) exhibits oscillatory gene expression which generates waves that sweep from posterior to anterior. B) Schematic of PSM showing how gene expression oscillations have different frequencies along the anterior-posterior axis. C) Heatmap showing waves generated by a gradient of frequency through space. D) Schematic of clot formation upon injury. Upon contact with collagen layer (gray), thrombin (navy circles) gets recruited to the site of injury and spreads in a wave-like manner. The thrombin wave is followed by a delayed antagonistic wave that results in the formation of a localized blood clot (red). E)

Spatiotemporal distribution of thrombin activity wave (adapted from (Dashkevich et al., 2012)) F) Schematic of a *Drosophila* eye imaginal disc, showing a morphogenetic furrow moving from posterior to anterior and organizing cell differentiation and cell proliferation.

To determine whether the observed waves of gene expression were active or kinematic, Maroto et al. dissected the PSM into small fragments and found that they maintained their synchronized oscillations compared to the intact control, an observation consistent with kinematic waves (Maroto et al., 2005). However, when individual cells were dissociated from the posterior side of the PSM and cultured *in vitro*, they oscillated asynchronously (Maroto et al., 2005), indicating an important role for cell-cell contact/communication (Oates et al., 2012). Synchronization of the segmentation clock depends on Notch signaling, which is essential for the coherent spatiotemporal wave pattern (Jiang et al., 2000). The importance of this cell-cell coupling was demonstrated by experiments in which individual cells from the PSM are isolated and randomly mixed together (Tsiarris and Aulehla, 2016). After a few hours, cells begin to display synchronized oscillations of a Notch signaling reporter and traveling waves of gene expression emerge. Mixing cells from different region of the PSM or isolated at different stages of oscillation indicated clearly that cells are able to adjust their frequency and phase in response to their neighbors.

Theoretically, the waves observed in these experiments are reminiscent of waves observed in systems of coupled oscillators. These systems have been extensively studied in mathematics. The Kuramoto's model, for example, describes the dynamics of a large

number of oscillators which can influence each other's phase (Kuramoto, 1986; Strogatz, 2000a). This coupling among oscillators pushes them towards a similar phase and, if it is sufficiently strong, can synchronize them and, under certain conditions, generate traveling waves (Rodrigues et al., 2016). Several experimental and theoretical analyses based on these ideas have revealed significant insights on the process of somitogenesis (Lauschke et al., 2013; Riedel-Kruse et al., 2007; Soroldoni et al., 2014). However, this model of phase-coupled oscillators has been recently brought into question as it was proposed that the waves of somitogenesis might, in fact, arise from an excitable system (Hubaud et al., 2017). In cultures reconstituted from isolated PSM cells, oscillations are initiated in both a density-dependent and substrate-dependent manner, suggesting a role for mechanical and cytoskeletal cues. This idea was strengthened by experiments demonstrating that signaling from the Yap pathway, which is known to be important in mechano-transduction (Pancier et al., 2017), affects the ability of PSM cultures to undergo collective, synchronized oscillations, that spread as traveling waves (Hubaud et al., 2017). Analysis of a mathematical model of excitability (FitzHugh-Nagumo model) demonstrated that several experimental observations are compatible with the behaviors of an excitable system involving both Notch and Yap signaling pathways (Hubaud et al., 2017). We expect that further quantitative imaging experiments and theoretical analyses will reveal the mechanisms regulating the properties of the waves, thus shedding light on a fundamental developmental process.

1.2.3.2 Waves in blood coagulation

Another example of an active wave phenomenon has been proposed in the process of blood coagulation. An advantage of having a wave-like response in wound healing is the ability to coagulate quickly across distances of millimeters to centimeters. Upon vascular injury, blood is released and comes into contact with a layer of collagen, which is present in the layer of extracellular matrix surrounding the vessels (Ataullakhanov et al., 1998). This contact promotes the release of thrombin, an enzyme that drives the process of blood clotting (Figure 5D). Using an *in vitro* model of wound healing, traveling waves of thrombin activity were observed by measuring the cleaving event of a fluorogenic thrombin-specific peptide substrate (Figure 5E) (Dashkevich et al., 2012). These thrombin activity waves exhibited the canonical features of an excitable wave: constant speed, constant wave amplitude, and a threshold for activation. A potential problem that arises from triggering a wave of coagulation is restricting the wave to the wound site. In response to this issue, a second antagonistic wave that stops the spreading of the coagulation wave has been proposed in order for clotting to be locally confined (Ataullakhanov et al., 1998). These observations have been limited to *in vitro* studies, therefore the role of thrombin activity waves in more complex tissues such as the adult skin in the context of wound repair remains to be elucidated.

1.2.3.3 Waves in patterning cell cycle and cell differentiation in *Drosophila*

A well-characterized system that displays a moving signaling wavefront is the *Drosophila* eye imaginal disc. In this system, Dpp and Hedgehog, a set of interacting signaling pathways, specify a morphogenetic furrow that travels across the tissue from the posterior to the anterior as a function of time (Figure 5F) (Roignant and Treisman, 2009). The major function of this moving furrow is to organize the pattern of cell differentiation and cell proliferation in space and time (Baker, 2007). The movement of the furrow is driven by an autocatalytic regulatory loop involving the Hedgehog morphogen (Roignant and Treisman, 2009). Cells that receive the Hedgehog ligand differentiate. As they differentiate, they express and release the Hedgehog ligand themselves, thus inducing the neighboring anterior cells to differentiate and release the ligand. This generates a traveling wave (Roignant and Treisman, 2009). The moving morphogenetic furrow clearly does not transfer information rapidly, since it takes about 2 days for the furrow to travel over the 100-200 μm of the tissue, i.e. a speed about 4-5 order of magnitude smaller than the speed observed in the mitotic waves of early embryogenesis (Roignant and Treisman, 2009). We speculate that a traveling wave in this developmental context provides a sharp spatial separation between the region of proliferation and that of differentiation. For such separation to be effective, the timescale of the moving wavefront must match the intrinsic timescales of proliferation and differentiation, which are of order of hours and not seconds or minutes. This is achieved

by introducing a delay of about 1-2 hours in the feedback loop, regulating Hedgehog expression (Roignant and Treisman, 2009). Specifically, Hedgehog activates the release of the Epithelial Growth Factor (EGF) ligand, Spitz. Spitz is received by neighboring cells, which in response activate the Punt transcription factor, which is responsible for transcription of the *hedgehog* gene, thus closing the feedback loop (Roignant and Treisman, 2009). The delays imposed by transcription, translation of several factors and processing of extracellular signals set the speed of the morphogenetic furrow. We propose that “slow” chemical waves in this system generate a sharp transition that allows for the precise control of transcriptional programs resulting in specific cell fate behaviors.

1.3 Cytoplasmic flows as an organization mechanism in biology

Cytoplasmic flow or streaming is a continuous circulation of cellular fluids within cells and is ubiquitous in biology (Goldstein and van de Meent, 2015; Quinlan, 2016). Intracellular flows were first discovered and are most common in plant cells, where these flow patterns were readily obvious and easy to visualize (Allen and Allen, 1978). Streaming is in most cases driven by cytoskeletal machinery, with examples of actomyosin-driven flows as well as microtubule-based flows (Goldstein and van de Meent, 2015). Nonetheless, it is still unclear what the topology of the cytoskeletal network must be to give rise to stereotypic and reproducible flows. In addition to plants, cytoplasmic streaming has been observed in oocytes, fungi, slime moulds, amoebae and

protozoa (Goldstein and van de Meent, 2015). My dissertation delves into the role of cytoplasmic flows in coordinating nuclear positioning in the early fly embryo and how integration of local cell cycle signals with cortical actomyosin can regulate such flows.

1.4 Summary of the work included in this dissertation

The work presented in this dissertation broadly focuses on identifying organizing principles in the establishment and maintenance of cell cycle synchronization in *Drosophila* embryogenesis. In Chapter 2, I describe my work discovering the role of chemical waves of Cdk1 activity which synchronize the cell cycle during the syncytial blastoderm stages. In Chapter 3, I describe my work on the role of cytoplasmic flows in the positioning of nuclei, which is required for the establishment of cell cycle synchrony. Chapter 4 serves as a discussion and identification of future directions of the aforementioned studies.

2. Waves of Cdk1 activity in S-phase synchronize the cell cycle in *Drosophila* embryos

Chapter 2 was modified from a manuscript (of the same title) published in *Developmental Cell* 38, 399-412 (2016). doi: 10.1016/j.devcel.2016.07.023. The authors were Victoria E. Deneke, Anna Melbinger, Massimo Vergassola and Stefano Di Talia. Section 2.3.6 was modified from a manuscript published in *PNAS* 115 (10), E2165-2174 (2018). doi: 10.1073/pnas.1714873115. The authors were Massimo Vergassola, Victoria E. Deneke and Stefano Di Talia. Massimo Vergassola and Stefano Di Talia developed the theory and wrote the manuscript. For the latter manuscript, my contribution was to perform the experiments, analyze the experimental data, and aid in visualization and figure design.

2.1 Summary

Embryos of most metazoans undergo rapid and synchronous cell cycles following fertilization. While diffusion is too slow for synchronization of mitosis across large spatial scales, waves of Cdk1 activity represent a possible process of synchronization. However, the mechanisms regulating Cdk1 waves during embryonic development remain poorly understood. Using biosensors of Cdk1 and Chk1 activities, we dissect the regulation of Cdk1 waves during the last four syncytial cell cycles of *Drosophila* embryos. We show that Cdk1 waves are not controlled by the mitotic switch but by a double negative feedback between Cdk1 and Chk1. Using mathematical

modeling and surgical ligation experiments we demonstrate a fundamental distinction between S-phase Cdk1 waves, which propagate as “sweep” waves, and mitotic Cdk1 waves, which propagate as passive phase waves. The in vivo dynamics of Cdk1 are captured by a transiently bistable reaction–diffusion model, where time-dependent reaction terms account for the growing level of cyclins and Cdk1 activation across the cell cycle. Sweep waves generate a wave-like spreading that differs from bistable waves for its dependence on dynamic parameters and its faster speed. Our findings show that in *Drosophila* embryos, Cdk1 positive feedback serves primarily to ensure the rapid onset of mitosis, while wave propagation is regulated by S-phase events.

2.2 Introduction

Early development in most metazoans is characterized by remarkably fast and coordinated cell cycles (O'Farrell et al., 2004). This early cell cycle program is thought to be under strong selective pressure for organisms that lay eggs externally, as eggs depend entirely on the maternal nutrients deposited within them (Farrell and O'Farrell, 2014). In such systems, mothers lay large eggs which store sufficient nutrients for embryonic development, and embryos rapidly amplify their DNA content prior to activation of zygotic gene expression at the maternal-to-zygotic transition (O'Farrell, 2015). This is achieved through exceptionally rapid and synchronous cleavage divisions. Synchronization appears to be necessary in order to ensure that a precise developmental

program is executed in a timely manner throughout the entire embryo during morphogenesis.

After fertilization, the *Drosophila* embryo undergoes 13 synchronous rounds of S-phase and mitosis (Rabinowitz, 1941), which take place in a multi-nucleated syncytium. The first 9 cell cycles are extremely rapid, lasting about 8-9 minutes (Edgar et al., 1994; Farrell and O'Farrell, 2014; Foe and Alberts, 1983). The remaining 4 cell cycles get gradually longer (Edgar et al., 1994; Farrell and O'Farrell, 2014; Foe and Alberts, 1983). This lengthening of the cell cycles is accounted by longer S-phase, as mitosis has a stereotypical duration of about 4 minutes (Farrell and O'Farrell, 2014), and by the activation of the DNA replication checkpoint (Farrell and O'Farrell, 2014; Fogarty et al., 1997; Sibon et al., 1997), which is likely triggered by the increase in DNA content of the embryo. The main effector of the DNA replication checkpoint is Chk1, which regulates the cell cycle by inhibiting Cdk1 activity (Morgan, 2007). This is accomplished in part by the activation of Wee1 by Chk1 (Lee et al., 2001), which is required for the low activity of Cdk1 observed in interphases of cell cycles 12 and 13 (Fasulo et al., 2012; Price et al., 2000; Royou et al., 2008; Stumpff et al., 2004). However, the contribution of these and other regulatory mechanisms to the synchronization of the early cell cycles remains unclear.

How spatial coordination is achieved during development across hundreds of microns remains largely uncharacterized. The *Drosophila* embryo provides a good model

to study the synchronization of biological events during development. It is about 500 μm long and 150 μm wide (Foe and Alberts, 1983), and, despite its large size, the embryo follows a precisely timed program. Diffusion within the large cytoplasm is too slow to account for long-distance synchrony. Assuming a diffusion coefficient of about 10 $\mu\text{m}^2/\text{s}$ (which would be expected for a typical protein), it would take several hours for a protein to diffuse across the embryo, a timescale which is clearly incompatible with the synchronization of the *Drosophila* cell cycle, which happens on timescales of tens of seconds. Chemical waves provide a much more rapid mechanism of communication between and across cells and have been observed in many species. There are two classes of chemical waves: trigger waves and phase waves. Trigger waves in reaction kinetics systems are generated by the coupling of catalytic loops with diffusion, which can spread biochemical activity much faster than simple diffusion (Gelens et al., 2014; Tyson and Keener, 1988). Dimensional analysis indicates that the speed of a trigger wave is determined by Luther's formula: $v \sim (Dk)^{1/2}$, where D indicates the diffusion coefficient and k is the relevant kinetic rate (Tyson and Keener, 1988). Systematic analysis of the reaction-diffusion system responsible for the generation of the wave is required to deduce the relevant rate k (van Saarloos, 1998). Conversely, phase waves are passive and do not involve any spatial coupling or diffusion (Winfree, 2001). They arise as a purely kinematic mechanism, which reflects spatially non-uniform timing mechanisms. For example, a set of identical oscillators with a spatially non-uniform initial phase

would generate a wave, even in the absence of any diffusion or coupling among the oscillators (Winfree, 2001). For this reason, phase waves are often referred to as pseudo-waves. Physical barriers provide the standard experimental tool to distinguish between trigger and phase waves. While the propagation of a trigger wave is hindered by a barrier, phase waves would move undisturbed through the barrier.

Mathematical models for developmental waves are based on reaction–diffusion systems that describe the feedback loops between Cdk1, the phosphatases Cdc25, and the kinase Wee1 (Morgan, 2007). Models feature substantial time dependency, which is due to the variable levels of cyclins and Cdk1 activation across each cell cycle. This constitutes a notable difference with respect to the time-independent standard models for bistable waves (Tyson and Keener, 1988; van Saarloos, 1998).

Recent *in vitro* experiments suggest that propagation of chemical waves of Cdk1 activity synchronize cell cycles in the *Xenopus* extract system (Chang and Ferrell, 2013). Indeed, interlinked positive feedback loops involving Wee1 and Cdc25 (Morgan, 2007) provide a bistable Cdk1 network capable of transmitting chemical waves. However, in *Drosophila* the speed of the mitotic waves slows down from cell cycle 10 to cell cycle 13 (Idema et al., 2013), without a concomitant slowing of mitosis (Farrell and O'Farrell, 2014; Foe and Alberts, 1983). The mitotic waves in this system were instead suggested to stem from excitable mechanical waves (Idema et al., 2013). Collectively, these

observations indicate that the physical and molecular mechanisms responsible for cell cycle synchronization *in vivo* remain to be elucidated.

Here we address the mechanisms driving synchronization of cell cycles 10-13 of the early *Drosophila* embryo. By making use of biosensors for Cdk1 and Chk1 activity, we directly document chemical waves and test the relationship between chemical and mitotic waves. We found that in cell cycles 12 and 13 the slowdown of Cdk1 waves is not explained by a slower activation of the mitotic switch but rather by the activation of the S-phase DNA replication checkpoint, which controls Cdk1 through the Chk1/Wee1 pathway. Mathematical modeling using a time-dependent reaction diffusion system captured the speed of the waves and predicted a fundamental distinction between S-phase Cdk1 waves, which propagate as active waves in an excitable medium, and mitotic Cdk1 waves, which propagate as passive phase waves that reflect the delays set by the active waves. Confirming that prediction, we show that physical barriers interrupt propagation of S-phase but not of mitotic waves. Our findings demonstrate that in *Drosophila* embryos, Cdk1/Wee1/Cdc25 positive feedbacks serve primarily to ensure a rapid activation of Cdk1. Conversely, the S-phase activity of Cdk1 and its regulation by Chk1 is responsible for triggering and regulating the speed of the mitotic wave.

2.3 Results

2.3.1 Visualization and quantification of Cdk1 and mitotic waves

Mitotic waves spread across the embryo, as revealed by confocal microscopy of embryos with tagged histones (Figure 6A in this Dissertation and Movie S1 in Deneke et al., 2016). In agreement with previous results (Idema et al., 2013), the wave of mitotic entry and the wave of mitotic exit are strongly correlated in space and time, with a consistent delay of 4 minutes between prophase and anaphase. This observation implies that the physical properties (e.g. speeds) of the two waves are essentially identical and hereafter we will refer to them as mitotic waves interchangeably. Surgical ligation experiments, which separate the embryo into two compartments (Newman and Schubiger, 1980; Sander, 1971), demonstrate that physical barriers block mitotic waves, indicating active wave propagation (Movie S2 in Deneke et al., 2016). These confocal-imaging observations confirm classical observations by Edgar et al. (Edgar et al., 1986). To unravel the regulatory mechanisms that control mitotic waves, we used a FRET-based biosensor for the activity of Cdk1 (Figure 6B) (Gavet and Pines, 2010b). The Cdk1 FRET signal showed clear oscillations corresponding to cell cycle progression (Figure 6C), and RNAi experiments indicated that the Cdk1 sensor responds to CycA-, CycB-, and CycB3-Cdk1 complexes in this system (Figure 7B-C). Imaging at high spatial and temporal (2 s) resolution allowed us to obtain a precise spatiotemporal map of Cdk1 activity (Figures 6D-E). Analysis of the dynamics of Cdk1 activity in different regions

along the anterior-posterior axis of the embryo revealed the propagation of waves of Cdk1 activity (Figure 6F). Measuring the time required for the waveform to travel a given distance, we found that waves propagate through the embryo at roughly constant speed (Figure 6G, Figure 7H). Moreover, the speeds of Cdk1 waves and mitotic waves are strongly correlated, suggesting that Cdk1 activity drives the mitotic waves (Figure 6H).

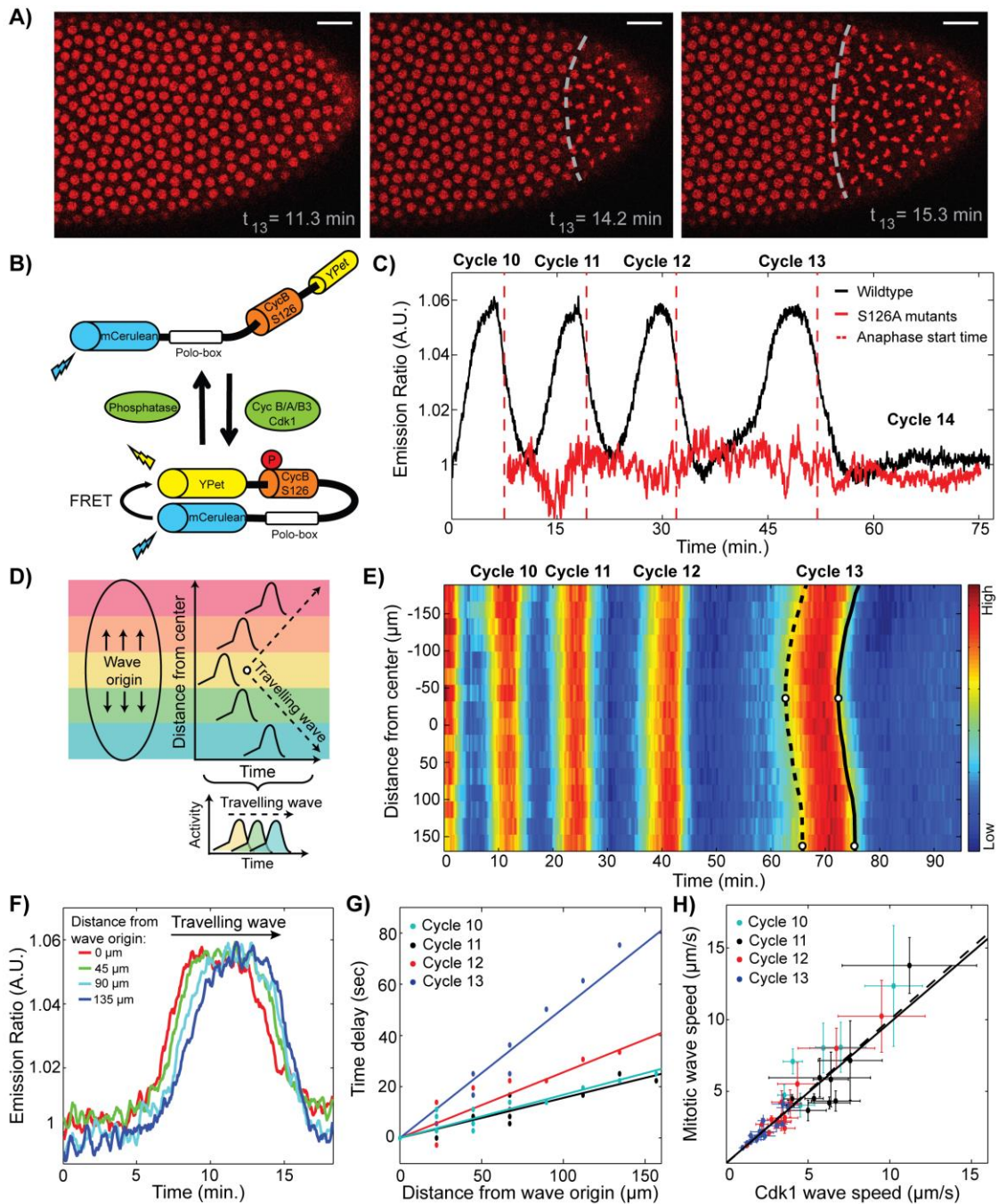


Figure 6: Cdk1 waves drive mitotic waves. (A) Time lapse series depicting the propagation of a mitotic wave in an embryo with RFP-tagged histones. (B) Schematic view of the Cdk1 FRET biosensor composed of two fluorophores, YPet and mCerulean, which are linked by a Cdk1 phosphorylation site from cyclin B1 (S126) and the polo box domain of Plk1. Upon phosphorylation of the Cdk1-specific phosphorylation site, the

sensor undergoes a conformational change that results in increased FRET efficiency. (C) Emission ratio of FRET sensor averaged across one embryo shows clear oscillations of Cdk1 activity, which increases upon mitotic entry and remains low during early interphase 14, when the levels of active Cdk1 are uniformly low. Red line, S126A mutant; red dotted line, average anaphase entry time. (D) Cdk1 traveling waves can be visualized by plotting the activity profiles as a function of space and time. First, images are divided into different regions along the anterior-posterior axis of the embryo (colored boxes). Activity profiles for each region are then calculated and plotted as a function of time and space, which allows for the visualization of the wave front (dotted line). (E) Heat-map of Cdk1 activity over time and along the anterior-posterior (AP)-axis of an embryo. White circles indicate wave origins at cycle 13, dotted line indicates the mitotic entry front and the black line indicates the anaphase wave front. (F) Cdk1 activity profiles for different positions along the AP-axis of an embryo in cell cycle 13. (G) The speed of the wave is estimated by computing the time elapsed for the wave to travel a given distance along the embryo: the inverse slope of a linear fit yields the speed. (H) Mitotic wave speed as a function of Cdk1 wave speed. Dotted line, identity line; solid line, best-fit curve. Scale-bars, 10 μ m. Error bars, 95% confidence interval (CI); a.u., arbitrary units.

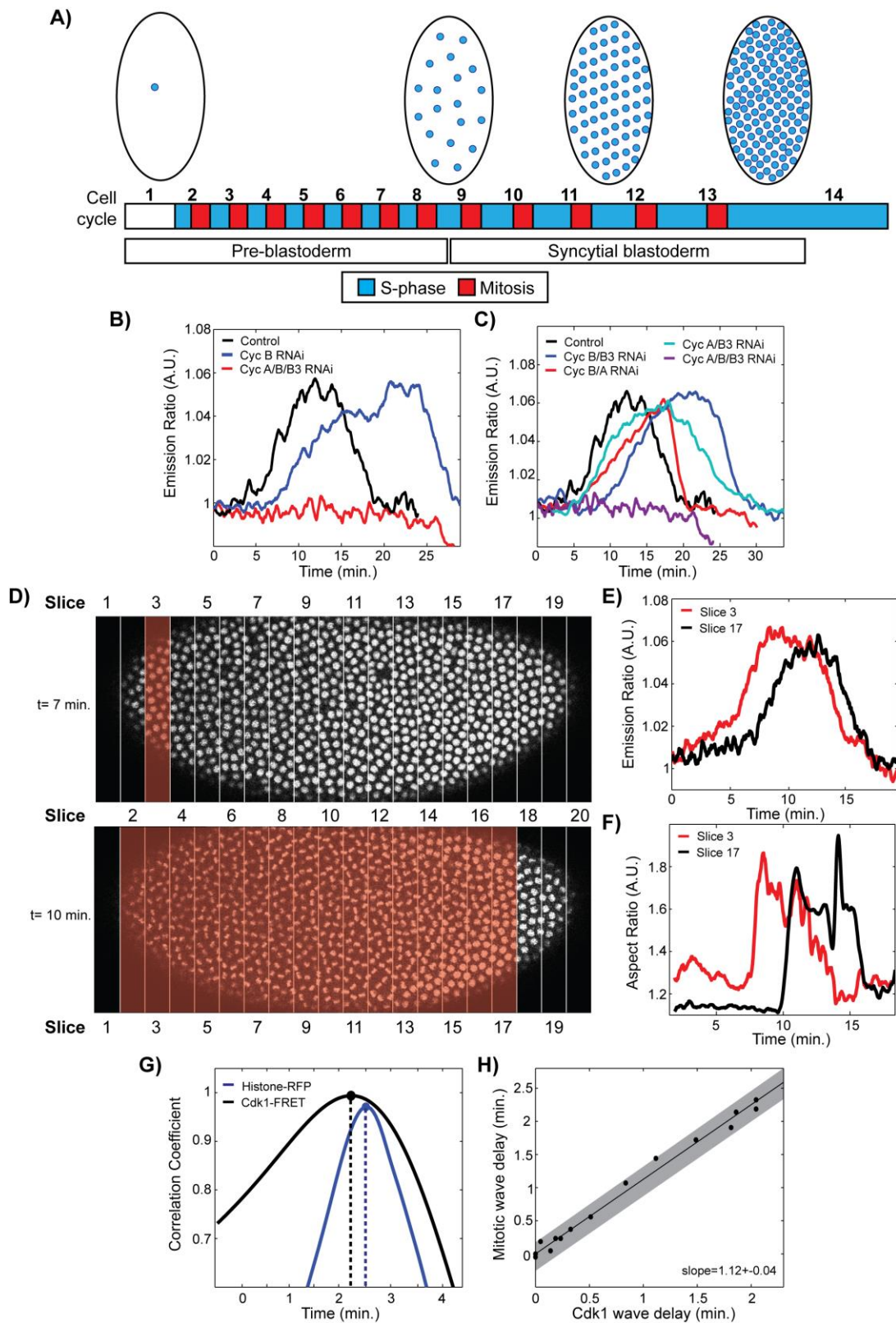


Figure 7: Validation of the Cdk1 FRET sensor and computational method to calculate wave speed. (A) Schematic of early development in *Drosophila*. (B) Cdk1 sensor is not specific to cyclin B-Cdk1 complexes. (C) Cdk1 sensor responds to the activity of all three cyclin-Cdk1 complexes as indicated by pairwise knockdown of cyclins. Triple knockdown results in an arrested cell cycle and failure of the Cdk1 sensor to detect any changes in FRET efficiency. Control indicates dye injection. (D) Images of His2Av-RFP embryos that were divided into 20 vertical slices along the AP-axis. Red shaded box represents area where nuclei are transitioning between slow and fast Cdk1 ramp-up. (E) Cdk1 FRET sensor emission ratio for slice 3 (red) and slice 17 (black). (F) Aspect ratio of nuclei estimated from His2Av-RFP images for slice 3 (red) and slice 17 (black). (G) Correlation coefficient analysis using slice 3 and 17 for His2Av-RFP (blue) and Cdk1-FRET (black) images. Shaded circle represents local maximum and dotted line corresponds to the time delay at which the correlation coefficient is at its maximum. (H) Mitotic wave delay versus Cdk1 wave delay for all slices in one embryo.

2.3.2 Cdk1 activity during S-phase is predictive of mitotic and Cdk1 wave speed at cycles 12 and 13

Mitotic waves decrease in speed as developmental cycles progress (Idema et al., 2013). Cdk1 waves also slow down from cycle 10 to 13 (Figure 8A). Dimensional analysis predicts that the velocity v of a chemical wave follows Luther's formula, $v \approx \sqrt{Dk}$, where D is the diffusion coefficient and k is the relevant reaction rate (Luther, 1906). This suggests that, for chemical waves to slow down with the cycles, the reactions that control wave propagation and/or the diffusion of key factors should decrease. FRAP experiments showed that Cdk1 diffusion does not change significantly in cycles 10-13 (Figure 8B). Conversely, Cdk1 activation is biphasic during late cycles, with a slow rise (rate k_s) followed by a fast activation (rate k_M) during mitotic entry (Figure 8C). Using the disappearance of tagged PCNA foci as a readout for completion of DNA replication

(Shermoen et al., 2010) (Figure 9), we determined that the inflection point of the biphasic Cdk1 activation slightly precedes the time of completion of S-phase. This result indicates that the slow rise at rate k_S reflects the activation of Cdk1 during S-phase. The rate of Cdk1 activation upon mitotic entry (k_M) remains constant during cycles 10-13 (Figure 8D, blue bars). This is consistent with the observation that the duration of mitosis is roughly constant during these cell cycles (Farrell and O'Farrell, 2014; Foe and Alberts, 1983), which was interpreted in (Idema et al., 2013) as evidence against chemical waves and in favor of mechanical waves.

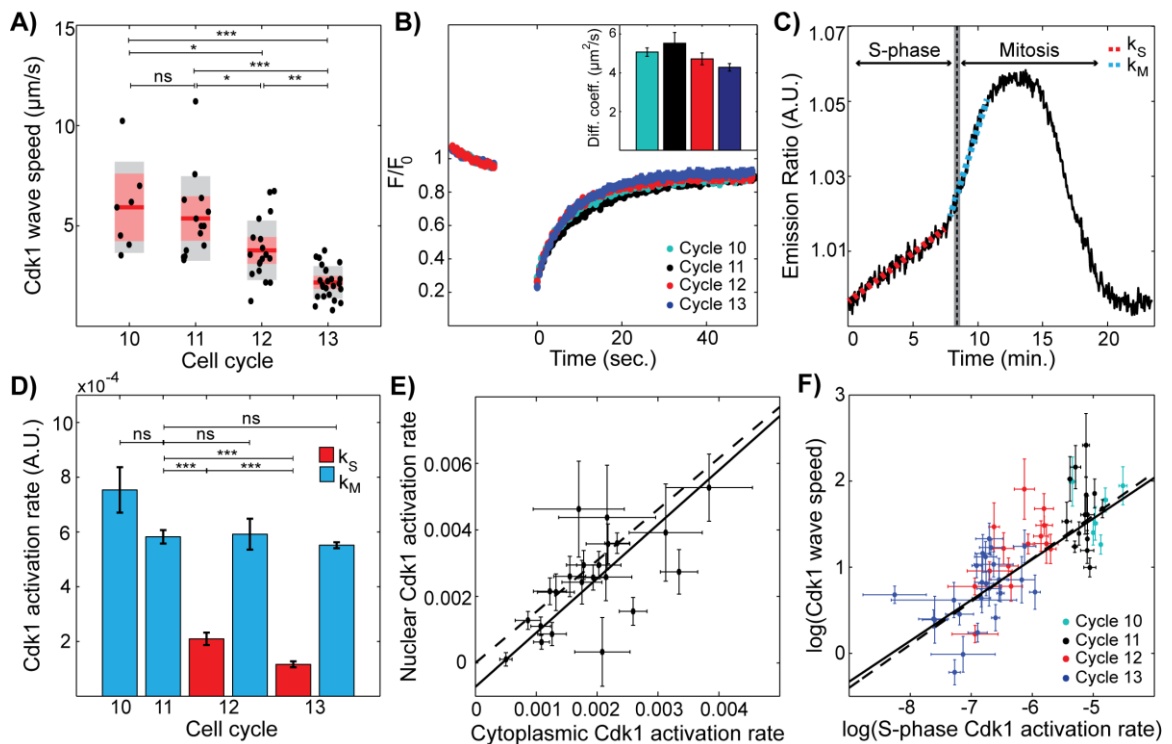


Figure 8: Cdk1 activity during S-phase is predictive of mitotic and Cdk1 wave speed. (A) Cdk1 wave speed as a function of developmental cycles. Red line, mean; gray box, 95% CI; red box, 1 standard deviation (SD). (B) Normalized fluorescence intensity profile of YFP-tagged Cdk1 before and after photobleaching. Inset, calculated diffusion

coefficient per cell cycle. Error bars, standard error of the mean (s.e.m.) (C) Emission ratio of Cdk1 sensor for cycle 13 displays biphasic behavior. Red dotted line corresponds to Cdk1 activation rate during S-phase (k_S) and blue dotted line corresponds to Cdk1 activation rate during mitosis (k_M). Completion of S-phase was determined through the disappearance of RFP-tagged PCNA foci, see Supplemental Information for details. (D) Average Cdk1 activation rate per cell cycle. Red bars, S-phase Cdk1 activation rate (k_S); blue bars, mitotic Cdk1 activation rate (k_M). Error bars, s.e.m. (E) Nuclear and cytoplasmic Cdk1 activities were calculated by segmenting nuclei with an intensity threshold and averaging intensity inside and outside nuclear mask, respectively. Dotted line, line with a slope given by the ratio of nuclear Cdk1 levels to cytoplasmic Cdk1 levels, measured using embryos expressing Cdk1-YFP; solid line, best-fit curve. Error bars, 95% CI. (F) Log-log plot of Cdk1 speed versus S-phase Cdk1 activation rate. Solid line, best-fit curve; dotted line, Luther's formula. Error bars, 95% CI. *, $p < 0.05$; **, $p < 0.001$; ***, $p < 0.0001$; ns, not significant.

However, chemical rates significantly decrease during S-phase, i.e. k_S diminishes at cycles 12 and 13 (Figure 8D, red bars) both in the cytoplasm and in nuclei (Figure 8E). These data suggest that the rate k_S of Cdk1 activation in S-phase controls the slowing of the Cdk1 chemical waves as $v \approx \sqrt{Dk_S}$, which was indeed confirmed in Figure 8F.

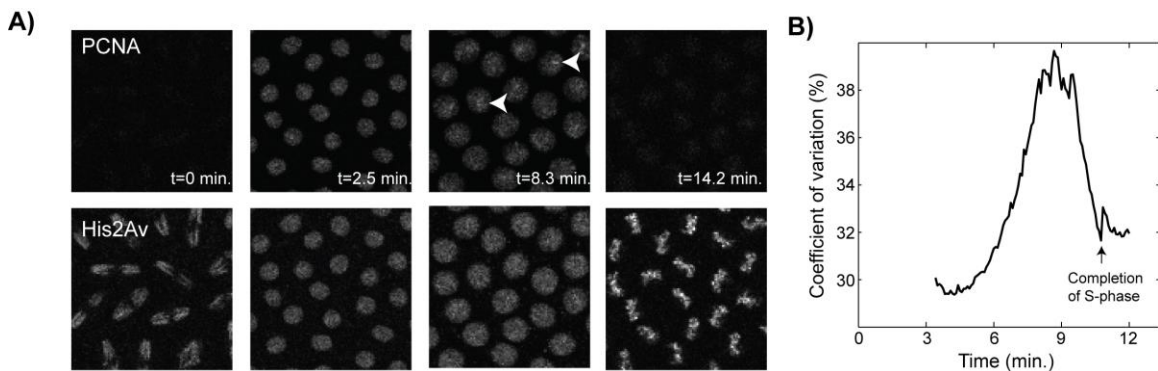


Figure 9: PCNA-TagRFP as a marker of completion of S-phase. (A) Top panel shows time-lapse images of PCNA-TagRFP, which localizes to foci in late S-phase (arrowheads). Lower panel shows His2Av-GFP signal as a reference to mitotic events. (B) Coefficient of variation (ratio of standard deviation to mean of intensity signal) for all nuclei in an embryo. Completion of S-phase was identified as the point when the coefficient of variation returns to a basal interphase level.

2.3.3 Cdk1 activity during S-phase is predictive of mitotic and Cdk1 wave speed at cycles 12 and 13

Our results argue that the velocity of mitotic and Cdk1 waves is controlled by Cdk1 activation during S-phase. To test this model, we looked for genetic perturbations that specifically alter the rate of activation of Cdk1 in S and M phases. We first analyzed mutants of the main effector kinases of the DNA replication checkpoint, Chk1 and Chk2. We used *chk1 chk2* mutants, instead of *chk1* mutants, as *chk1* mutants undergo a Chk2-dependent developmental arrest which makes the analysis of the last syncytial cycles difficult (Takada et al., 2007). In *chk1 chk2* mutants these developmental defects are greatly ameliorated (Takada et al., 2007). Embryos mutant for *chk1* and *chk2* fail to slow Cdk1 activation in S-phase, resulting in premature mitotic entry and the completion of two extra syncytial cycles (Figure 10A in this Dissertation and Movie S3 in Deneke et al., 2016) (Fogarty et al., 1997; Sibon et al., 1997). Notably, *chk1 chk2* embryos do not display biphasic Cdk1 activation (Figures 10A, 10C), and wave propagation does not slow during cycles 10-13 (Figure 10E). A similar behavior was observed in embryos mutant for *wee1* (Figures 10B, 10D-E) (Price et al., 2000), a downstream effector of Chk1 (Farrell and O'Farrell, 2014; Morgan, 2007). These findings suggest that the increase in DNA content during the developmental cycles activates the DNA replication checkpoint to slow Cdk1 activation and thereby reduce the speed of the waves. To test this idea, we modified the DNA content of the embryos using compound chromosomes (Merrill et al.,

1988). As predicted, k_s (the rate of Cdk1 activation in S-phase) is inversely proportional to DNA content, and cell cycle duration increases with DNA amount (Figure 10F).

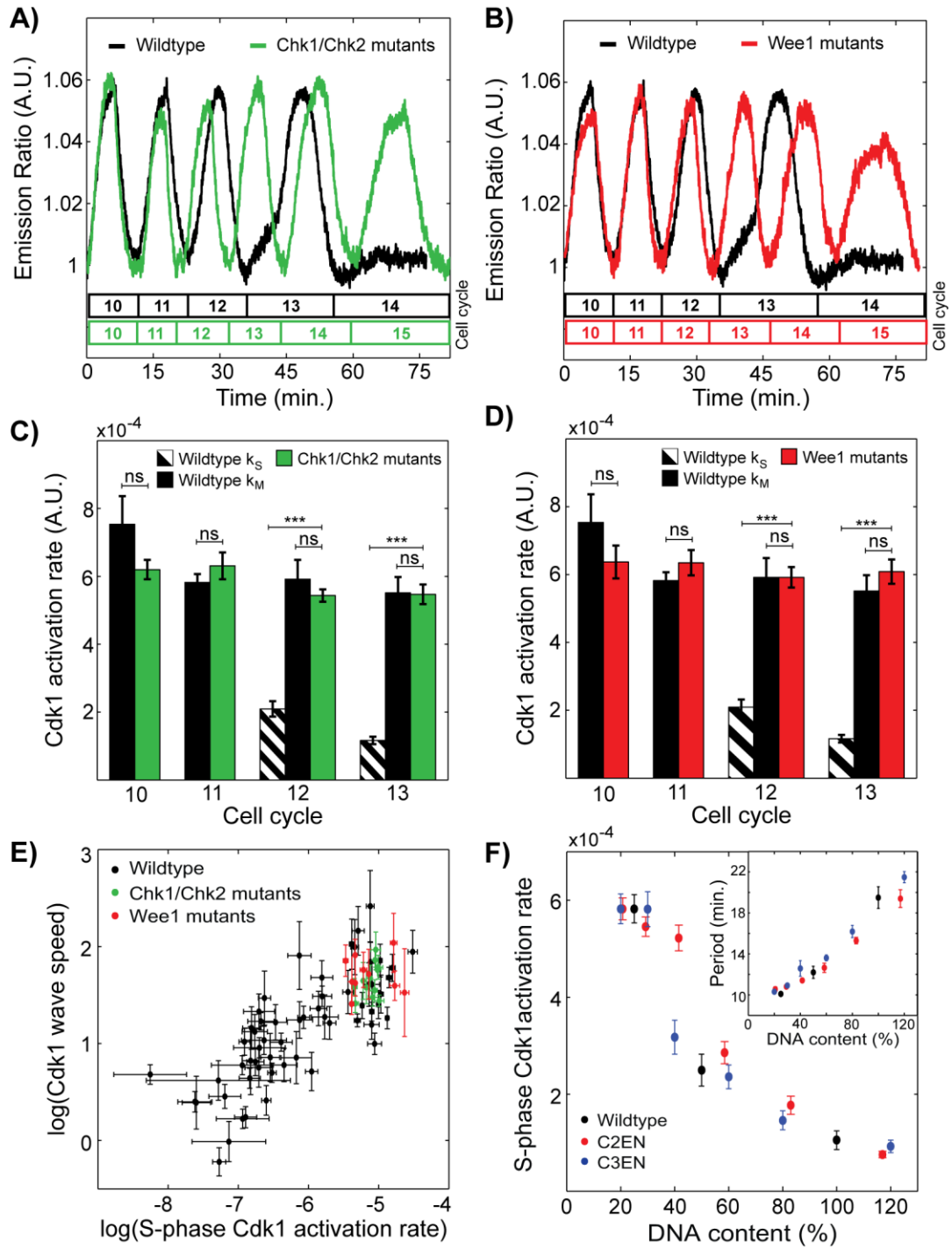


Figure 10: Cdk1 waves are dependent on the Chk1/Wee1 pathway and on DNA content. (A-B) Emission ratio of Cdk1 sensor for wildtype embryos (black line), chk1 chk2 embryos (A, green line), and wee1 embryos (B, red line). (C-D) Average Cdk1

activation rate per cell cycle for wildtype (black), *chk1 chk2* (C, green) embryos, and *wee1* embryos (D, red). Error bars, s.e.m. (E) Log-log plot of Cdk1 speed versus S-phase Cdk1 activation rate for wildtype (black), *chk1 chk2* (green), and *wee1* (red) embryos. Error bars, 95% CI. (F) S-phase Cdk1 activation rate as a function of DNA content. Inset, cell cycle period, marked from anaphase start time of one cycle to the next, as a function of DNA content. 100% indicates the DNA content of wild type embryos at cycle 13. ***, $p < 0.0001$; ns, not significant.

2.3.4 A Cdk1/Chk1 double negative feedback controls Cdk1 waves

To gain quantitative insights on the dynamics of Chk1, we engineered a localization sensor that responds primarily to its activity during cell cycles 12 and 13. We fused a peptide from human Cdc25C (amino acids 183-251), which contains an NLS, NES and a Chk1 phosphorylation site (Serine 216) to EGFP (Figure 11A). Phosphorylation of S216 triggers the binding of 14-3-3, which masks the NLS downstream of Serine 216 decreasing the nuclear import rate (Perry and Kornbluth, 2007). An NES sequence upstream of Serine 216 mediates nuclear export (Perry and Kornbluth, 2007). We found that cytoplasmic-to-nuclear ratio (C/N) of the sensor increases from cycle 11 to cycle 13 (Figure 11B), which is consistent with an increase of Chk1 activity. To determine whether the sensor responds primarily to Chk1 activity at cycles 12 and 13, we compared its localization dynamics to that of a sensor in which Serine 216 was mutated to Alanine (S216A). We also quantified the localization dynamics of the sensor in *chk1 chk2* mutants as well as under various genetic perturbations, which reduce or slightly increase the activity of Chk1 (Figure 11B and Figure 12A). Collectively, our experiments indicate that the increase in the nuclear exclusion of the sensor observed in cycles 12 and 13 is mainly dependent on Chk1

activity. The sensor undergoes a rapid nuclear import at the onset of mitosis, which precedes nuclear envelope breakdown by about one minute (Figure 12B). To confirm that this rapid nuclear import reflects a rapid inactivation of Chk1 at completion of S-phase, we forced embryos to enter mitosis in the presence of high Chk1 activity, established through injection of mRNA encoding for a constitutively active Chk1 mutant (Chk1-CA) (Wang et al., 2012). The sensor enters nuclei very slowly at the onset of mitosis (Figure 11C), consistent with a role of Chk1 in slowing down the rate of import of the sensor. Expression of Chk1-CA results in longer cell cycles (about 30 min compared to 12 min for cycle 12) with a significant contribution to cell cycle lengthening from a longer mitosis (Figure 12C). This is in agreement with the notion that inactivation of Chk1 is required for rapid mitosis. Based on all these observations, we conclude that the rapid import of the Cdc25¹⁸³⁻²⁵¹-EGFP sensor reflects the rapid inactivation of Chk1 at the onset of mitosis.

Using the biosensor described above, we established that the activity of Chk1 increased at cycles 12 and 13 relative to cycle 11 (Figure 11B). Chk1 activity plummets about one minute prior to nuclear envelope breakdown (Figure 1B and Figure 12B), indicating that Chk1 inactivation coincides with the abrupt activation of Cdk1 (Figure 11D). In fact, Chk1 inactivation propagates in a wave-like manner synchronized with the wave of Cdk1 activity (Figures 11E-F), arguing that Cdk1 triggers Chk1 inactivation, consistent with previous results (Yuan et al., 2012). Completion of S-phase coincides

with the time of Chk1 inactivation and propagates in the same wave-like pattern (Figure 11F: the wave of completion of S-phase precedes the waves of mitotic entry and mitotic exit by about 1 and 5 minutes, respectively). These observations suggest that Cdk1 negatively regulates Chk1 through its ability to promote completion of S-phase (Farrell et al., 2012), removing the DNA replication checkpoint stimulus. We also found that the nuclear levels of Chk1 start decreasing about a minute prior to mitosis (see Figure 12B), a process which might contribute to the reversal of the DNA replication checkpoint. We propose that a double-negative feedback between Cdk1 and Chk1 is the molecular mechanism that initiates the spreading of the Cdk1 waves at cycle 12 and 13 and controls their physical properties.

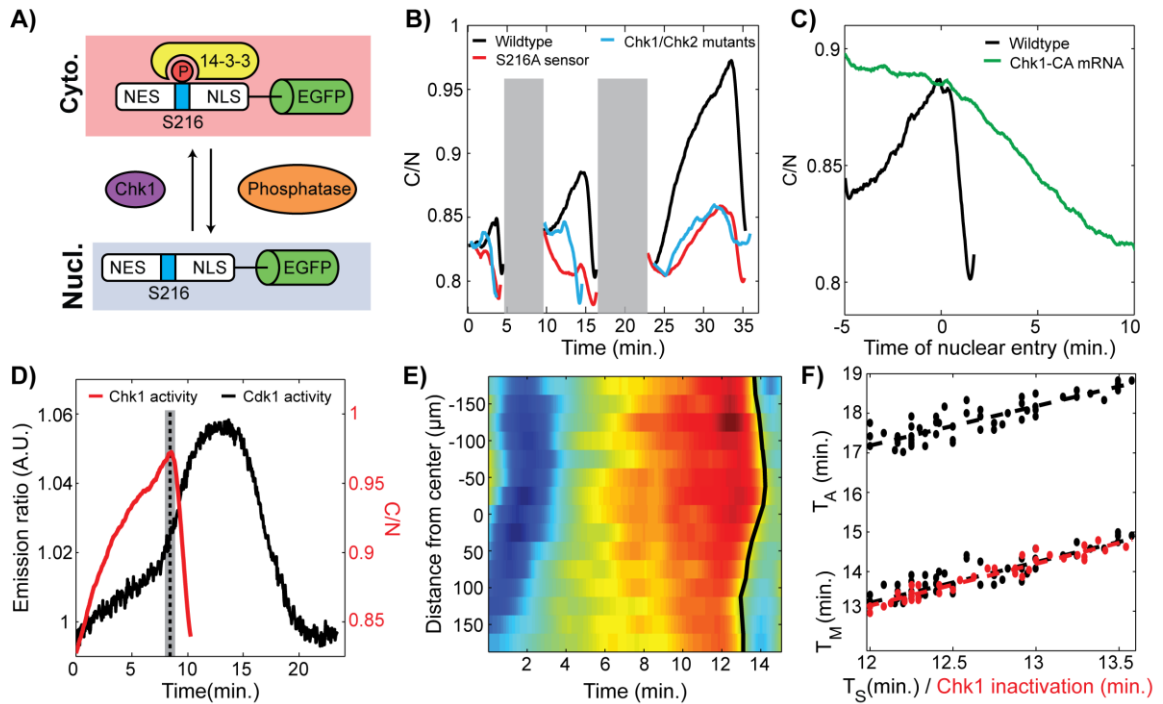


Figure 11: A Cdk1/Chk1 double negative feedback controls Cdk1 waves. (A) Schematic view of Chk1 localization sensor. The cytoplasmic to nuclear ratio provides a readout of Chk1 activity. (B) Cytoplasmic to nuclear intensity ratio of the Chk1 sensor in wild type (black), mutant sensor (S216A; red line), and *chk1 chk2* mutants (blue line) for cycles 11-13. In order to compare cell cycles of similar durations, we used cycle 15 (instead of cycle 13) for *chk1 chk2* mutants. Gray shaded box represents mitosis, when the absence of nuclear envelope precludes a reliable measure of the C/N ratio. (C) C/N ratio for a cycle 12 wild type and an embryo injected with Chk1-CA mRNA. (D) Average Cdk1 and Chk1 activities at cycle 13 measured in two different embryos. Dotted line, completion of S-phase. (E) Heat-map of Chk1 activity over time and along the anterior-posterior (AP)-axis of an embryo. Black line, Chk1 inactivation wave front. (F) Time of entry into mitosis (T_M) and anaphase start time (T_A) as a function of the time of completion of S-phase (T_S) (black line) and Chk1 inactivation (red line). Slopes: 1.0 ± 0.1 .

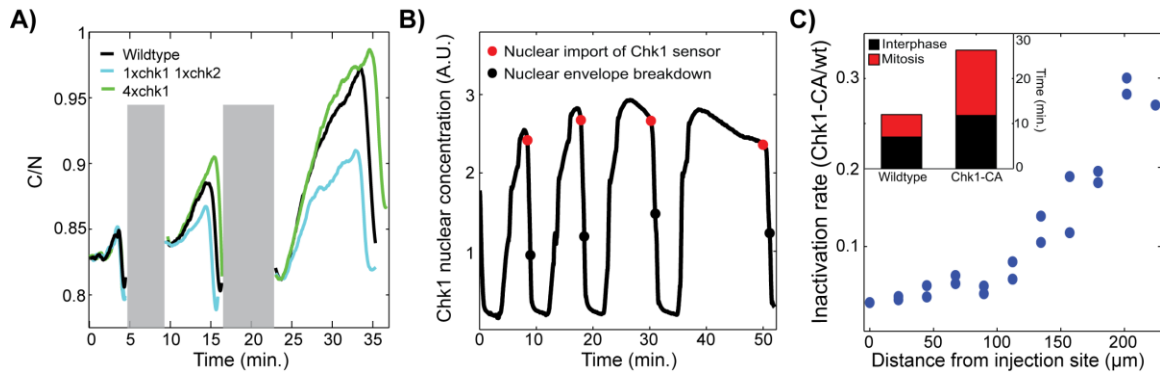


Figure 12: Validation of the Chk1 sensor. (A) Cytoplasmic to Nuclear (C/N) intensity ratio of the sensor ratio in wild type vs. *1xchk1 1xchk2* (blue) and *4xchk1* (green) mutants.

One copy of Chk1-TagRFP-T expressed from the maternal tubulin promoter -and spaghetti squash 3' UTR- should result in Chk1 protein levels similar to wild type levels. Embryos expressing Chk1-TagRFP-T were therefore labelled as *4xchk1*. Grey shaded box represents mitosis, when the absence of nuclear envelope precludes a reliable measure of the C/N ratio. (B) Chk1 nuclear concentration using a Chk1-TagRFP-T construct- as a function of time (cycles 10-13). The red and black dots indicate the time of inactivation of the sensor and of nuclear envelope breakdown. (C) The rate of inactivation of the sensor is inversely proportional to the distance from the site of injection of Chk1-CA mRNA.

Inset: estimated cell cycle duration for wild type and Chk1-CA.

2.3.5 Mitotic switch ensures rapid activation of Cdk1 during mitosis but does not regulate S-phase Cdk1 activation rate

Previous studies implicated positive feedback among Cdk1, Cdc25 and Wee1 as providing the bistability necessary for propagation of mitotic waves in *Xenopus* (Chang and Ferrell, 2013; Novak and Tyson, 1993). Positive feedback is due to Cdk1-mediated phosphorylation of Wee1 and Cdc25. To test the role of this regulation in *Drosophila* embryos, we generated feedback-deficient embryos that lack the relevant phosphorylation sites. Wee1-9A and Twine-3A (Twine and String are the two Cdc25 phosphatases in *Drosophila* embryos) have all of the putative Cdk1 sites mutated to nonphosphorylatable residues (Di Talia and Wieschaus, 2012; Harvey et al., 2011;

Pomerening et al., 2005). We focused on Twine because String is degraded earlier than Twine, which makes Twine the major phosphatase that controls cell cycle 13 (Di Talia et al., 2013; Farrell and O'Farrell, 2013). Embryos mutant for endogenous *wee1* and *twine* (but expressing *Wee1-9A* and *Twine-3A*) lack the Cdk1/*Wee1*/*Cdc25* feedback at cycle 13. We found that the rate of Cdk1 activation during mitotic entry is reduced 2-3 fold at cycle 13 (Figures 13A-B and Figure 14, confirming that the positive feedback in the mitotic switch is required for the abrupt activation of Cdk1 in mitosis. Conversely, the activation of Cdk1 during S-phase is unaffected and remained smaller than the mitotic activation rate. Notably, Cdk1 waves still propagate, although with a speed slower than wild-type (Figure 13C in this Dissertation and Movie S4 in Deneke et al., 2016). We conclude that the positive feedback through *Wee1*/*Cdc25* phosphorylation is required for the invariant mitotic activation rate of Cdk1, which in turn ensures that the speed of the wave is not altered by changes in mitotic rates but is controlled by the rate of Cdk1 activation in S-phase. We observe that embryos in which only one of the two feedbacks is abrogated show intermediate phenotypes and demonstrate that the double negative feedback between Cdk1 and *Wee1* plays a stronger role than the feedback between Cdk1 and Twine (Figure 14).

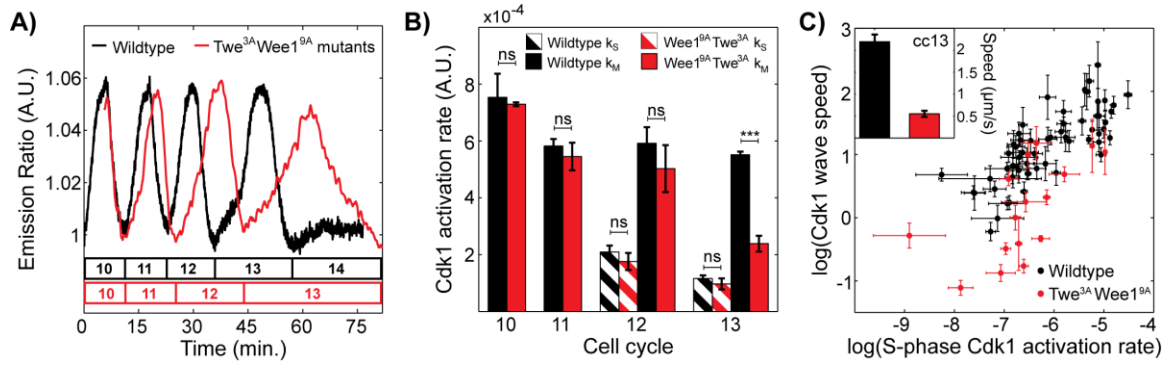


Figure 13: Mitotic switch ensures rapid activation of Cdk1 during mitosis but does not regulate S-phase Cdk1 activation rate. (A) Emission ratio of Cdk1 sensor for wildtype embryos (black line) and *twine-3A wee1-9A* embryos (red line). (B) Average Cdk1 activation rate per cell cycle for wildtype (black) and *twine-3A wee1-9A* (red) embryos. Error bars, s.e.m. (C) Log-log plot of Cdk1 speed versus S-phase Cdk1 activation rate for wildtype (black) and *twine-3A wee1-9A* (red) embryos. Error bars, 95% CI. Inset, Cdk1 wave speed of wildtype (black) and *twine-3A wee1-9A* (red) embryos at cycle 13. Error bars, s.e.m. ***, $p < 0.0001$; ns, not significant.

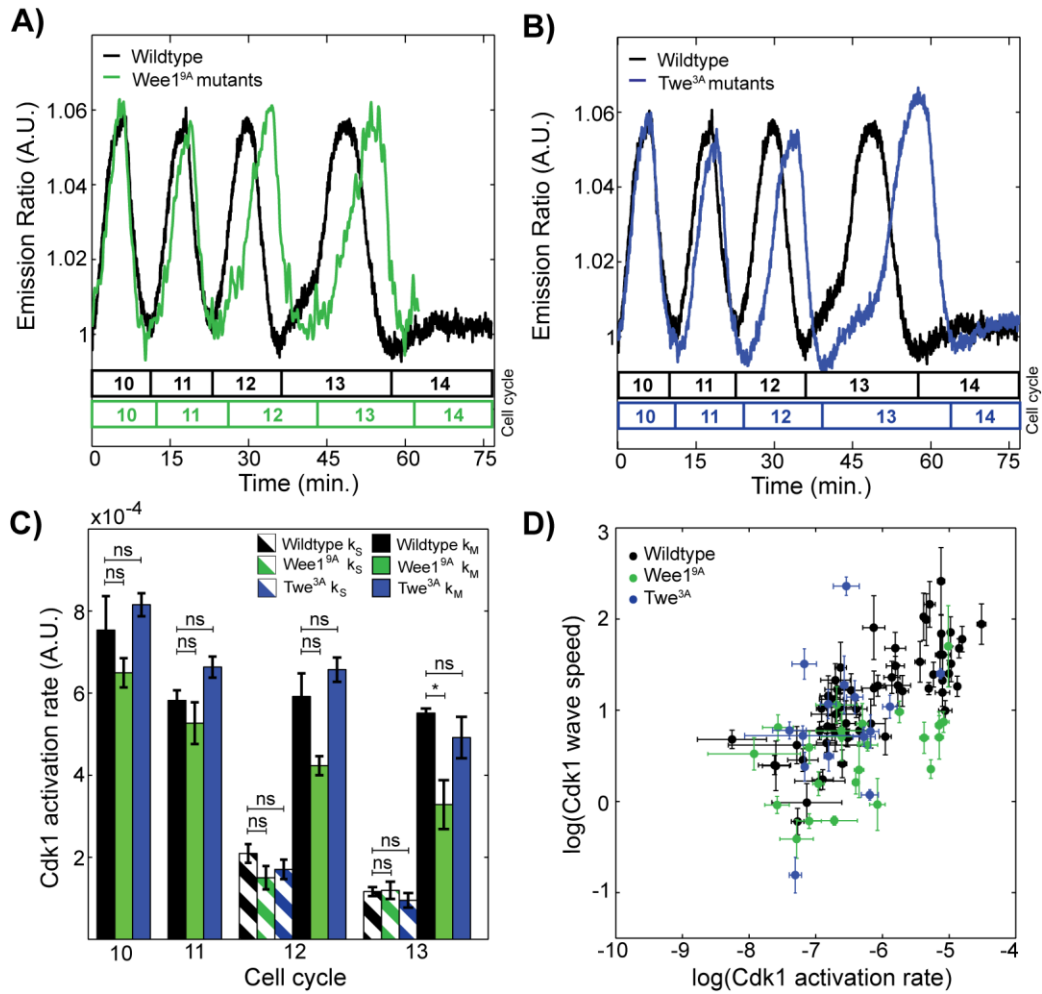


Figure 14: Positive feedback from the Cdk1 mitotic circuit regulates abruptness of Cdk1 activation. (A) Emission ratio of Cdk1 sensor for wildtype embryos (black line) and *wee1^{9A}* embryos (green line). (B) Emission ratio of Cdk1 sensor for wildtype embryos (black line) and *twe^{3A}* embryos (blue line). (C) Average Cdk1 activation rate per cell cycle for wildtype (black), *wee1-9A* (green), and *twine-3A* (blue) embryos. Error bars, s.e.m., ***, $p < 0.0001$; *, $p < 0.05$; ns, not significant. (D) Log-log plot of Cdk1 speed versus S-phase Cdk1 activation rate for wildtype (black), *wee1-9A* (green), and *twine-3A* (blue) embryos. Error bars, 95% CI.

2.3.6 A new physical mechanism for the generation of waves captures the properties of Cdk1 waves

To gain further insight into the nature of the mitotic waves, we built a mathematical model for Cdk1 dynamics. Bistability coupled with diffusion provides the classical mechanism that triggers chemical waves (Tyson and Keener, 1988; van Saarloos, 1998). This can be understood intuitively as follows. When a region of the embryo transitions from a low state of Cdk1 activity to a high state, diffusion of active Cdk1 can initiate a similar transition in a neighboring region, which can then spread to another region and thereby generates a traveling wave. By plotting the time evolution of experimental Cdk1 profiles, a bistable wave should display a stable state of Cdk1 (upper) invading a metastable one (lower). Nonetheless, profiles in wild-type embryos (Figure 15A) differed from a bistable front, which is visible in Figure 15B (obtained for mutants of the mitotic switch). In particular, the levels of activity at the left/right ends in Figure 15B (which correspond to the metastable/stable points of the corresponding bistable system) are roughly unchanged in time while a front progresses. Conversely, the wild-type profiles do not show any sign of invasion by a stable phase of a metastable one. Therefore, two distinct regimes were found for Cdk1 waves in *Drosophila* embryos: a traditional bistable front in the mitotic switch mutants and sweeping gradient of Cdk1 activity in the wildtype case. This led us to develop a theory of waves consisting of a time-dependent reaction–diffusion model that would capture both experimental regimes

observed in *Drosophila* embryos (for details on mathematical model see Vergassola et al., 2018).

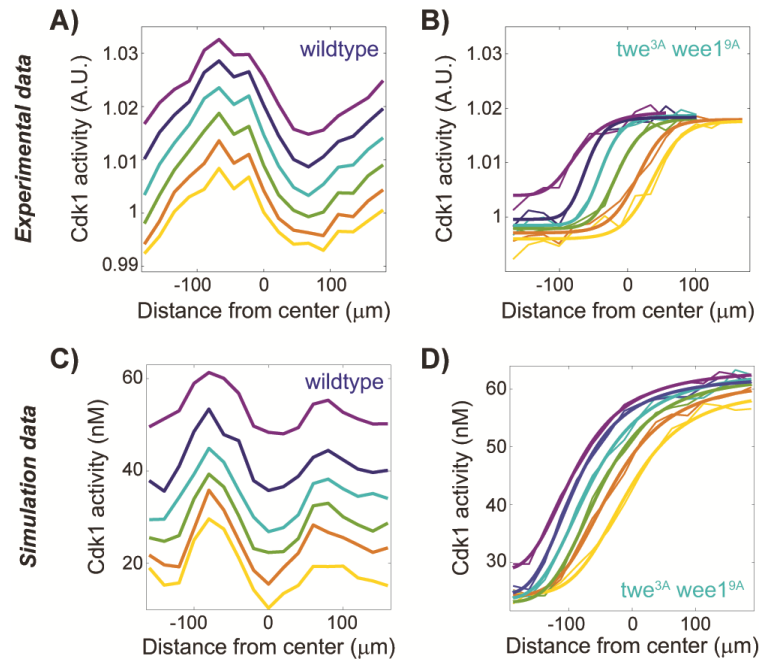


Figure 15: Spatiotemporal patterns of Cdk1 activity differ in wild type and mutants of the mitotic switch. (A) In the wild type, the Cdk1 activity grows synchronously, with minor distortions of the gradients. (B) In the mutant lacking the mitotic switch feedbacks, a sharp front propagates across the embryo. (C and D) The reaction–diffusion model of Cdk1 activity recapitulates experimental observations.

A time-dependent reaction diffusion model that incorporates the regulatory interactions among Cdk1, the phosphatases Cdc25, the kinase Wee1, and the checkpoint kinase Chk1 captured the Cdk1 dynamics observed both in the wild type and the mitotic switch mutant (Figure 15C-D). Furthermore, by comparing the range of wave speeds predicted by a bistable model compared to a time-dependent reaction diffusion model we observed that the maximum speed achieved by a bistable wave remained severalfold slower than waves from our simulation (Figure 16). This suggested that bistable waves

are too slow to account for the speed of the Cdk1 waves observed *in vivo* and that instead, a transiently-bistable reaction diffusion model can account for the spreading of Cdk1 waves in *Drosophila* embryos. We called the waves that arise from this model “sweep waves”, due to the sweeping gradients of Cdk1 activity that characterize the system.

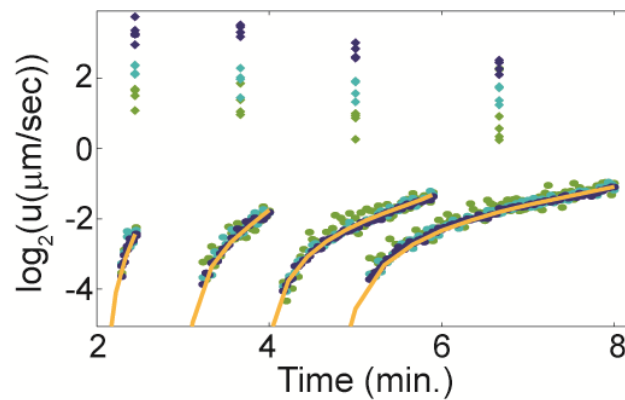


Figure 16: Bistable waves are slow compared to sweep waves. Circles show the speed of bistable waves measured in simulations in the presence of different noise levels; diamonds show the speed in simulations of a time-dependent reaction diffusion model for different noise levels.

In short, the spreading of sweep waves of Cdk1 activity in wild type embryos features three phases. During phase I, which corresponds to the beginning/middle S-phase of the cell cycle, Cdk1 gradients are formed and couple neighboring regions within the embryo (Figure 17A). During mid- to late S-phase of the cell cycle (Phase II), time-dependent effects become dominant and produce the upward sweep of the Cdk1 levels of activity (Figure 17B). The sweep is roughly uniform in space and therefore preserves the Cdk1 spatial gradients. Since gradients swept upward reach prescribed

levels with delays that vary roughly linearly in space, a wave-like spreading is produced, which accounts for experimental observations in wild type embryos. Finally, during the third phase (Figure 17C), which spans various phases of mitosis, the delays introduced during Phase I are preserved, as in Figure 17C Inset. Therefore, in the sweep wave model, coupling of neighboring regions occurs in Phase I or S-phase and all events that follow simply reflect the delays introduced in S-phase.

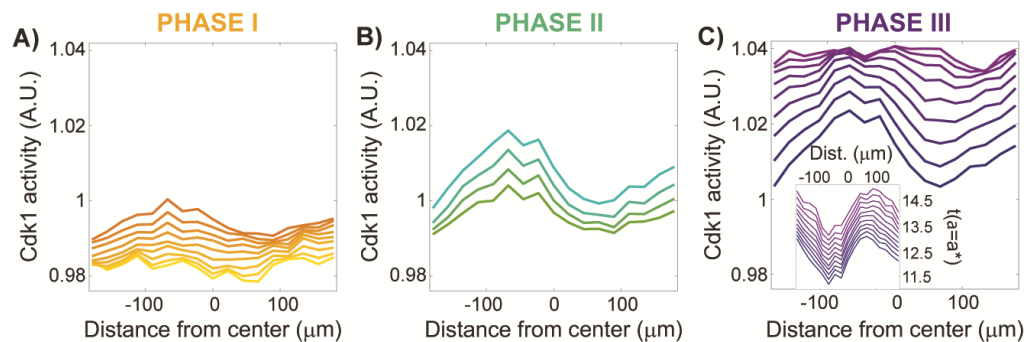


Figure 17: The dynamics of Cdk1 over a single cell cycle display three distinct phases. (A) Temporal evolution of Cdk1 activity (from experimental data) as a function of space demonstrates the formation of gradients of increasing length. (B) Temporal evolution of Cdk1 activity (from experimental data) as a function of space demonstrates that gradients are swept up largely undeformed during this phase. (C) Temporal evolution of Cdk1 activity (from experimental data) as a function of space demonstrates that gradients change, yet the time delays among different spatial points to reach a given Cdk1 threshold of activity are conserved (Inset).

2.3.7 S-phase waves are generated by an active mechanism, while anaphase waves are a kinematic and passive process

Nuclear cycles are completed by mitotic exit events, which are initiated by a decline in Cdk1 activity. Positive feedback mechanisms sharpening the metaphase-anaphase transition (Holt et al., 2008; Ishihara et al., 2014; López-Avilés et al., 2009) raise the possibility that, like the S-phase Cdk1 waves, the anaphase waves also propagate as

chemical trigger waves. If that were the case, then any slowing of anaphase waves in successive cycles should be accompanied by changes in the Cdk1-inactivation reactions. However, we found that the rate of Cdk1 inactivation is invariant (Figure 19), yet anaphase waves display the same slowing observed for completion of S-phase and mitotic entry in different cycles (Figure 11F). The previous observations and the analysis of our mathematical model suggest that S-phase Cdk1 waves are sweep waves, while anaphase waves are phase waves. Phase I of sweep waves involves the catalytic production of a propagating species and its diffusion into neighboring regions (Figure 18A). Conversely, phase waves are kinematic, and just reflect pre-defined delays (Figure 18A). In our case, delays are those set by the Cdk1 waves in the S-phase, which explains the strong correlation of velocities in Figure 6H.

The different nature of active and phase waves is highlighted by placing a physical barrier along the path of the wave. The barrier is expected to impede the propagation of an active wave, but not of a phase wave (Figures 18B-C). We modified the design of a micromanipulator for surgical ligations of embryos (Newman and Schubiger, 1980; Sander, 1971) in order to be able to introduce a barrier with a temporal resolution of about 1 minute in embryos expressing the Cdk1 sensor and His2Av-mRFP. To test whether our predictions were correct, we used this setup to introduce a barrier between two regions of the embryo either during S-phase (to block Cdk1 waves) or M-phase (to test whether or not anaphase waves would be blocked). When the barrier was

introduced during interphase, the two sides of the embryo became asynchronous (Figure 18D in this Dissertation and Movie S5 in Deneke et al., 2016). Conversely, when the barrier was introduced at the onset of mitosis, the anaphase wave travelled unperturbed through the barrier (Figures 18E-F in this Dissertation and Movie S6 in Deneke et al., 2016). These observations confirm our predictions and demonstrate that the wave of anaphase is indeed a kinematic wave (phase wave), which reflects the delays set by the active wave that synchronizes the S-phase. In other words, introducing a physical barrier between two embryonic regions during S-phase prevented the buildup of a Cdk1 gradient across the two regions, which resulted in an impeded mitotic wave.

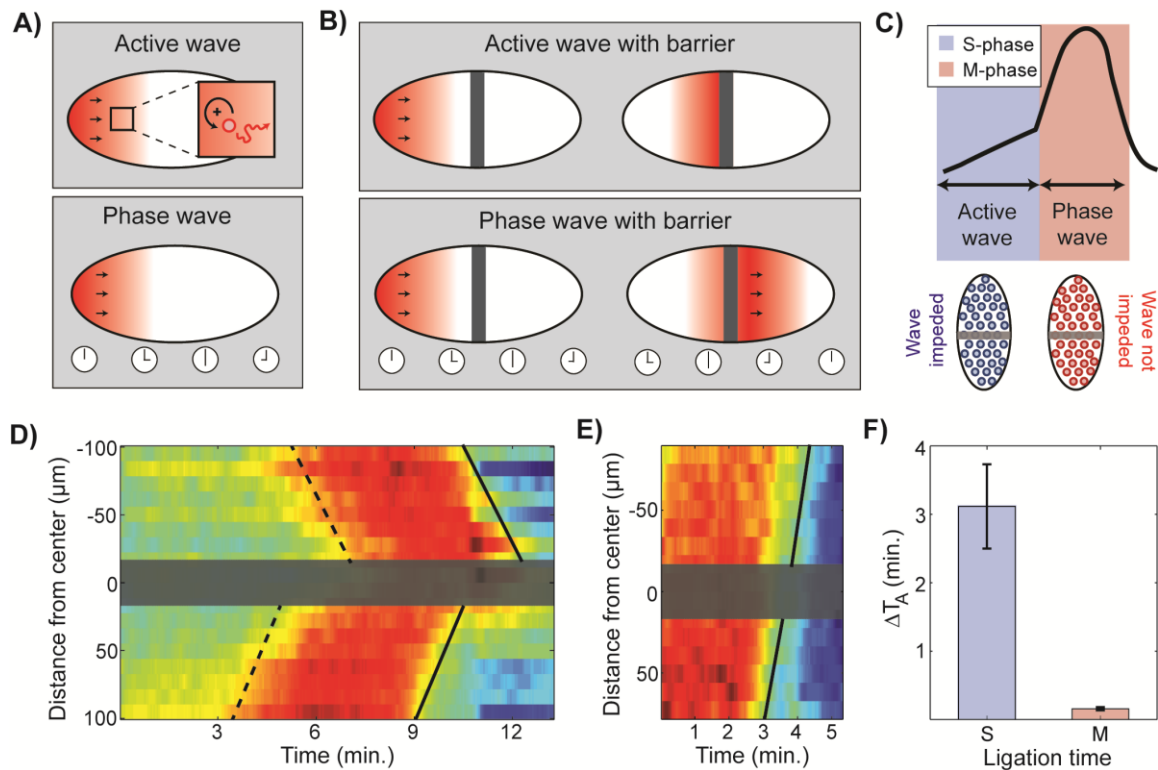


Figure 18: Mitotic waves are kinematic phase waves.(A) Schematic of the difference between active waves and phase waves. Active waves involve the transport or diffusion (red line) of material from one neighboring region to another, and depend on positive feedback loops (black circular arrow), which ensure the rapid production of the diffusing species. Phase waves are kinematic phase waves that reflect a delay in timing between neighboring regions (bottom panel). (B) The difference between an active wave and a phase wave becomes evident when an impermeable barrier is introduced. An active wave is blocked when a barrier is present (top panel), whereas a phase wave is unaffected (bottom panel). (C) Schematic of our prediction that synchronization of mitosis should be disrupted if an impermeable barrier is introduced during S-phase (prior to the S-phase Cdk1 active wave) and be unaffected if a barrier is introduced during M-phase. (D-E) Heat-map of Cdk1 activity through time and across the anterior-posterior (AP)-axis of an embryo ligated during S-phase (D) or M-phase (E), respectively. Gray box, ligation barrier; dotted line, prophase wave front; solid line, anaphase wave front. The continuity in (E) of the lines on the two sides of the barrier demonstrates that mitotic waves are indeed phase waves. (F) Anaphase delay (computed as the difference in anaphase time on the two sides of the barrier) caused by the introduction of a barrier in S-phase or M-phase. Error bars, s.e.m.

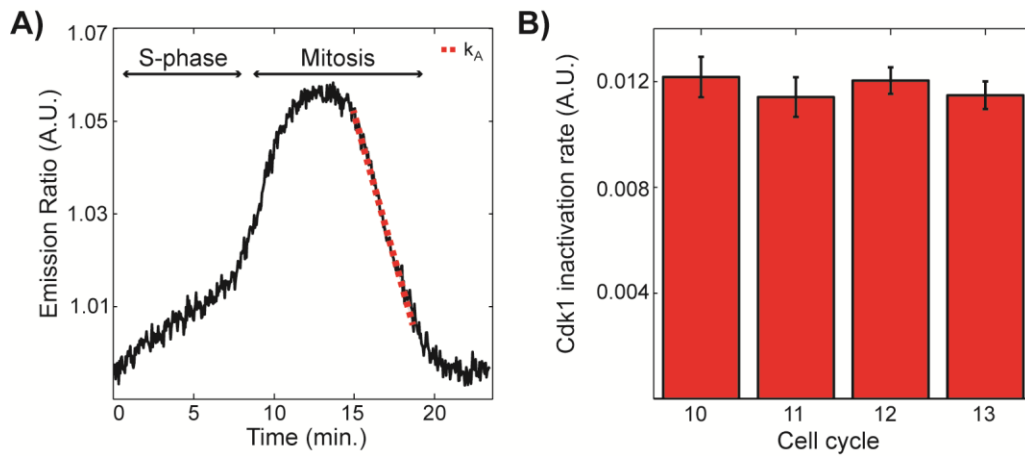


Figure 19: The rate of inactivation of Cdk1 during anaphase does not change during development. (A) Emission ratio of Cdk1 sensor for cycle 13. The dotted line indicates the linear fit to extract the rate of Cdk1 inactivation. (B) Rate of Cdk1 inactivation as a function of cell cycle number. Error bars, s.e.m.

2.4 Discussion

2.4.1 Cell cycle synchronization through chemical waves of Cdk1 activity

The large size of embryos poses a major challenge for biological processes that need to be rapidly coordinated across the entire cell. While diffusion takes too long to transfer information across large embryos, chemical waves provide a physical mechanism that is poised to be much more rapid. Here, we have focused on how such waves synchronize the four cell cycles prior to the maternal-to-zygotic transition of the syncytial *Drosophila* embryo. Using surgical ligations, we have confirmed classical observations that physical uncoupling of two regions of the embryo can introduce a delay of several minutes in the time when embryos reach the maternal-to-zygotic

transition at cell cycle 14 (Edgar et al., 1986). During cell cycle 14, *Drosophila* embryos first undergo cellularization, a specialized form of cytokinesis enclosing nuclei in individual cells, and then begin gastrulation. Gastrulation requires an exquisite degree of spatiotemporal coordination of cellular dynamics. We propose that mitotic waves during the syncytial cell cycles are necessary to ensure that all the cells in the embryo enter cycle 14 at about the same time, enabling proper coordination of gastrulation.

We have shown that cell cycles 10-13 in *Drosophila* embryos are synchronized by waves of Cdk1 activity. These waves were first proposed as a mechanism for the synchronization of mitosis in the *Xenopus* egg extract system (Chang and Ferrell, 2013), but we provide the first direct evidence for such waves using a FRET-based biosensor of Cdk1 activity (Gavet and Pines, 2010b). In contrast to the proposed role of the mitotic switch in *Xenopus*, in *Drosophila* embryos we found that the Cdk1 waves of cell cycles 12 and 13 propagate based on S-phase (and not M-phase) Cdk1 regulation. In fact, mitotic waves are not the result of an active mechanism, but simply a consequence of earlier differences in the timing of DNA replication. As a consequence, the speed of the Cdk1 and mitotic waves is controlled by the activity of Cdk1 during S-phase and is sensitive to the activity of the DNA replication checkpoint. We point out that, consistently with previous observations (Foe and Alberts, 1983), the slowdown of mitotic waves during *Drosophila* development is not accompanied by a slowdown in the duration of mitotic processes (which likely depend on the mitotic rate of activation of Cdk1). This

observation was previously taken as evidence that the mechanism generating the mitotic waves could be of a mechanical nature, reflecting the decrease in inter-nuclear distance that occurs as nuclei proliferate (Idema et al., 2013). Our results have provided a different explanation for the slowdown of mitotic trigger waves, based on the reduced chemical rates of Cdk1 activation during the S-phase (Edgar et al., 1986; Farrell and O'Farrell, 2014; Price et al., 2000; Stumpff et al., 2004) which is consistent with a role for Cdk1 waves in the synchronization of the cell cycle. Furthermore, the observation that mutants, such as *wee1*, that specifically affect Cdk1 activity (Morgan, 2007; Price et al., 2000), alter the speed of mitotic waves in a quantitatively predictive manner argues against the existence of a mechanical signal upstream of Cdk1 activity that triggers the mitotic waves.

Furthermore, we have shown that Cdk1 waves spread as sweep waves in the early *Drosophila* embryo that are characterized by a transiently bistable reaction-diffusion system. The above mechanism differs fundamentally from the coupling of bistability and diffusion proposed for *Xenopus* extracts (Chang and Ferrell, 2013) and has a major impact upon the waves' speed and its dependency on physical parameters. We speculate that sweep waves have evolved to ensure that cell cycles in the *Drosophila* syncytium are synchronized and completed in minutes rather than several tens of minutes, which the reduced drive of the S-phase and slower bistable waves would entail. It would be important to develop similar experimental tools for *Xenopus*, to

ascertain the nature of its Cdk1 and surface contraction waves. *In vitro* experiments using egg extracts show a wide range of wave speeds in *Xenopus laevis* and a substantial slowdown across the cycles, making it plausible that time-dependent mechanisms play a fundamental role.

By visualizing and quantifying the dynamics of Cdk1 and Chk1 waves, we have unraveled the molecular and physical mechanisms of collective synchronization of the cell cycle. Cdk1 activity forms gradients that couple neighboring regions in S-phase and is followed by a phase wave of mitotic events. We determined that the S-phase activity of Cdk1 and its interaction with the checkpoint effector kinase Chk1 is the primary positive feedback responsible for regulating the speed of the mitotic wave. Using a novel biosensor which responds primarily to Chk1 during the late syncytial cycles, we have shown that Chk1 activity decreases abruptly at completion of S-phase. Similar conclusions were reached by Yuan et al. who analyzed cell cycle dynamics upon cyclin knockdowns (Yuan et al., 2012). While the mechanisms triggering the decrease of Chk1 activity at completion of S-phase remain unclear, it is likely that mechanisms similar to the ones elucidated in mammalian cells might be at play (Zhang and Hunter, 2014). Once DNA replication is completed, Chk1 cannot be phosphorylated and activated by DNA damage. If the phosphatase(s) deactivating Chk1 is active at the end of S-phase, the checkpoint could be reversed very rapidly. Other mechanisms, e.g. the degradation of the DNA replication checkpoint factor Claspin and nuclear exclusion of Chk1, could

also contribute significantly to the rapid reversal of the DNA replication checkpoint (Zhang and Hunter, 2014).

The Cdk1 positive feedback through direct phosphorylation of Wee1 and Cdc25 does not control the activity of Cdk1 in S-phase, but is important to ensure a stereotypically rapid activation of Cdk1 upon entry into mitosis. This is at variance with the observations in *Xenopus* egg extract, where the positive feedbacks involved in the mitotic switch directly control wave propagation (Chang and Ferrell, 2013). We suggest that the mechanisms of cell cycle control are plastic and allow different levels of regulation.

2.4.2 Quantitative analysis of chemical waves during embryonic development

Dissecting the physical properties of the Cdk1 and mitotic waves required accurate measurements of Cdk1 activity with high spatiotemporal resolution. Such precise measurements gave us the possibility to quantitatively test ideas for the initiation and the spreading of the Cdk1 waves. This also led us to uncover a new physical mechanism by which Cdk1 activity spreads in the early *Drosophila* embryo called sweep waves. The mechanism hinges on time-dependent effects in a reaction–diffusion system, namely the fact that they can sweep the overall level of the Cdk1 field upward, while preserving its spatial gradients. The resulting waves are faster than those triggered by the invasion of a metastable state by a stable state (bistable waves).

Chemical waves have been described in a variety of biological systems and can be classified as active and phase waves (Winfree, 2001). While phase waves originate from kinematic mechanisms and just reflects pre-existing gradients in the underlying timing of events, active waves are generated by active mechanisms and require the propagation of physical information. Since the coupling of diffusion and positive feedback can generate chemical waves, it is likely that such waves generally emerge as an important feature for the coordination of cellular processes across large spatial scales. Our analysis demonstrates that biphasic regulation of Cdk1 activity uncouples the speed of Cdk1 waves from the regulation of mitotic Cdk1 activation. In principle, such uncoupling could allow biological systems to achieve an independent control of the speed of chemical waves and the rapidity of execution of cellular transitions. Whether this signaling feature is used for synchronization of cellular processes in large tissue remains to be established.

2.5 Experimental Methods

2.5.1 Plasmids

Plasmids were constructed using either standard ligation or Gibson assembly (NEB). The Cdk1-FRET sensor, the Chk1 sensor (human Cdc25C aa 183-251, fused to EGFP) and the Chk1-TagRFP-T construct were all cloned in plasmid pBabr containing the maternal Tubulin promoter and the spaghetti squash 3' UTR (gift of Yu-Chiun Wang and Eric Wieschaus, Princeton University). The PCNA-TagRFP-T plasmid was

generated by substituting the EGFP sequence with Tag-RFP-T sequence from a PCNA-EGFP plasmid (gift of Shelby Blythe and Eric Wieschaus, Princeton University). The *twine*^{3A} construct was generated starting from a rescue construct (Alphey et al., 1992) for *twine* (isolated from a Pacman BAC plasmid (CH322-159O07) by BamHI digestion) cloned in pBabr. A *twine* fragment in which the 3 putative Cdk1 sites (SP/TP) were mutated (AP) was synthesized (IDT) and cloned into the *twine* rescue construct. To generate the *wee1*^{9A} construct, we first generated a plasmid containing just the *twine* promoter and the *twine* 3'UTR from the *twine* rescue construct. The *wee1*^{9A} sequence (Di Talia and Wieschaus, 2012) was then inserted. Transgenic flies were generated by site directed integration of plasmids on various sites on the 2nd and 3rd chromosomes (atp40, VK1, attP2, VK5, VK33).

2.5.2 Stocks

Stocks were generated using standard methods. A list of stocks used in this Chapter is available in Table 2. To generate embryos with different DNA content we used homo compound chromosomes: C(2)EN and C(3)EN, in which both copies of chromosome 2 and 3 are fused together respectively. Analysis of cell cycle timing reveals two classes of embryos: embryos with shorter cell cycles than wild type (1 copy of chromosome 2 or 3) and embryos with longer cell cycle (3 copies of chromosome 2 or 3). To confirm that the cell cycle timing in fact correlates with chromosome copy number, we performed high resolution imaging of His2Av-mRFP, which allows the visualization

of the longer C(2)EN and C(3)EN chromosomes (Martins et al., 2013). The results were confirmed by analyzing embryos from crosses with a C(2)EN stock (BDSC #2974), which only gives embryos with one copy of chromosome 2 (Martins et al., 2013).

Table 2: List of stocks used in this Chapter

Experiment	Genotype
Cdk1 waves	w; Cdk1-FRET; His2Av-mRFP
Cdk1 waves	His2Av-mRFP; <i>grp</i> ²⁰⁹ <i>lok</i> ³⁰ / <i>grp</i> ^{z5170} <i>lok</i> ³⁰ ; Cdk1-FRET
Cdk1 waves	His2Av-mRFP; <i>wee1</i> ^{ES1} / <i>Df</i> (2L) <i>Dwee1</i> -W05; Cdk1-FRET
Cdk1 waves	w; Cdk1-FRET <i>twe</i> ^{HB5} <i>twe</i> ^{3A} ; His2Av-mRFP
Cdk1 waves	w; <i>wee1</i> ^{ES1} <i>twe</i> ^{HB5} <i>twe</i> ^{3A} / <i>Df</i> (2L) <i>Dwee1</i> -W05 <i>twe</i> ^{HB5} <i>twe</i> ^{3A} ; Cdk1-FRET His2Av-mRFP/ <i>twepr</i> - <i>wee19A</i>
Cdk1 waves	His2Av-mRFP; <i>wee1</i> ^{ES1} / <i>Def</i> (<i>wee1</i>); Cdk1-FRET/ <i>twepr</i> - <i>wee19A</i>
Cdk1 Diffusion	UAS-Cdk1-Venus/ <i>nos</i> -Gal4 (the UAS-Cdk1-Venus was a kind gift of Shelagh Campbell)
S-phase duration	w; His2Av-GFP; PCNA-TagRFP-T
Chk1 activity and waves	w; His2Av-mRFP/+; <i>Cdc25C</i> ¹⁸³⁻²⁵¹ -EGFP/+
Chk1 activity and waves	w; <i>grp</i> ²⁰⁹ <i>lok</i> ³⁰ / <i>grp</i> ^{z5170} <i>lok</i> ³⁰ ; <i>Cdc25C</i> ¹⁸³⁻²⁵¹ -EGFP/His2Av-mRFP
Chk1 activity and waves	w; <i>grp</i> ²⁰⁹ <i>lok</i> ³⁰ /+; <i>Cdc25C</i> ¹⁸³⁻²⁵¹ -EGFP/His2Av-mRFP
Chk1 activity and waves	w; +/ <i>grp</i> ^{z5170} <i>lok</i> ³⁰ ; <i>Cdc25C</i> ¹⁸³⁻²⁵¹ -EGFP/His2Av-mRFP
Chk1 activity and waves	w; <i>Cdc25C</i> ¹⁸³⁻²⁵¹ -EGFP/ <i>Chk1</i> -TagRFP-T
Cdk1 activity as a function of DNA content	w; Cdk1-FRET; His2Av-mRFP females crossed to C(2)EN males (stocks BDSC 2974, BDSC 1020 and BDSC 1112)
Cdk1 activity as a function of DNA content	w; Cdk1-FRET; His2Av-mRFP females crossed to C(3)EN males (stock BDSC 1117).

2.5.3 Microscopy

Imaging experiments were performed with an upright Leica SP8 confocal microscope, a 20X/0.75 numerical aperture oil-immersion objective, an argon ion laser,

and a 561-nm diode laser. For embryos expressing His2Av-RFP and Cdk1-FRET we acquired images (800x300 pixels) with a frame rate of 1/2.89s. For embryos expressing the Chk1 sensor, as well as embryos expressing the tagged Chk1 proteins, images were acquired with a frame rate of about 1/2s. For embryo expressing His2Av-GFP and PCNA-TagRFP-T, images were collected with a frame rate of about 1/0.7s.

2.5.4 FRAP experiments

The diffusion constants of Cdk1 and Chk1 were estimated by performing Fluorescence Recovery After Photobleaching (FRAP) experiments. Circular areas of 15 μm radius were bleached and the recovery of the fluorescence signal was acquired with a resolution of about 100 ms. Diffusion coefficients were estimated using an approach previously described (Brown et al., 1999).

2.5.5 Validation and characterization of Cdk1 FRET sensor

To validate the Cdk1 FRET sensor and to establish which cyclin-Cdk1 complexes phosphorylate the sensor in living *Drosophila* embryos, we performed single and pairwise knockdown of cyclins using double-strand RNA (dsRNA) injections. Knockdown of all three mitotic cyclins (CycA, CycB and CycB3) results in a low and constant FRET ratio, indicating that the oscillation in the emission ratio of the sensor is in fact due to changes in Cdk1 activity (Figure 7B). Furthermore, knockdown of Cyclin B or of any pair of cyclins still showed oscillations in the emission ratio of the sensor, supporting the idea that the sensor responds to all mitotic cyclins-Cdk1 complexes

(Figures 7B-C). The efficiency of the knockdowns was determined by the observed cell cycle lengthening which is consistent with previous reports (McClelland et al., 2009).

2.5.6 Data and image analysis

Cdk1 FRET curves were computed by taking the fluorescence intensity ratio of YFP signal over CFP signal averaged over the entire embryo or over vertical slices of a width of 22.4 μm . S-phase Cdk1 activation rates were computed by fitting a straight line through the first 2-3 minutes of Cdk1 activity increase. M-phase Cdk1 activation rates were computed in a similar manner, fitting a straight line through a time interval of 2-3 minutes after Cdk1 inflection point. To estimate nuclear and cytoplasmic Cdk1 activities, nuclei were segmented with custom-made MATLAB software. Cytoplasmic activity was calculated by inverting nuclear masks. Completion of S-phase was interpreted to be the time at which PCNA foci disappeared. This time was estimated from changes in the coefficient of variation of PCNA-TagRFP intensity signal in each nucleus (Figure 9). The cytoplasmic to nuclear ratio of the Chk1 sensor was estimated by measuring nuclear signals from segmenting nuclei and cytoplasmic signals from rings 2 pixels-wide at 2 pixels-distance from the nuclear border (generated through dilation of the nuclear masks).

2.5.7 Computational method to calculate Cdk1 and mitotic wave speeds

To measure the speed of Cdk1 and mitotic waves, we developed a computational method that extracts the speed based on delays in Cdk1 activity or mitotic events at

different regions of the embryo. In the Supplemental Information we demonstrate that the Cdk1 and mitotic waves are well approximated by one dimensional waves spreading along the anterior-posterior (AP) axis. Therefore, we start by dividing the embryo in 20 regions across that axis (Figure 7D). We then estimate the activity of Cdk1 and the geometrical properties (aspect ratio) of nuclei for each region separately (Figure 6 and Figure 7E-F). To estimate the delays of each region relative to the region where the Cdk1 wave originated, we computed correlation coefficients comparing the dynamics of Cdk1 or of the morphological changes of nuclei in a given region to the ones in the region where the wave originated (Figure 7G). The time-dependence of this correlation was examined by temporally shifting the data sets relative to each other. The delay was estimated as the time shift that gave the maximum correlation of the two dynamics (Figure 7G). Using a linear fit of the delay as a function of the distance from the wave center (Figure 6G), we extracted the speed as the inverse slope of such fit.

2.5.8 Embryo manipulations

Embryos were collected on apple juice agar plates after 0-2 hours at 25°C. Following collection, embryos were dechorionated with 50% bleach for 1 minute and rinsed with water. For injections, embryos were aligned on agar plates using a metal probe and transferred to cover slips lined with double-sided tape, desiccated for 7-9 minutes and then covered with 700 Halocarbon oil (Sigma Aldrich). Double-stranded RNA was injected at a concentration of 0.5 mg/ml. For permanent embryo ligations, a

dull razor blade was lowered onto desiccated embryos aligned on double-sided tape with a micromanipulation apparatus previously described (Sander, 1971). After 10 minutes, the blade was removed and the slide was transferred to the microscope for imaging. For ligations performed during imaging, we used a modified micromanipulation apparatus, which allowed us to raise a dull razor blade onto accurately staged embryos glued to a glass slide.

2.5.9 Production of dsRNA

Double-stranded RNA (dsRNA) was synthesized by *in vitro* transcription of a DNA template containing the T7 promoter sequence on both ends. Amplicons for each cyclin from the Drosophila RNAi Screening Center (DRSC) (Cyclin A: DRSC 11123, Cyclin B: DRSC 04605, Cyclin B3: DRSC 16618) were PCR-amplified using Herculanase II Fusion DNA polymerase. Amplified DNA templates were *in vitro* transcribed (Ambion Megascript Kit) and diluted to a final concentration of 1mg/ml.

3. Self-organized nuclear positioning synchronizes the cell cycle in *Drosophila* embryos

Chapter 3 was modified from a manuscript (of the same title) accepted for publication in *Cell* in January 2019. The authors were Victoria E. Deneke, Alberto Puliafito, Daniel Krueger, Avaneesh V. Narla, Alessandro De Simone, Luca Primo, Massimo Vergassola, Stefano De Renzis and Stefano Di Talia. This project was conceptualized by Victoria E. Deneke, Alberto Puliafito, Massimo Vergassola and Stefano Di Talia. The optogenetic experiments were performed in collaboration with Stefano De Renzis at EMBL Heidelberg by Victoria E. Deneke and Daniel Kruger. Simulations and mathematical models were developed by Avaneesh V. Narla, Stefano Di Talia and Massimo Vergassola. In addition, I would like to thank Anna Chao and Maggie Xing for help with experiments, and Daniel Lew, Jonathon Pines and Eric Wieschaus for scientific discussions on this project. Finally, I'd like to thank Sharyn Endow, Brigid Hogan, Bernard Mathey-Prevot and members of the Di Talia lab for comments on the manuscript.

3.1 Summary

The synchronous cleavage divisions of early embryogenesis require coordination of the cell cycle oscillator, the dynamics of the cytoskeleton and the cytoplasm. Yet, it remains unclear how spatially restricted biochemical signals are integrated with physical properties of the embryo to generate collective dynamics. Here, we show that synchronization of the cell cycle in *Drosophila* embryos requires accurate nuclear

positioning, which is regulated by the cell cycle oscillator through cortical contractility and cytoplasmic flows. We demonstrate that biochemical oscillations are initiated by local Cdk1 inactivation and spread through the activity of phosphatase PP1 to generate cortical myosin II gradients. These gradients cause cortical and cytoplasmic flows that control proper nuclear positioning. Perturbations of PP1 activity and optogenetic manipulations of cortical actomyosin disrupt nuclear spreading, resulting in loss of cell cycle synchrony. We conclude that mitotic synchrony is established by a self-organized mechanism that integrates the cell cycle oscillator and embryo mechanics.

3.2 Introduction

Embryonic development is controlled by dynamic biochemical signals which trigger changes in the organization of the cytoskeleton and of the cytoplasm, and thereby of the mechanical properties of the embryo (Gilmour et al., 2017; Gross et al., 2017). Changes in the physical properties of the embryo can, in turn, feedback to biochemical dynamics, suggesting that morphogenesis requires the integration of biochemical and mechanical signals, possibly through the generation of self-organized circuits (Gross et al., 2017; Maitre et al., 2016; Samarage et al., 2015). However, the molecular principles underlying this integration remain poorly understood, making it difficult to quantitatively and predictably describe embryonic development on a macroscopic scale.

A powerful model system to dissect the integration of biochemistry and mechanics during morphogenesis is provided by the cleavage divisions of the *Drosophila* embryo. After fertilization, the fruit fly embryo undergoes 13 rounds of DNA replication and mitosis without cytokinesis, resulting in a multinucleated syncytium containing about 6,000 nuclei (Farrell and O'Farrell, 2014; Rabinowitz, 1941) (Figure 20A). These nuclear cycles are controlled by oscillations in the activity of cyclin-dependent kinase 1 (Cdk1) and mitotic phosphatases, PP1 and PP2A (Heim et al., 2017; Mochida et al., 2010; Morgan, 2007; Wu et al., 2009). The first cleavage divisions are accompanied by a series of nuclear movements; by cycle 10, movements result in a hollow shell at the surface of the embryo where nuclei are uniformly distributed (Figure 20A) (Foe and Alberts, 1983). Following the first 3 rounds of division, where no significant nuclear movement is observed, nuclei spread along the anterior-posterior (AP) axis during cell cycles 4-6 in a process called axial expansion (Zalokar and Erk, 1976). Subsequently, in cell cycles 7-9 nuclei migrate progressively to the embryo surface (Baker et al., 1993) where they undergo 4 rounds of blastoderm divisions, which gradually slow down without losing synchrony.

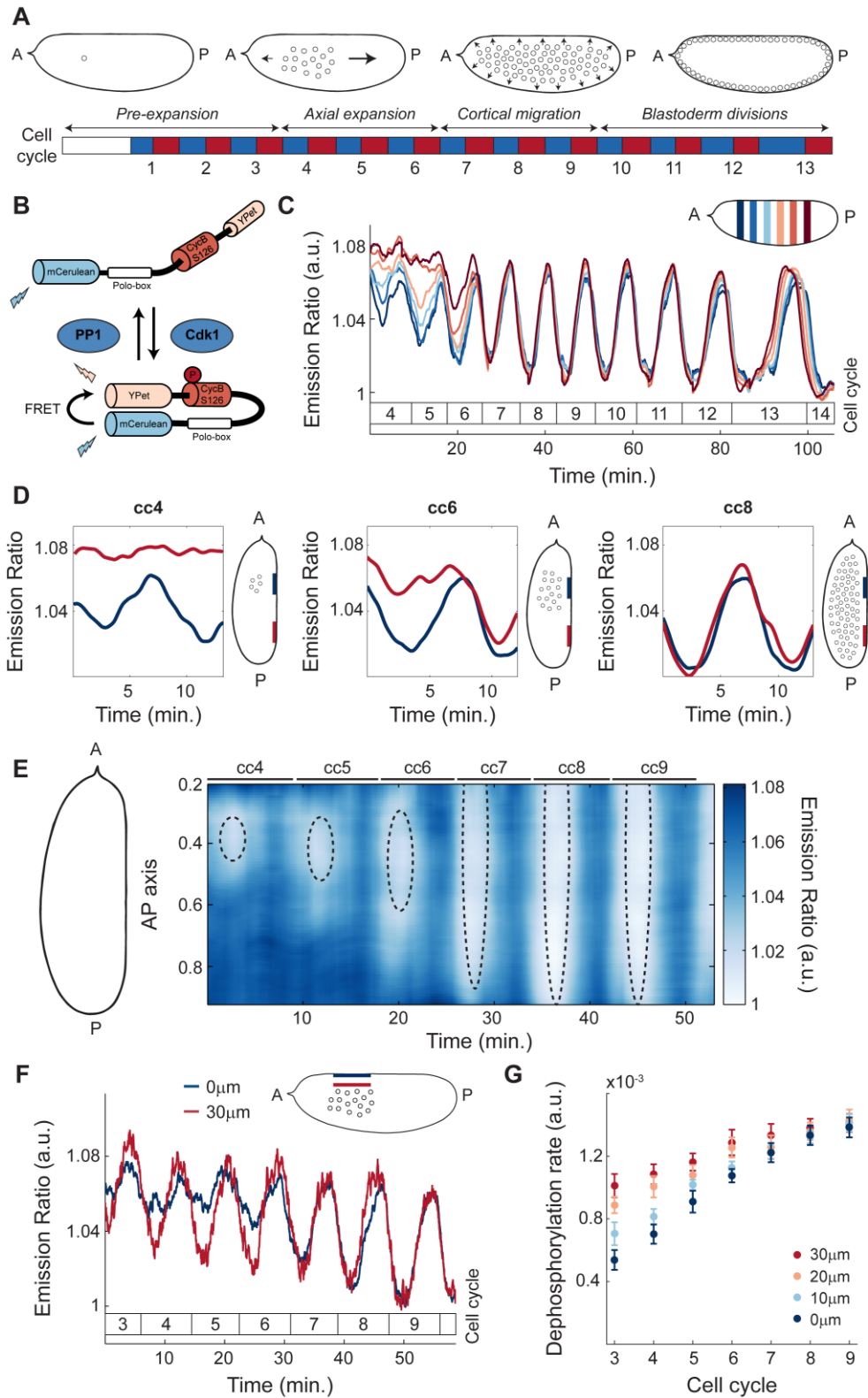


Figure 20: Nuclei provide a spatial landmark for the oscillations of Cdk1 and PP1. A) After fertilization, the *Drosophila* embryo undergoes 13 syncytial divisions characterized by four different stages of nuclear movement: pre-expansion (cc1-3), axial expansion (cc4-6), cortical migration (cc7-9), and blastoderm divisions (cc10-13). Embryo diagrams show mid-plane position of nuclear cloud during interphase of cell cycle 1, 6, 8 and 11, respectively. Blue boxes: S-phase; red boxes: mitosis. B) Diagram of Cdk1 to PP1 FRET sensor. C) Emission ratio of Cdk1/PP1 FRET sensor averaged in different regions of the surface of one embryo at cell cycles 4-14. Mitotic exit marks start of a new cycle. Inset, embryo outline with shaded boxes indicating the positions along the AP axis and at the surface of the embryo where the signal was averaged. D) Cdk1 to PP1 activity ratio in anterior (navy) or posterior (red) regions at the surface of an embryo for cell cycles 4 (left), 6 (middle), and 8 (right). Embryo diagrams show mid-plane position of the nuclear cloud as well as regions at the surface (navy and red) where measurements were taken. E) Heat map of Cdk1 to PP1 activity as a function of time along the AP axis of an embryo for cell cycles 4-9. Black dotted ellipses: nuclear cloud border. F) Emission ratio of Cdk1/PP1 FRET sensor for cell cycles 3-9 at embryo surface (blue) and 30 μ m from the surface (red); $p < 10^{-10}$ (χ^2 test). G) Quantification of the dephosphorylation rate of Cdk1/PP1 FRET sensor in different axial planes for cell cycles 3-9. Error bars, sem; a.u., arbitrary units.

Two conceptually distinct, although not mutually exclusive, models have been proposed for how nuclei spread across the AP axis (Royou et al., 2002; von Dassow and Schubiger, 1994), a process known to be driven by actomyosin contractility (Hatanaka and Okada, 1991; Zalokar and Erk, 1976). The first model, here referred to as the local disassembly model, proposes that actin around nuclei partially disassembles during interphase and this local decrease in tension causes streaming of the cytoplasm and the nuclei toward the poles (von Dassow and Schubiger, 1994). The second model, here referred to as the cortical contraction model, proposes that cycles of myosin II-driven cortical contraction generate cytoplasmic flows that push nuclei along the AP axis (Royou et al., 2002). These two models require different assumptions about the

mechanisms coupling cell cycle dynamics and nuclear movement, which have been shown to be tightly linked (Foe, 1993). In the first model, local cell cycle dynamics are sufficient to couple nuclear cycles and cytoskeletal rearrangements; conversely, the second model requires a mechanism that couples nuclear dynamics and cortical contractility over the relatively large distance (about 40 microns) separating nuclei from the cortex.

Our current understanding of the spatial regulation of the cell cycle is unable to distinguish between these two models. On the one hand, Cdk1 activity is high in most of the cytoplasm during the first 9 cell cycles (Edgar et al., 1994; Su et al., 1998), while it is locally inactivated through degradation of a small pool of cyclins around the nuclei (Huang and Raff, 1999). Consistent with the local disassembly model of nuclear spreading, local oscillations of Cdk1 can drive actin disassembly in a small region surrounding the nuclei (von Dassow and Schubiger, 1994). On the other hand, pharmacological perturbations of Cdk1 dynamics, which have been shown to interfere with cortical myosin II dynamics (Royou et al., 2002), argue in favor of the cortical contraction model. It remains unclear how cortical and cell cycle dynamics are coupled and whether this involves waves of Cdk1 activity, similar to those observed at the later blastoderm cycles (Deneke et al., 2016; Vergassola et al., 2018). Alternatively, the coupling could be mediated by the activity of mitotic phosphatases PP1 and PP2A. During mitosis, the activity of Cdk1 is high, while PP1 and PP2A activities are low (Grallert et al., 2015;

Heim et al., 2017). The decrease in Cdk1 activity at mitotic exit results in activation of mitotic phosphatases, which is further sharpened by several feedback mechanisms (Grallert et al., 2015; Mochida et al., 2010; Wu et al., 2009). How the activities of PP1 and PP2A are regulated spatially, and whether they play a role in nuclear positioning remains unknown.

Cytoplasmic flows represent a mechanism for large scale coordination of nuclear movements, provided their directionality and strength are regulated to ensure precise nuclear positioning. Nuclear spreading could potentially feedback on cell cycle synchrony since the distribution of nuclei across the embryo determines the nuclear to cytoplasmic ratio (NC ratio), which correlates with the duration of the nuclear divisions (Farrell and O'Farrell, 2014; Foe and Alberts, 1983; Sibon et al., 1997). During the later blastoderm cycles, an increase in the NC ratio reduces the DNA replication capacity of the embryo and triggers the activation of the DNA replication checkpoint, which causes a gradual slowdown of the cell cycle (Farrell and O'Farrell, 2014; Foe and Alberts, 1983; Sibon et al., 1997) and plays an important role in the regulation of mitotic synchrony (Deneke et al., 2016).

Here, we have generated imaging and computational tools to determine the mechanisms of nuclear positioning and cell cycle synchronization during early *Drosophila* development. We demonstrate that cell cycle synchronization emerges from the ability of

nuclei to self-organize their positioning by regulating the spatiotemporal dynamics of the cell cycle, cortical contractions, and cytoplasmic streaming. We show that local Cdk1 downregulation at mitotic exit initiates the damped spreading of PP1 activity, which is responsible for recruiting myosin II to cortical regions that surround the nuclei, where gradients of contractility are generated. These gradients drive cortical and cytoplasmic flows that properly position the nuclei across the embryo. Such spatial organization ensures a homogeneous NC ratio and synchronous embryo-wide oscillations of Cdk1 and PP1 activities at the maternal-to-zygotic transition.

3.3 Results

3.3.1 Nuclei provide a spatial landmark for the oscillations of Cdk1 and PP1

To elucidate the mechanisms that regulate the emergence of cell cycle synchronization in the *Drosophila* embryo, we first measured detailed spatiotemporal activity profiles of major cell cycle regulators. To this end, we used a biosensor which undergoes a conformational change increasing Fluorescence Resonance Energy Transfer (FRET) efficiency upon phosphorylation by Cdk1 (Figure 20B) (Deneke et al., 2016; Gavet and Pines, 2010b). In addition, we found that the dephosphorylation of the biosensor and the consequent decrease in FRET efficiency was triggered by PP1 activity (Experimental Methods; Figure 21A-B). Thus, at each time interval during the cell cycle, the biosensor (referred to as Cdk1/PP1 biosensor) reports the ratio of Cdk1 to PP1 activities. Quantification of the emission ratio of the Cdk1/PP1 biosensor near the

embryo surface shows that the Cdk1/PP1 ratio exhibited a disorganized pattern of activity in cell cycles 4-6 (Figure 20C). After cell cycle 6, oscillations became synchronous and persisted until cell cycle 14 (Figure 20C). Spatial analysis of the Cdk1/PP1 biosensor dynamics revealed that oscillations were restricted to regions of the cortex surrounding the nuclei (Figure 20D). To display Cdk1/PP1 activity in both space and time, we used a heat map representation where color indicates activity, the x-axis is the time coordinate and the y-axis the coordinate along the AP axis. We found that the oscillatory pattern of Cdk1/PP1 activity at the surface of the embryo gradually spreads along the AP axis during cell cycles 4-6 (Figure 20E). By cell cycle 7, the Cdk1/PP1 biosensor oscillated synchronously throughout the entire embryo (Figure 20E). Importantly, even though nuclei are located at the embryo mid-plane during the first 9 cycles, the region that displayed localized oscillations near the cortex is located 40 μm above the nuclei (Figure 20E, dotted ellipses and Figure 21C). The Cdk1/PP1 oscillations expanded in a manner that closely mirrors the expansion of the nuclear cloud (Figure 20E). Taken together our measurements argue that during the early cell cycles the oscillations in the Cdk1 to PP1 activity ratio at the surface of the embryo closely follow the position of the nuclei located at embryo mid-plane.

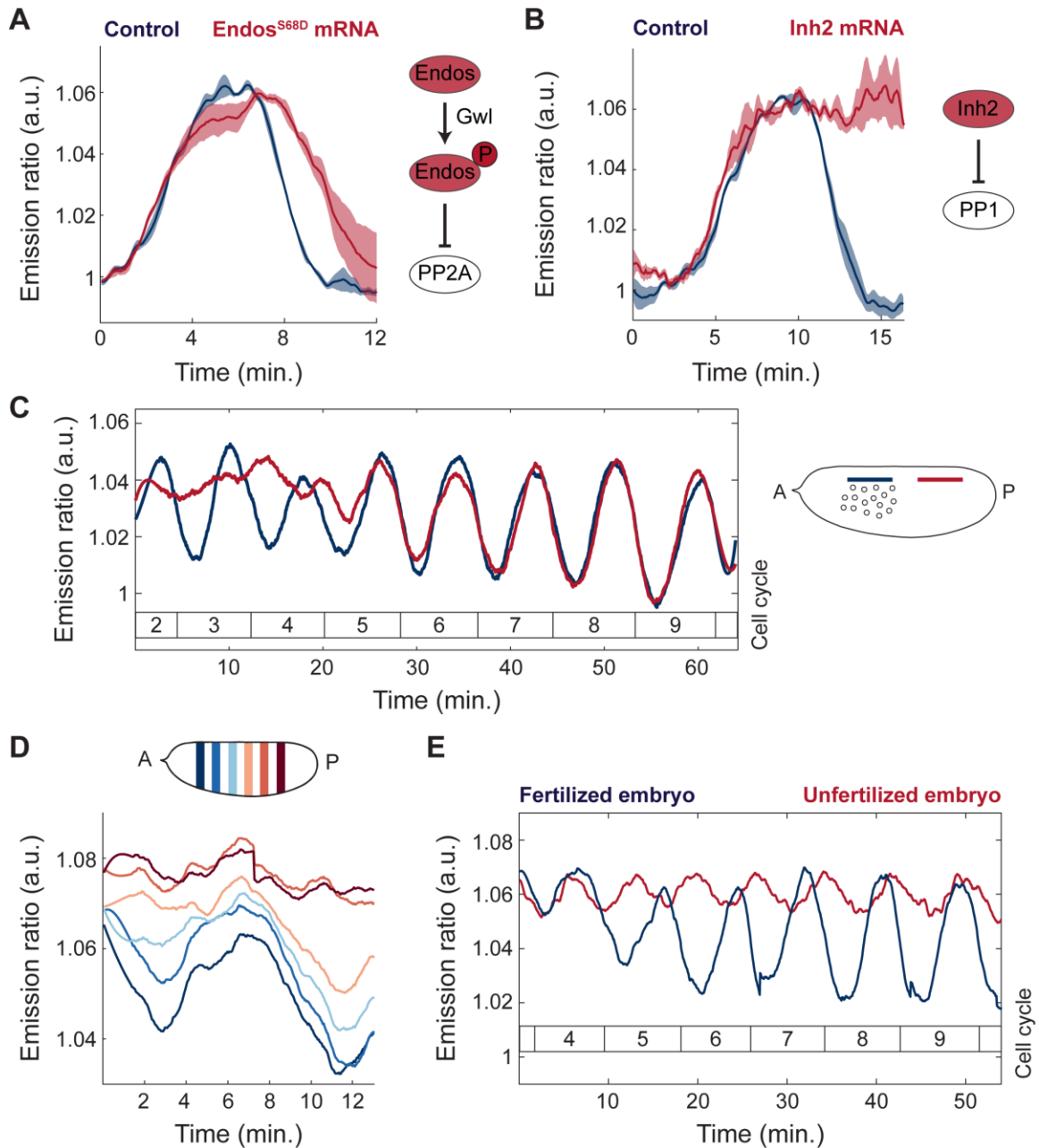


Figure 21: Identification of PP1 as the phosphatase driving dephosphorylation and spatiotemporal dynamics of the Cdk1/PP1 biosensor. A) Dynamics of biosensor in a control-injected blastoderm embryo (navy line) and embryo injected with phosphomimetic *endos-S68D* mRNA (red line), which inhibits PP2A. B) Dynamics of biosensor in a control-injected blastoderm embryo (navy line) and embryo injected with *I-2* mRNA (red line), which inhibits PP1. C) Emission ratio of Cdk1/PP1 FRET sensor averaged in regions 30 μ m from the surface on anterior side (blue line) and posterior side (red line).

Note that the early positioning of nuclei is on the anterior side. Inset, embryo outline with shaded boxes indicating position of plotted regions along the anterior-posterior axis and 30 μ m from the surface of the embryo. D) Cdk1 to PP1 activity ratio in anterior (navy line) or posterior (red line) regions at the surface of an embryo for cell cycle 4. Inset, embryo outline with shaded boxes indicating the positions along the anterior-posterior axis and at the surface of the embryo where the signal was averaged. E) Cdk1 to PP1 activity ratio in anterior region and at the surface of a fertilized (navy line) in cell cycles 4-9 and unfertilized (red line) embryo of similar age. Error bars, sem; a.u., arbitrary units.

To further elucidate the relation between the Cdk1 to PP1 oscillations at the cortex and around the nuclei, we performed measurements of the Cdk1/PP1 biosensor activity in the axial direction (Figure 20F). Biosensor oscillations in the cytoplasm close to the cortex were damped compared to oscillations in a region 30 μ m inside the embryo (Figure 20F), as well as along the AP axis (Figure 21D). To obtain further quantitative insights on the spatiotemporal dynamics of the Cdk1/PP1 biosensor, we measured the dephosphorylation rate, defined as the slope of the temporal decrease of the FRET signal at mitotic exit. Quantification of this rate in the axial direction showed a gradual decrease moving from the inner-most plane to the surface of the embryo (Figure 20G), confirming that the Cdk1/PP1 activity oscillations are the strongest around the nuclei and reduce as the surface of the embryo is approached. To further test the role of nuclei, we imaged activated, unfertilized eggs, which did not undergo nuclear proliferation. Importantly, newly laid unfertilized eggs did not show effective oscillations of the biosensor (Figure 21E), highlighting the importance of nuclei in initiating oscillations in the Cdk1/PP1 activity ratio. Collectively, our results demonstrate that local oscillations

of Cdk1 to PP1 initiate around the nuclei and spread radially in a damped manner.

These oscillations reach the surface of the embryo and could couple nuclear and cortical dynamics.

3.3.2 The dynamics of the cell cycle oscillator is characterized by a graded distribution of PP1 activity.

To confirm and elucidate the coupling between nuclear and cortical dynamics, we dissected the respective contribution of Cdk1 and PP1 to the oscillations of the biosensor. To determine whether oscillations at the surface of the embryo were due to downregulation of Cdk1 activity through cyclin degradation, we measured cyclin-B dynamics using 2-photon and confocal imaging of a functional GFP-cyclin-B trap line. Consistent with previous findings, cyclin-B levels only oscillated in a small region around the nuclei (Figure 22A, blue line; Figure 23A) (Huang and Raff, 1999). At the cortex, cyclin-B levels did not oscillate until the nuclei reached the surface of the embryo at cell cycle 9 (Figure 22A, red line). Spatial analysis of cyclin-B dynamics at the surface confirmed lack of local oscillations during early divisions (Figure 23B). Finally, we found that the dynamics of the Cdk1/PP1 biosensor was unaltered in embryos mutant for Wee1, a kinase playing a major role in the regulation of Cdk1 activity (Morgan, 2007) (Figure 23C). The upshot is that the local cytoplasmic oscillations of the Cdk1/PP1 biosensor are not due to cyclin degradation or post-translational regulation of Cdk1, thus pointing at the role of PP1 activity.

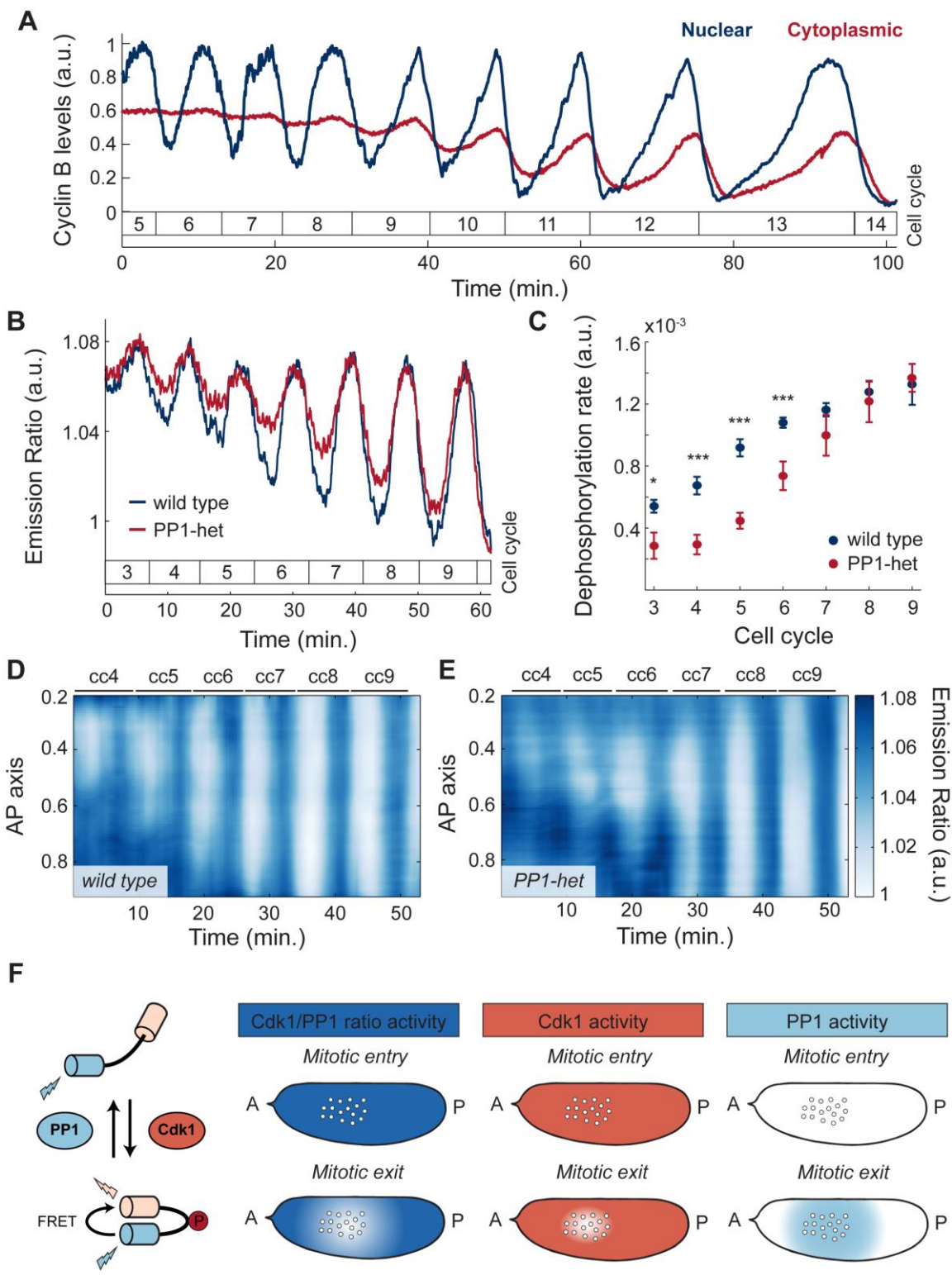


Figure 22: The dynamics of the cell cycle oscillator is characterized by a graded distribution of PP1 activity. A) Quantification of cyclin-B levels in the cytoplasm near the embryo cortex (red) and around nuclei (blue). B) Emission ratio of Cdk1/PP1 FRET sensor at the surface of a wild type (blue) or a PP1-het (red) embryo; $p < 10^{-10}$ (χ^2 test). C) Quantification of the dephosphorylation rate of Cdk1/PP1 FRET sensor in wild type (blue) vs. PP1-het embryos (red). $p < 10^{-10}$ (χ^2 test). D-E) Heat map of Cdk1 to PP1 activity along the AP axis of an embryo for cell cycles 4-9 near the cortex of a wild type (D) and a PP1-het (E) embryo. F) Diagram summarizing the activity of Cdk1 and PP1 in the early embryo. First panel from left: Simplified diagram of Cdk1 to PP1 FRET sensor. Second panel from left: Measured Cdk1 to PP1 activity ratio during mitotic entry and mitotic exit. Third panel from left: Cdk1 (coral shaded region) activity is downregulated only in a small region around nuclei during mitotic exit. Fourth panel from left: PP1 activity (light blue shaded region) shows a graded, damped distribution from nuclei to cortex during mitotic exit. Error bars, sem; a.u., arbitrary units. * $p < 0.05$, ** $p < 0.001$, *** $p < 0.0001$.

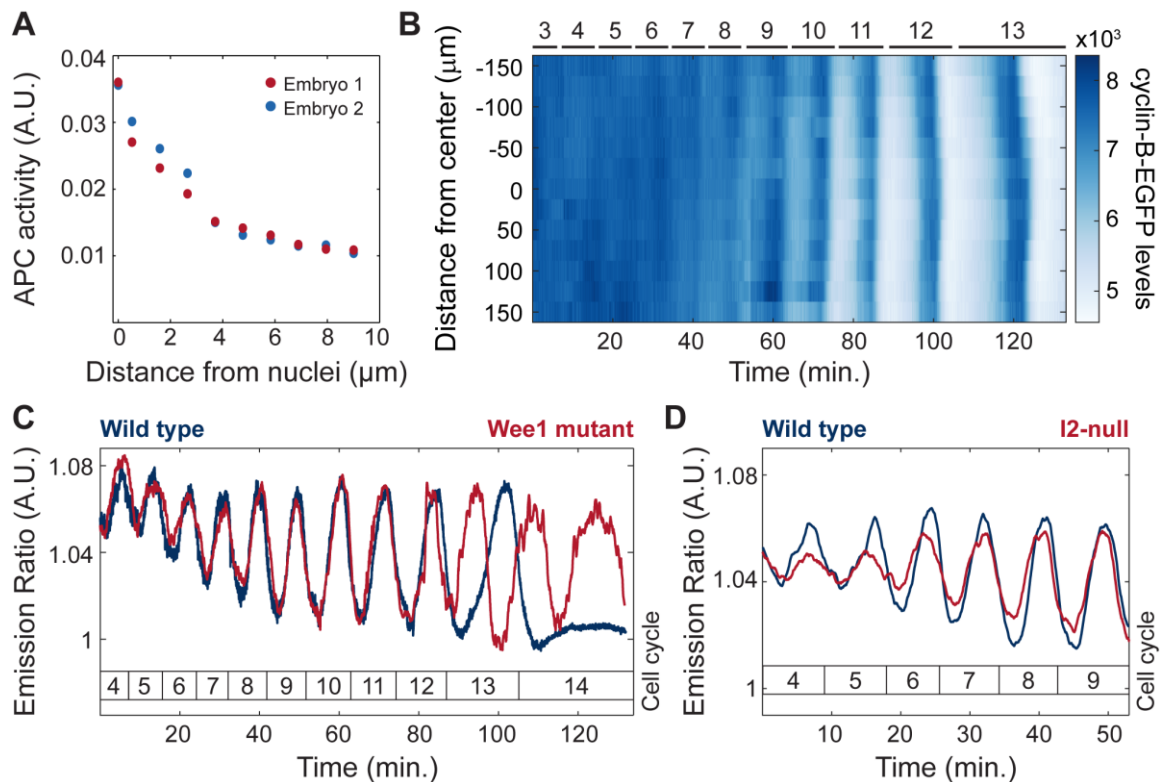


Figure 23: Biosensor dynamics near the surface of early embryos is regulated by PP1 activity rather than Cdk1. A) APC activity at mitotic exit as a function of distance from chromosomes in 2 embryos. APC activity was estimated as the relative rate of cyclin B

degradation, that is ***APC activity*** = $\frac{d[\text{CycB}]}{dt} / [\text{CycB}] = \frac{d}{dt} \ln[\text{CycB}]$. B) Heat map of cyclin B levels along the anterior-posterior axis at the surface of a wild type embryo for cell cycles 3-13. C) Emission ratio of Cdk1/PP1 FRET sensor at the surface of a wild type (blue line) or *wee1* mutant (red line) embryo. *wee1* mutant embryos fail to slow down the cell cycle during cc10-13 and as a result have 2 extra divisions. Nonetheless, the Cdk1/PP1 ratio shows very similar dynamics (the same amplitude and period) in both *wee1* mutants and wild type embryos during the pre-blastoderm cycles (cc 4-9). D) Emission ratio of Cdk1/PP1 FRET sensor at the surface of a wild type embryo (blue line) or an embryo in which I-2 levels are highly reduced by mutations (red line). $p < 10^{-10}$ (χ^2 test).

To test this hypothesis, we analyzed the dynamics of the biosensor in embryos heterozygous for two genes encoding maternally expressed PP1 α (hereby referred as PP1-heterozygous) (Kirchner et al., 2007). We observed that oscillations of the biosensor near the surface during the early cell cycles were damped in PP1-heterozygous embryos compared to wild type embryos (Figure 22B). This was due to reduced dephosphorylation rates (Figure 22C), indicating that PP1 is rate-limiting for dephosphorylation of the sensor. Spatial analysis of the Cdk1/PP1 biosensor showed delayed oscillations at the poles compared to wild type (Figure 22D-E). The importance of PP1 in the spatial regulation of the cell cycle was further supported by decreasing the levels of Inhibitor-2, a major regulator of PP1 activity (Figure 23D).

The above results collectively support the following model for the spatial regulation of the cell cycle. Upon mitotic entry, Cdk1 activity is uniformly high in the embryo, while PP1 activity is uniformly low (Figure 22F). At mitotic exit, cyclins are degraded in a small region surrounding the nuclei, which results in a local decrease of Cdk1 activity (Figure 22F) and PP1 activation. PP1 is then able to stimulate its own

activity, which extends to a spatial region of about 50 μm that reaches cortical regions surrounding the nuclear cloud (Figure 22F). Thus, our experiments argue that, similarly to the Cdk1/PP1 biosensor, other mitotic targets are dephosphorylated by PP1 in a region extending from the nuclei to the surrounding surface of the embryo (Figure 22F). Based on these data, we hypothesize that PP1 is responsible for coupling nuclear and cortical dynamics by driving the recruitment of myosin II to regions of the cortex surrounding the nuclear cloud.

3.3.3 Local PP1 activity couples nuclear and cortical dynamics by regulating cortical myosin II recruitment.

To demonstrate the role of PP1 activity in the recruitment and positioning of myosin II at the cortex, we measured both Cdk1/PP1 and Myosin II Light Chain dynamics (Video S1 in Deneke et al., 2019) simultaneously in early embryos. Spatial analysis of cortical myosin II dynamics showed that myosin II accumulated in regions where the Cdk1/PP1 biosensor featured oscillations (Figure 24A-D). In addition, myosin II recruitment closely followed the expansion of the Cdk1/PP1 oscillations along the AP axis (Figure 24A, C). Using a Moesin-ABD-GFP transgenic line, we visualized and quantified F-actin dynamics at the cortex, which closely matched myosin II dynamics both in space and time (Figure 25A-B). Cortical recruitment of F-actin and myosin II depend on Rho1 (Royou et al., 2002). Using a biosensor of Rho activity (Munjal et al., 2015), we found that Rho activity displayed spatial dynamics that closely matched that of myosin II (Figure 24E-F). Rho activity peaks simultaneously with PP1 activity, as

revealed by the low Cdk1/PP1 ratios at the maximum of Rho activity (Figure 24G, dotted line). The peak in Rho activity is followed by a peak in myosin II with a delay of 1-2 minutes (Figure 24G). This suggests that the delay between PP1 activation and myosin II accumulation is largely due to the time needed for myosin II activation by Rho. Both activation of Rho and recruitment of myosin II were reduced in PP1-heterozygous embryos (Figure 24H; Figure 25I), which further establishes the importance of PP1 in regulating actomyosin cortical contractility during the early cycles.

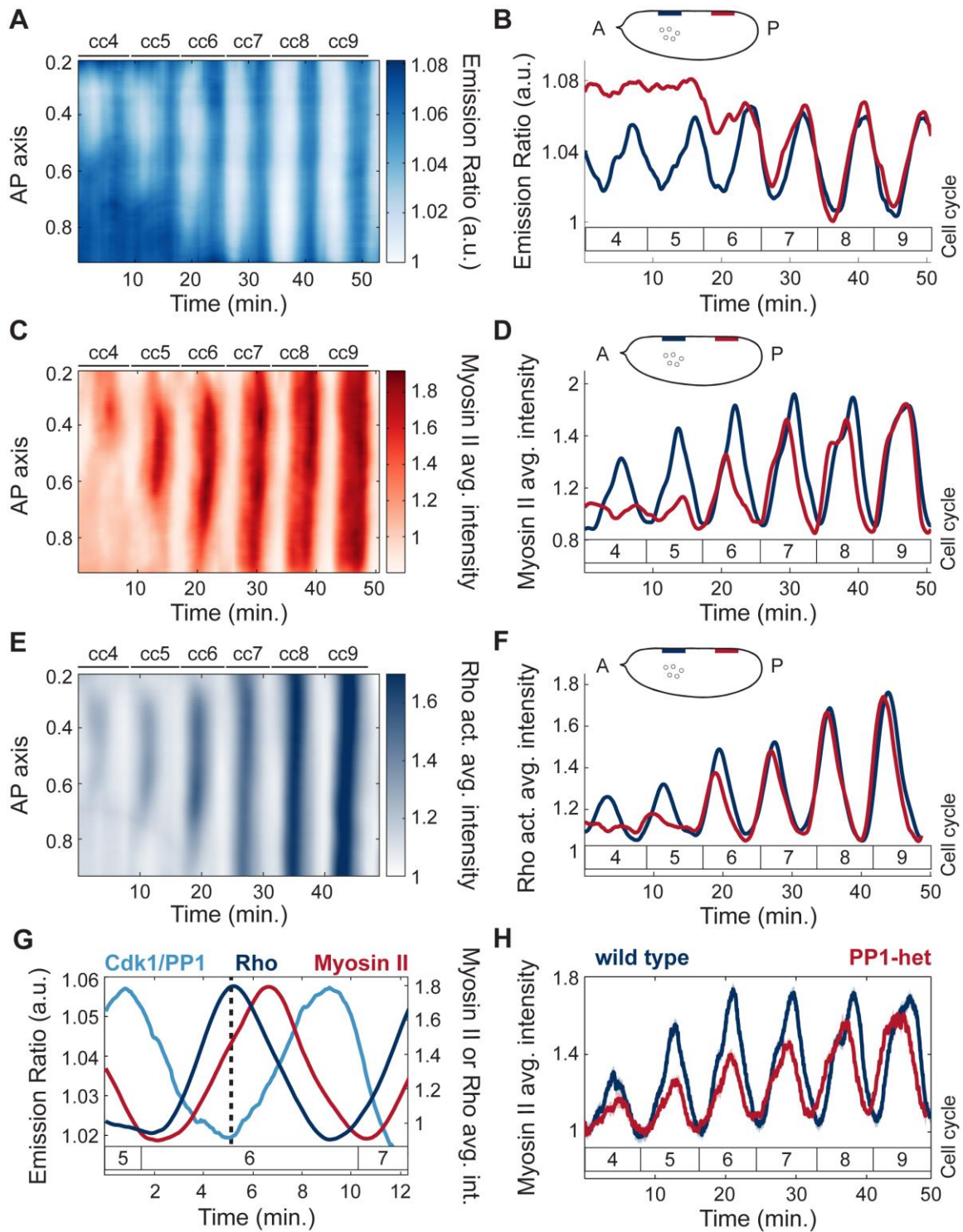


Figure 24: Local PP1 activity couples nuclear and cortical dynamics by regulating cortical myosin II recruitment. A) Heat map of Cdk1 to PP1 activity as a function of

time along the AP axis at the surface of a wild type embryo for cell cycles 4-9. B) Cdk1 to PP1 activity ratio in anterior (navy) or posterior (red) regions at the surface of an embryo for cell cycles 4-9. Inset, embryo outline with shaded boxes indicating the positions along the AP axis at the surface of the embryo where the signal was averaged (nuclear cloud at cell cycle 4 is depicted for reference). C) Heat map of myosin II levels as a function of time along the AP axis at the surface of a wild type embryo for cell cycles 4-9. D) Myosin II levels in anterior (navy) or posterior (red) regions at the surface of an embryo for cell cycles 4-9. Inset, same as in B. E) Heat map of Rho activity as a function of time along the AP axis at the surface of the embryo for cell cycles 4-9. F) Rho activity in anterior (navy) and posterior (red) regions at the surface of an embryo for cell cycles 4-9. G) Dynamics of Cdk1/PP1 FRET sensor, Rho activity, and myosin II levels averaged in regions surrounding nuclei at cell cycle 6. Dotted line: local Rho activity maximum and Cdk1/PP1 activity minimum. Delay between Rho activity and myosin level peak: 1.3 min. ($p < 10^{-6}$, t-test). H) Myosin II levels at surface averaged in regions surrounding nuclei for wild type (blue line) and PP1-het (red line) embryos at cell cycles 4-9. Shaded regions, sem; $p < 10^{-10}$ (χ^2 test); a.u., arbitrary units.

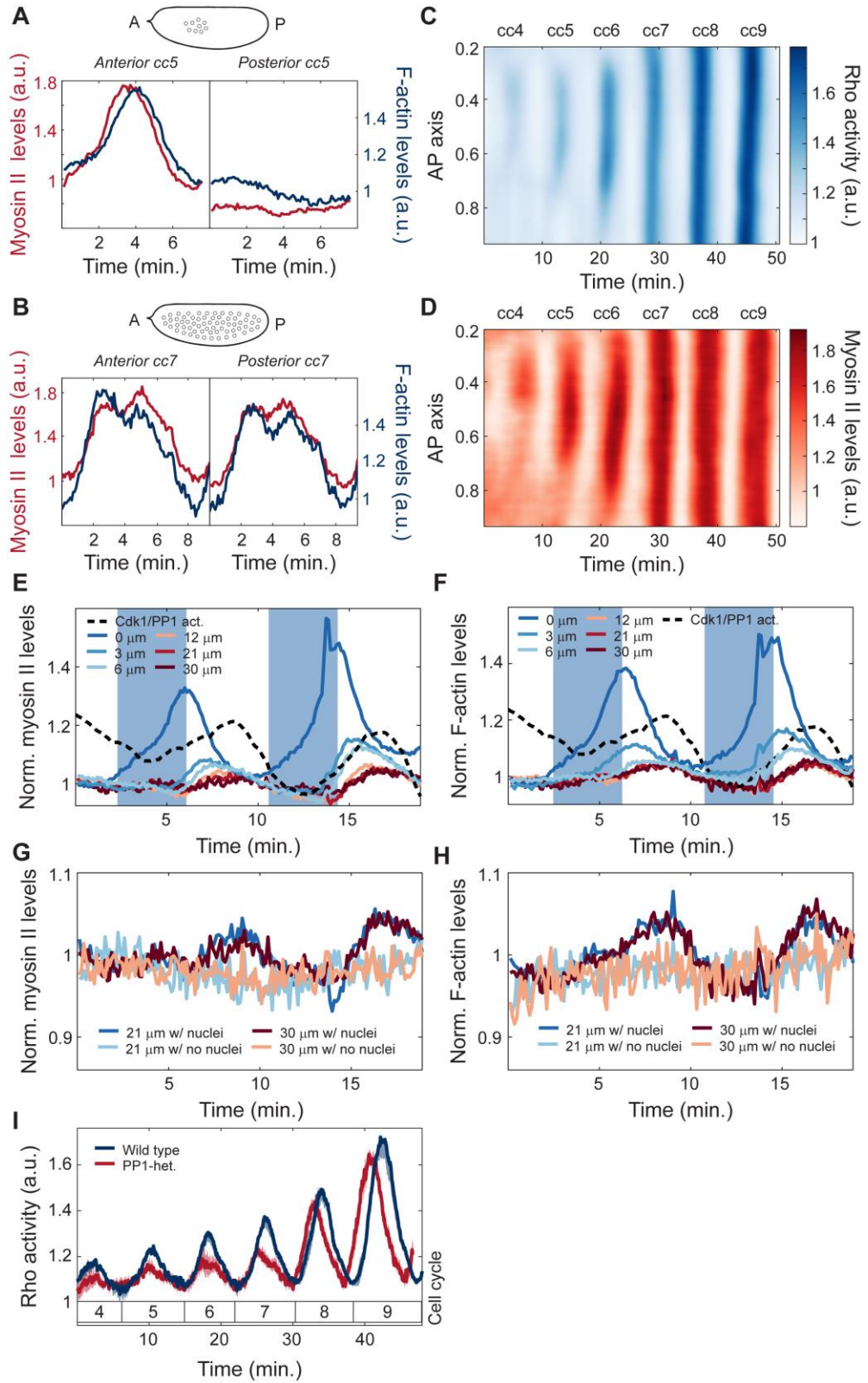


Figure 25: Quantification of myosin II, F-actin and Rho activities in early development. A) Myosin II and F-actin (measured by Moesin-ABD-GFP) levels as a function of time in anterior (left) or posterior (right) regions at the surface of an embryo for cell cycle 5. B) Myosin II and F-actin level dynamics in anterior (left) or posterior (right) regions at the surface of an embryo for cell cycle 7. C-D) Heat map of Rho activity (C) and myosin II levels (D) along the anterior-posterior axis at the surface of a wild type embryo for cell cycles 4-9. E-F) Myosin II (E) and F-actin (F) level dynamics for cell cycles 5-6 at embryo surface (blue line) and varying distances from the surface (see legend). Dotted black line: Cdk1 to PP1 activity dynamics. G-H) Myosin II (G) and F-actin (H) level dynamics averaged in regions with and without nuclei and at different depths from the surface (see legend). I) Rho activity at the surface averaged across oscillating regions for wild type (blue line) and PP1-heterozygous (red line) embryos. Shaded regions, sem.; $p < 10^{-10}$ (χ^2 test).

3.3.4 Myosin II gradients drive cortical contractions

One possible function of coupling cell cycle dynamics and cortical actomyosin accumulation is the generation of cycles of cortical contractility and flow during interphase, which could in turn control cytoplasmic flow and nuclear positioning. Spatial analysis of myosin II recruitment revealed that myosin II accumulated locally and formed gradients along the AP axis during cycles 4-6 (Figure 26A, top panel). The region of myosin II accumulation gradually expanded until cycle 7, while at the following cycles myosin II accumulated uniformly across the AP axis (Figure 26A, bottom panel). The transition to a uniform myosin II accumulation coincided with the time when nuclei occupied the entire AP axis in the interior of the embryo and Cdk1/PP1 oscillations became uniform. To dissect the relationship between myosin II dynamics and cortical flows, we performed particle image velocimetry (PIV) in embryos co-expressing His2Av-GFP and MLC-mCherry (see Experimental Methods) (Video S2 in

Deneke et al., 2019). The His2Av-GFP signal was sufficiently particulate to be tracked by PIV and could be used to measure the flow of the cytosol, that is the soluble aqueous component of the cytoplasm, as confirmed by FRAP (Fluorescence Recovery After Photobleaching) measurements of soluble GFP (see Figure 27A-C and Experimental Methods). Trajectories of the flow field during cell cycle 6 showed a polarized movement of the cytoplasm from the poles towards a point of zero velocity (stagnation point) at around 40% egg length (Figure 26B, light to dark red trajectories, inset). In contrast, once nuclei distributed across the AP axis by cell cycle 7, no net flow was evident (Figure 26C, light to dark red trajectories, inset). Quantification of the velocities during cortical contractions along the AP axis allowed the generation of a spatiotemporal cortical flow map, where flows to the posterior side are represented as positive velocities (Figure 26D, blue shades) and flows towards the anterior side as negative velocities (Figure 26D, red shades). Geometry and strength of the cortical flows demonstrated a tight correlation with myosin II gradients. First, cell cycles 4-6, which exhibited gradients of myosin II (Figure 26A, top panel), also displayed cycles of polarized contraction (Figure 26D, cell cycles 4-6). Second, the speed of cortical flow increased as myosin II accumulation levels increased and expanded (Figure 26D, cc4-6; Figure 26G, left panel, solid lines). Third, during cycles 7-9, when myosin II accumulated uniformly at the cortex, embryos did not undergo polarized contractions and showed little to no net flow (Figure 26D, cc7-9; Figure 26G, right panel, solid lines). To test

quantitatively whether cortical flows could be predicted by myosin II gradients, we measured myosin II gradients during the contraction phases of cycles 5-7 (Figure 27D-F) and compared the cortical speed along the AP axis to predictions of a viscoelastic model (Mayer et al., 2010). In the model, cortical tension results from the combination of tension imbalances between neighboring regions, which are linked to myosin II gradients, and viscous effects, which characterize the physical nature of cortical flows (see Experimental Methods). We found that speed and direction of cortical flows were in good agreement with theoretical predictions (Figure 26E). These data strongly suggest that myosin II gradients at the embryo cortex drive cortical contractions and cortical flows during cell cycles 4-6. Furthermore, assuming that the cytoplasm behaves as an incompressible fluid, inward flows at the cortex must generate outward flows in the mid-embryo. In this manner, cytoplasmic flows could achieve the proper geometry and magnitude to facilitate nuclear spreading.

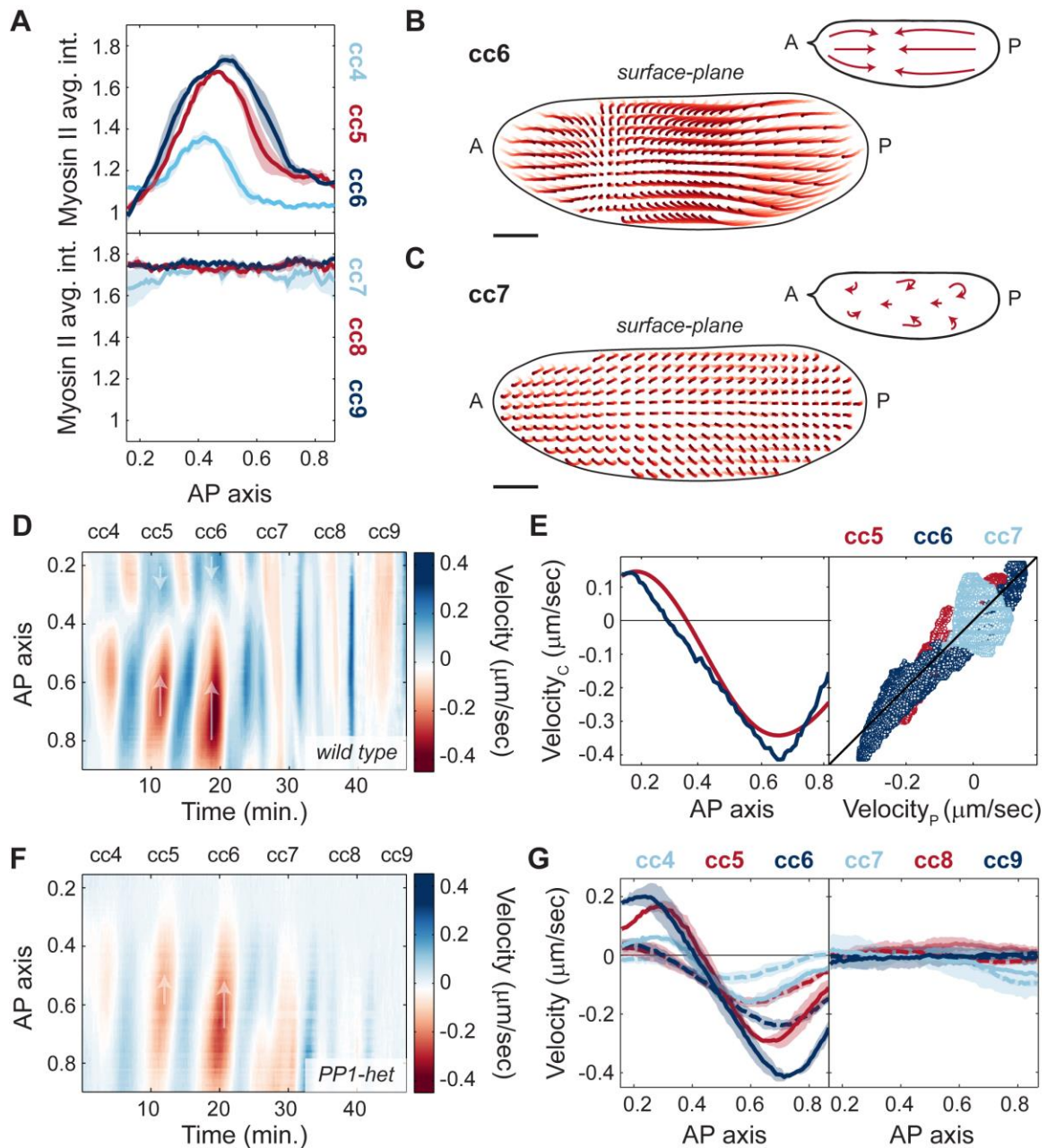


Figure 26: Myosin II gradients drive cortical contractions. A) Myosin II intensity profiles across AP axis during maximum myosin II recruitment for cell cycles 4-6 (top) and cell cycles 7-9 (bottom). B-C) Cortical flow trajectories (light to dark red) for contraction phase of an embryo during cell cycle 6 (B) and cell cycle 7 (C). Insets, schematic of streamlines showing direction of cortical flows. D) Heat map of cortical flow velocity along the AP axis of an embryo for cell cycles 4-9. Arrows indicate the direction of movement along the AP axis. E) Left: Measured cortical velocity (blue line)

for a cycle 6 embryo and predicted velocity (red line) from myosin II gradients. Right: Cortical velocity versus predicted velocity using a gradient-driven flow model for cell cycle 5 (red), 6 (navy blue) and 7 (light blue). Black line: least squares regression line ($R^2=0.82$). F) Heat map of cortical flow velocity along the AP axis of a PP1-het embryo for cell cycles 4-9. Arrows as in D). G) Velocity profiles across AP axis during contraction phases of cell cycles 4-6 (left panel) and cell cycles 7-9 (right panel) for wild type (solid lines) and PP1-het embryos (dashed lines). For cell cycles 4-6, $p < 10^{-10}$ (χ^2 test); for cell cycles 7-9, not significant. Shaded regions, sem. Scale bars, $50\mu\text{m}$.

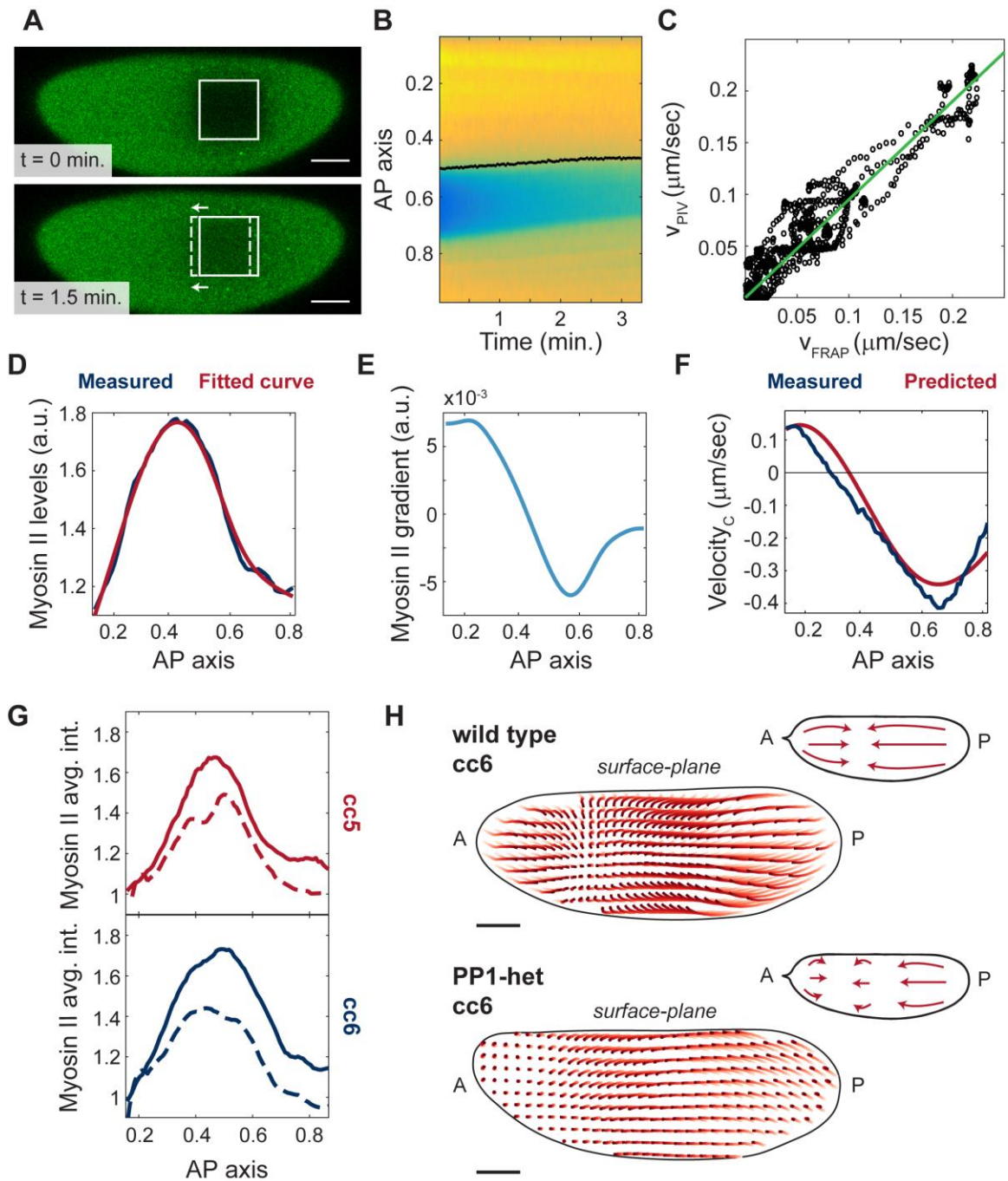


Figure 27: Prediction of cortical velocity from myosin II gradients and quantification of gradients and cortical flows in PP1-heterozygous embryos. A) Snapshots of an embryo expressing soluble Cdc25^{Twine}-GFP 0 min. (top) and 1.5 min. (bottom) after fluorescence recovery of bleached region. White box: bleached region at $t=0$ min. Dotted white box: bleached region at $t=1.5$ min. B) Heat map of GFP fluorescence intensity along

the AP axis following photobleaching. Dotted black line: calculated position of front edge of bleached area. C) Velocity measured by PIV of His2Av-mRFP images versus velocity measured by FRAP for 10 embryos during cell cycles 4-8. Solid green line: best fit line (slope: 0.96 ± 0.02). D) Measured myosin II intensity profile across AP axis for one embryo in cell cycle 6 (blue line) and fitted curve (red line). E) Myosin II gradient across AP axis. F) Measured cortical velocity (blue line) for a cycle 6 embryo and predicted velocity (red line) from myosin II gradients. G) Myosin II intensity profiles across AP axis during maximum myosin II recruitment for cell cycle 5 (top) and cell cycle 6 (bottom) in wild type (solid lines) vs. PP1-heterozygous (dotted lines) embryos. H) Cortical flow trajectories (light to dark red) for contraction phase of a wild type (top) and PP1-heterozygous (bottom) embryo during cell cycle 6. Insets, schematic of streamlines showing direction of cortical flows. Scale bars, $50\mu\text{m}$.

To evaluate the role of localized PP1 oscillations in the regulation of cortical contractions, we measured myosin II gradients and cortical flows in PP1-heterozygous embryos. Myosin II spatial profiles retained a similar geometry in PP1-heterozygous embryos to that observed in wild type embryos, but with reduced amplitude (Figure 27G). Consistently, flows at the cortex were reduced by about 2-fold in PP1-heterozygous embryos during cycles 4-6 (Figure 26F-G, cc4-6, dotted lines). Thus, cortical contractions damped when PP1 levels decreased, yet the geometry of the flow remained unaltered (Figure 26F-G; Figure 27H). Therefore, PP1 activity plays a crucial role in coupling cell cycle and cortical dynamics by regulating myosin II gradients at the cortex and, consequently, the magnitude and geometry of cortical contractions.

3.3.5 Nuclear movements correlate with cytoplasmic flows

To test the role of cytoplasmic flows in nuclear positioning, we measured and reconstructed mid-embryo flows using a technique to stain yolk granules (Quinlan,

2016) and PIV analysis (Video S3-4 in Deneke et al., 2019), which provided a reliable measurement of cytosolic flow as confirmed by FRAP measurements of soluble cytosolic RFP (Figure 28A-C). Nuclei were tracked using a PCNA-TagRFP transgenic line, whose high expression levels enabled deep tissue imaging of nuclei during interphase by confocal microscopy. In interphase of cycle 6, embryos displayed cytoplasmic flows characterized by features compatible with nuclear spreading. In the middle of the embryo where nuclei are located, the cytoplasm flowed from the center of the nuclear cloud toward the poles (Figure 29A, light to dark red trajectories, inset). Nuclei closely followed the direction of the cytoplasmic flows and spread to the same extent (Figure 29A, light to dark blue trajectories). Consistent with data shown in Figure 26 flows were also visible near the cortex of the embryo, moving from the poles toward the center and meeting at a position along the AP axis closely matching the center of the nuclear cloud. The bidirectional flow both at the cortex and mid-embryo created four vortices and a stagnation point that arose near the center of the nuclear cloud where cortical flows converged and ingressed (Figure 29A, inset) (von Dassow and Schubiger, 1994). In cycle 7, once nuclei were uniformly spread along the AP axis, cytoplasmic flows were significantly reduced (Figure 29B, light to dark red trajectories) and nuclei also showed little movement (Figure 29B, light to dark blue trajectories). Quantitative analysis of cytoplasmic and nuclear speed during cycles 4-8 showed a high degree of correlation (Figure 29C). Additionally, the direction of the nuclear and cytoplasmic movements

throughout the embryo was strongly correlated (Figure 29D), thus demonstrating that nuclear movements closely followed the flow of the cytoplasm.

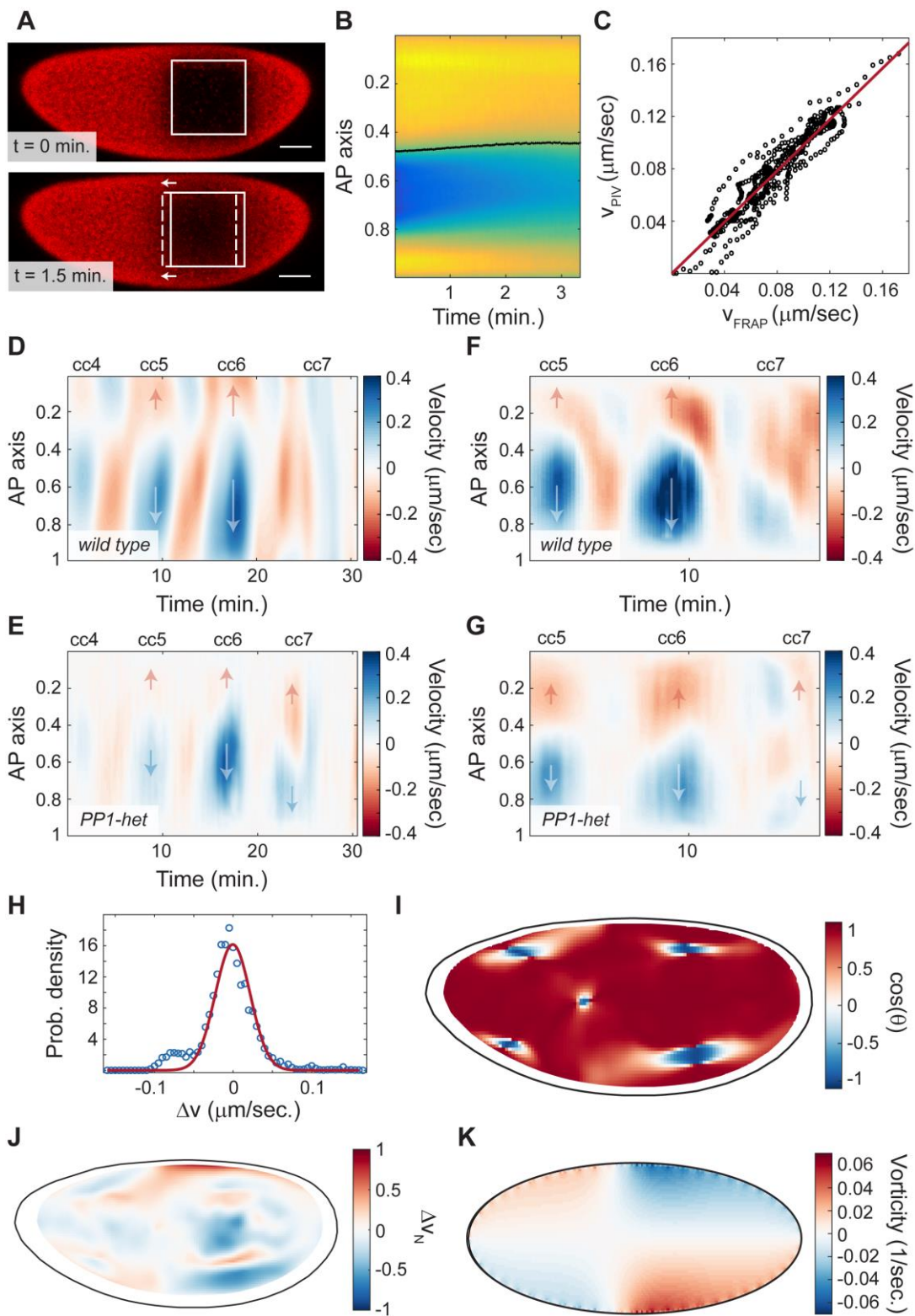


Figure 28: Cytoplasmic flows in wild type and PP1-heterozygous embryos. A) Snapshots of an embryo expressing soluble PCNA-TagRFP 0 min. (top) and 1.5 min. (bottom) after fluorescence recovery of bleached region. White box: bleached region at $t=0$ min. Dotted white box: bleached region at $t=1.5$ min. B) Heat map of TagRFP fluorescence intensity along the AP axis following photobleaching. Dotted black line: calculated position of front edge of bleached area. C) Velocity measured by PIV on yolk granules versus velocity measured by FRAP on PCNA-TagRFP for 10 embryos during cell cycles 4-8. Solid red line: best fit line (slope: 0.98 ± 0.02). D-E) Heat map of cytoplasmic flow in a $50 \mu\text{m}$ region in the center of a wild type (D) and a PP1-heterozygous embryo (E) for cell cycles 4-7. Arrows indicate the direction of movement along the AP axis. F-G) Heat map of cytoplasmic flow in a $50 \mu\text{m}$ region in the center of a wild type (F) and a PP1-heterozygous embryo (G) for cell cycles 5-7. Arrows indicate the direction of movement along the AP axis. H) Probability density of the difference between the speed predicted by Stokes' flow and the measured speed. As a reference, the experimental resolution is $1 \text{ pixel} / 2 \text{ frames} \sim 0.025 \mu\text{m/s}$. Red line: Gaussian fit. I) Heat map showing the cosine of the angle Θ defined by the measured velocity and the velocity predicted by Stokes' flow. J) Heat map showing the difference between the speed predicted by Stokes' flow and the measured speed normalized by the root-mean-square in a posterior region in the mid-embryo where flows are strong. K) Vorticity ($\omega = \nabla \times \mathbf{v}$) for a simulated Stokes' flow, demonstrating that maxima and minima are located at the embryo cortex.

Similar to cortical flows, cytoplasmic speed increased gradually in magnitude from cycles 4-6 but was significantly reduced by cycle 7 (Figure 29E, blue line). Since embryos heterozygous for PP1 showed reduced cortical contractions, we hypothesized that cytoplasmic flows should also be reduced. In agreement with our prediction, PP1-heterozygous embryos showed damped cytoplasmic flows during cycles 4-6 (Figure 29E, red line, Video S5 in Deneke et al., 2019). Spatial analysis of mid-embryo movements showed that flows in PP1-het embryos followed the same polarized geometry as those in wild type embryos during cycles 4-6 (Figure 29F-G; Figure 28D-G). However, at cycle 7, when wild type embryos no longer show polarized flows, PP1-het

embryos still showed polarized cytoplasmic flows (Figure 29G, cell cycle 7; Figure 28D-G), consistent with the fact that nuclei were not uniformly distributed at cycle 7 in mutant embryos.

To assess the ability of the measured flows to position nuclei uniformly, we quantified the extent to which cytoplasmic flows could drive separation of initially proximal particles. We asked whether nuclei distributed uniformly at the end of cycle 7 would start from a small cloud at the beginning of cycle 4 according to the measured flow. To this aim, we computationally positioned uniformly-distributed particles in the mid-embryo along the AP axis at the end of cycle 7. We then used the measured cytoplasmic flows to evolve their position back in time until the beginning of cycle 4. Wild type flow trajectories were able to transform a cloud of nuclei similar to the one observed at cycle 4 into a uniform distribution by the end of cycle 7 (Figure 29H, bottom panel). By contrast, in PP1-heterozygous embryos flows were unable to disperse the nuclei properly and the only possibility to obtain a uniform nuclear distribution by cycle 7 was to start with partially dispersed nuclei (Figure 29I, red lines). Altogether, this quantitative analysis argues that flows in wild type embryos are effective at nuclear spreading, while flows in PP1-heterozygous are not sufficient to spread nuclei uniformly, as it is indeed observed in experimental data (Figure 29I, top panel).

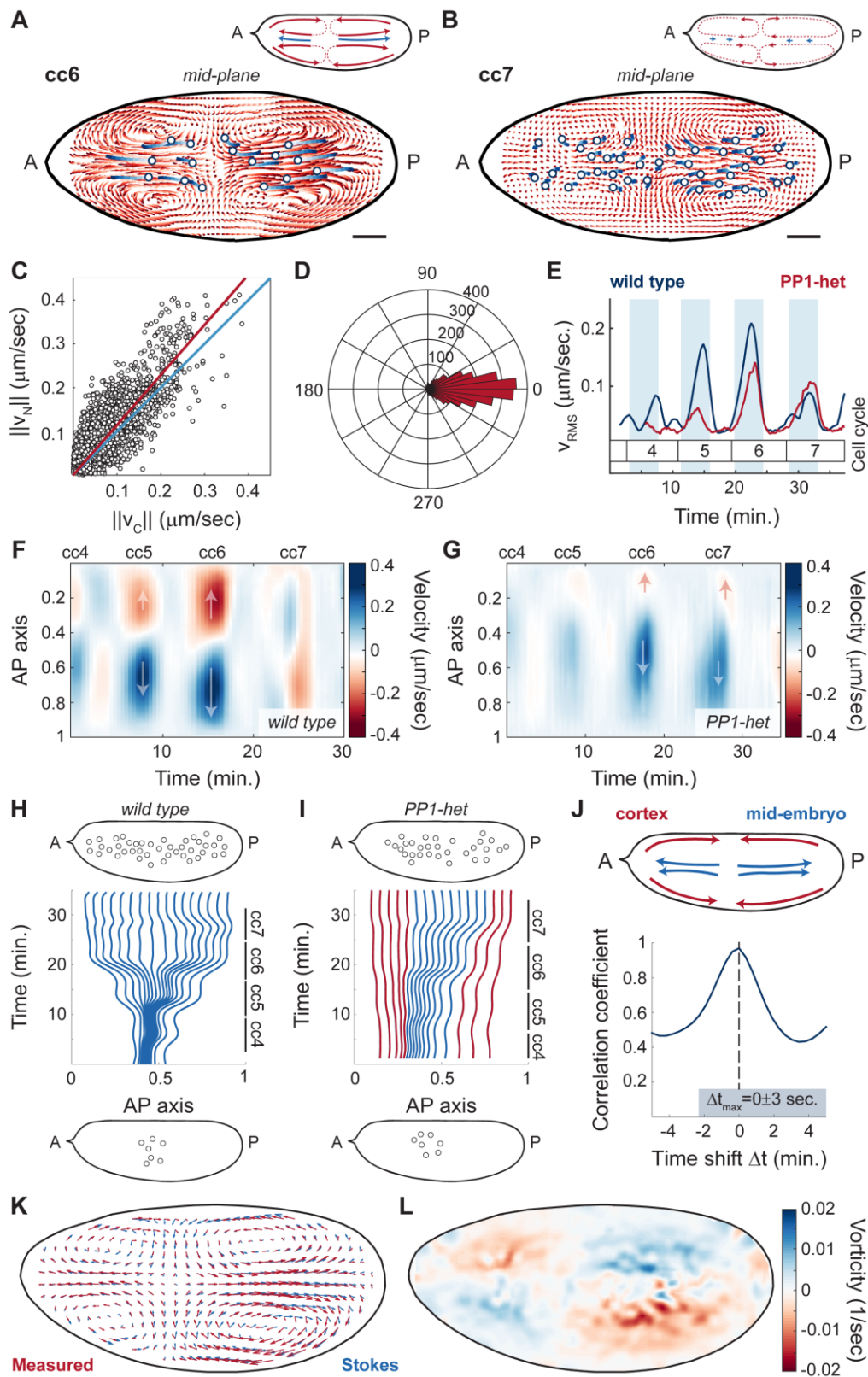


Figure 29: Nuclear movements correlate with cytoplasmic flows. A-B) Cytoplasmic flow trajectories (light to dark red) and nuclear trajectories (light to dark blue) during interphase of cell cycle 6 (A) and cell cycle 7 (B). Insets, schematic of streamlines showing direction of cortical and cytoplasmic flows (red) and nuclear movement (blue). Scale bars, 50 μ m. C) Modulus of nuclear versus cytoplasmic flow velocities for embryos in cell cycles 4-7. Blue line: identity line; red line: best fit. D) Histogram in polar coordinates of the angle between nuclear and cytoplasm velocities. E) Root mean square velocity across a wild type embryo (blue) and a PP1-het (red) embryo in cell cycles 4-7. Shaded blue regions: interphase. $p < 10^{-10}$ (χ^2 test). F-G) Heat map of cytoplasmic flow in a 50 μ m region in the center of a wild type (F) and a PP1-het embryo (G) for cell cycles 4-7. Arrows indicate the direction of movement along the AP axis. H-I) Computationally reconstructed flow trajectories needed for uniform nuclear distribution at the end of cell cycle 7 in a wild type (H) and a PP1-het embryo (I). Blue lines represent trajectories that at cell cycle 4 initiate in the region where nuclei are present, while red lines represent trajectories outside of the nuclear cloud. Top and bottom insets: nuclear distribution in embryos at cell cycle 4 (bottom) and cell cycle 7 (top) from experimental data. J) Cross-correlation analysis of cortical flows and mid-embryo cytoplasmic flows. K) Comparison between the measured flow (red arrows) and the best-fitted Stokes' flow (blue arrows). L) Heat map showing the vorticity field ($\omega = \nabla \times v$) of the measured flow.

3.3.6 Optogenetic control of Rho signaling shows that cytoplasmic flows and nuclear movements are mainly driven by cortical contractions.

Cytoplasmic flows are synchronized with the cell cycle and occur predominantly during interphase (Figure 29E). However, the respective contributions to the generation of flows by actomyosin contractility in the bulk cytoplasm or at the cortex remain to be determined, as both contractile modes are regulated by the cell cycle. To distinguish between these two possibilities, first we performed a correlation analysis between the dynamics of cortical and mid-embryo cytoplasmic flows in the same embryo, and found that they are essentially simultaneous (Figure 29J), arguing that flows of cytoplasm near the cortex and in the mid-embryo might be directly coupled. Second, we assayed the

contribution of the contractile cortical actomyosin to the motion of the cytoplasm by an experimental approach that allows specific control over cortical contractility. To this end, we made use of an optogenetic tool to activate Rho signaling specifically at the embryo cortex (Izquierdo et al., 2018). Upon blue light activation, the catalytic domain of RhoGEF2, tagged with the photosensitive protein domain CRY2, was recruited to the plasma membrane of the illuminated area, via a CIB1 localized plasma membrane anchor (Figure 30A, Figure 31A-D), where it triggered Rho signaling and myosin II activation (Izquierdo et al., 2018)(Figure 31E-G). Embryos expressing RhoGEF2::CRY2 were imaged in the presence of uniform blue light, which resulted in uniform recruitment of myosin II at the cortex (Figure 31F-G), which overrode endogenous cortical myosin II gradients that were present during the contraction cycles (Figure 26B). Embryos exposed to uniform blue light showed dramatic dampening both of cortical contractions (Figure 30B) and of mid-embryo cytoplasmic flows (Figure 30C-D, Video S6 in Deneke et al., 2019). Importantly, in embryos exposed to uniform blue light, nuclei failed to spread along the AP axis during interphase (Figure 30E). Therefore, actomyosin gradients at the cortex are necessary to generate cortical contractions which then facilitate cytoplasmic flows and nuclear spreading.

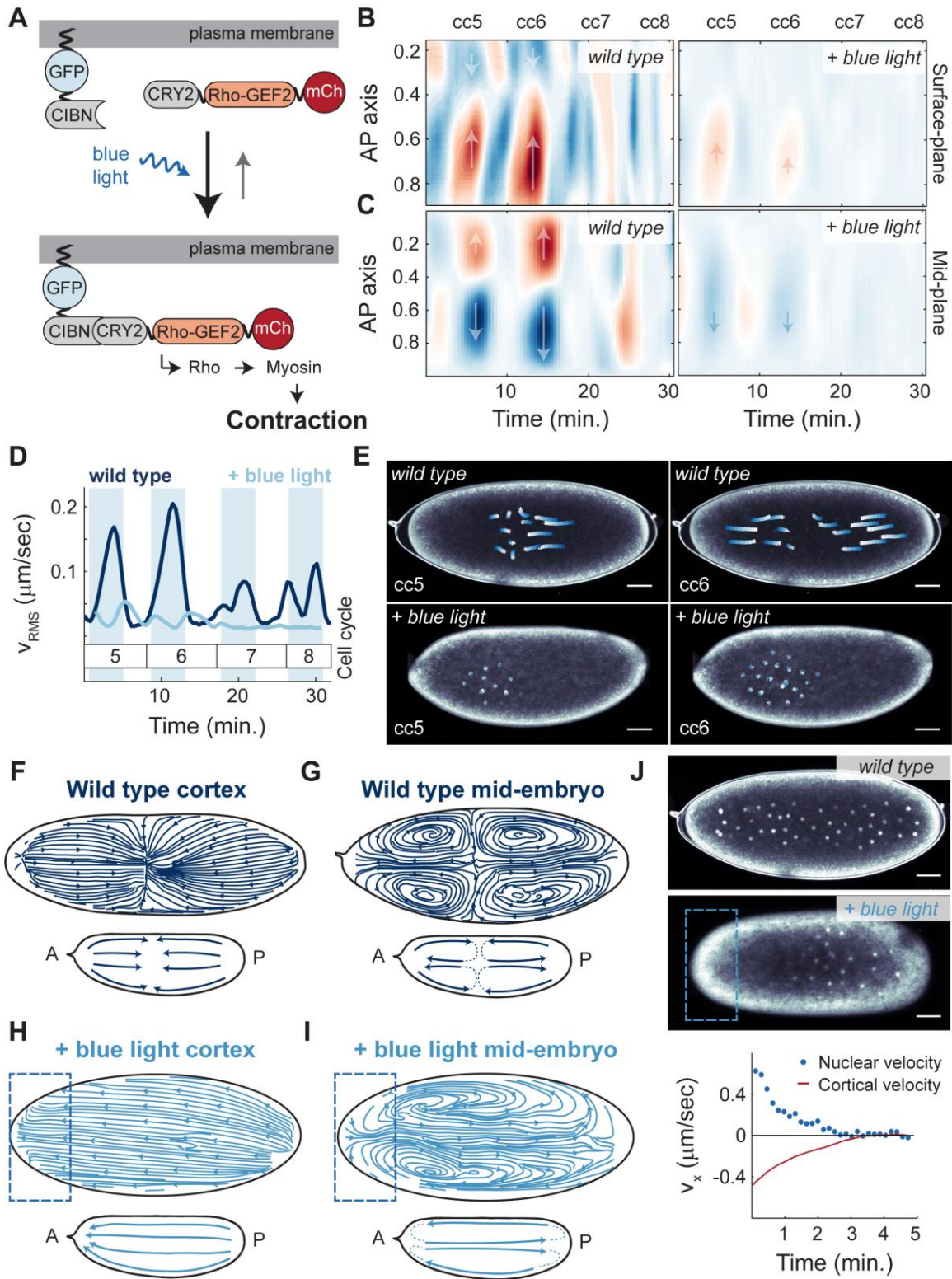


Figure 30: Optogenetic control of Rho signaling shows that cytoplasmic flows and nuclear movements are mainly driven by cortical contractions. A) Schematic view of the RhoGEF2 optogenetic tool. B) Heat map of cortical velocities in a wild type (top) and embryo expressing RhoGEF2 optogenetic system exposed to constant blue light (bottom) for cell cycles 5-8. Arrows indicate the direction of movement along the AP axis. C) Heat map of mid-embryo cytoplasmic velocities in a wild type (top) and embryo expressing RhoGEF2 optogenetic system exposed to constant blue light (bottom) for cell cycles 5-8. Arrows as in B). D) Root mean square cytoplasmic velocity of a wild type embryo (navy blue) and an optogenetic RhoGEF2 embryo exposed to blue light (light blue). Shaded blue regions: interphase. E) Nuclear trajectories (white to blue) for contraction phase of a wild type (top) or optogenetic RhoGEF2 embryo exposed to blue light (bottom) during cell cycle 5 (left) and cell cycle 6 (right). F-G) Streamlines showing direction of cortical (F) or cytoplasmic (G) flows in a wild type embryo during cell cycle 6. Inset, summary diagram of flows. H-I) Streamlines showing direction of cortical (H) or cytoplasmic (I) flows in an optogenetic RhoGEF2 embryo that was activated with blue light on the anterior pole. Inset, summary diagram of flows. J) Top two panels: Nuclear distribution for a wild type (top) and a pole-activated embryo (middle) at cell cycle 7 expressing PCNA-TagRFP to mark nuclei. Bottom panel: average cortical velocity during one contraction phase (red line) with corresponding nuclear velocity (blue points) of an optogenetic RhoGEF2 embryo activated on anterior pole. Scale bars, 50 μ m.

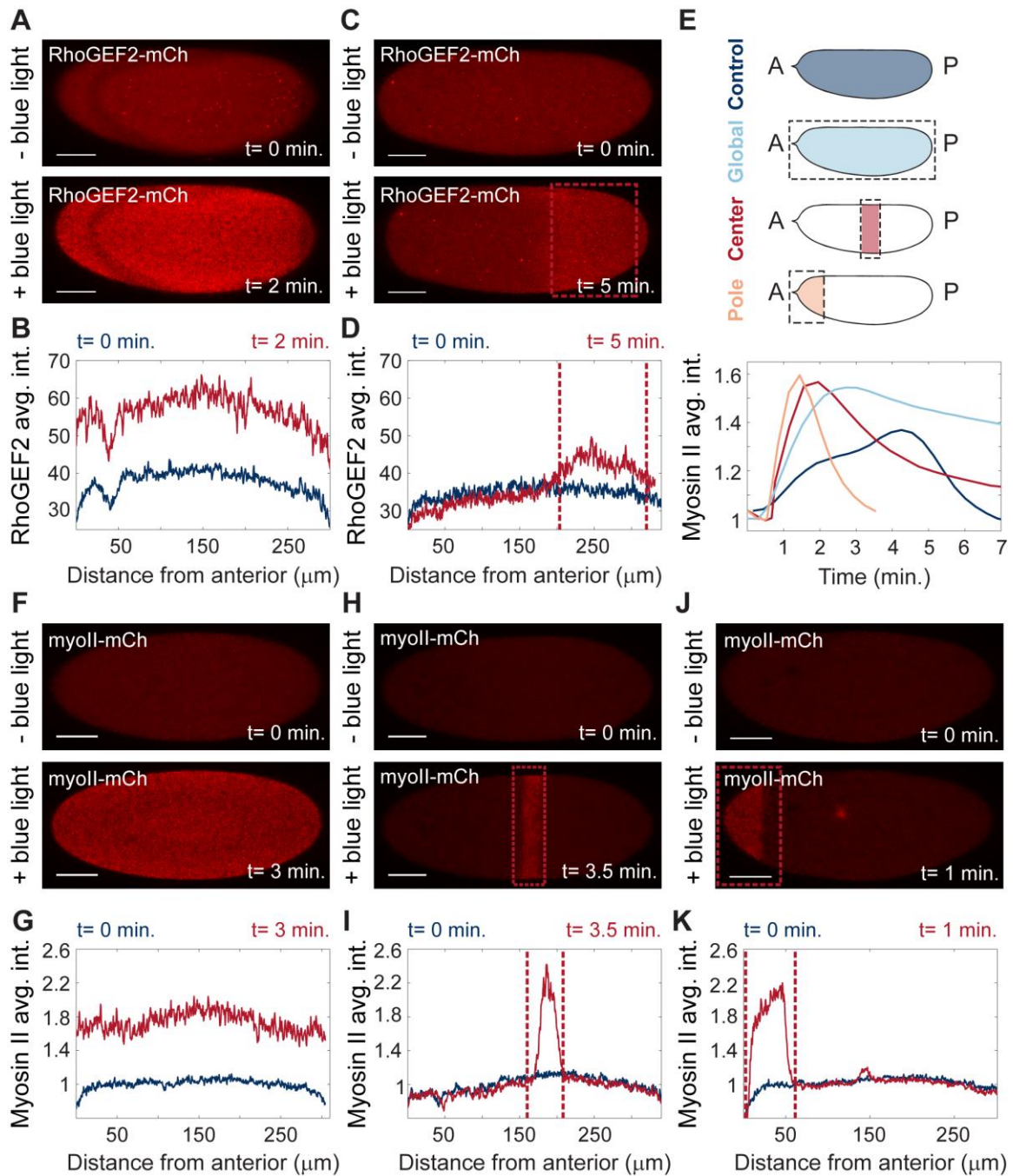


Figure 31: Optogenetic RhoGEF2-CRY2 recruitment to plasma membrane drives myosin II cortical accumulation upon blue light illumination. A) Snapshot of an embryo co-expressing CIBN::pmGFP and RhoGEF2-CRY2::mCherry before (top) and after global blue light illumination (bottom). B) Quantification of RhoGEF2 average intensity across the embryo before (navy line) and after (red line) global blue light

illumination. C) Snapshot of an embryo co-expressing CIBN::pmGFP and RhoGEF2-CRY2::mCherry before (top) and after local blue light illumination on posterior side of embryo (bottom). Dotted box: illuminated region. D) Quantification of RhoGEF2 average intensity across the embryo before (navy line) and after (red line) global blue light illumination. Dotted lines: illuminated region. E) Quantification of myosin II average intensity dynamics of embryos co-expressing CIBN::pmGFP, RhoGEF-CRY2, and myosin II::mCherry. Navy line, no blue light illumination control embryo showing endogenous myosin II recruitment at cell cycle 7. Light blue line, embryo illuminated with blue light globally. Red line, embryo illuminated only in local center region. Light peach line, embryo illuminated on posterior side. Top panel, diagrams of all illumination conditions with illuminated regions shown in dotted black line and averaged region shown in colored regions. F) Snapshot of an embryo co-expressing CIBN::pmGFP, RhoGEF2-CRY2, and myosin II::mCherry before (top) and after global blue light illumination (bottom). G) Quantification of average myosin II intensity across an embryo before (navy line) and after (red line) global blue light illumination. H) Snapshot of an embryo co-expressing CIBN::pmGFP, RhoGEF2-CRY2, and myosin II::mCherry before (top) and after center blue light illumination (bottom). Dotted box: illuminated region. I) Quantification of average myosin II intensity across an embryo before (navy line) and after (red line) center blue light illumination. Dotted lines: illuminated region. J) Snapshot of an embryo co-expressing CIBN::pmGFP, RhoGEF2-CRY2, and myosin II::mCherry before (top) and after local blue light illumination in anterior side of embryo (bottom). Dotted box: illuminated region. K) Quantification of average myosin II intensity across an embryo before (navy line) and after (red line) local blue light illumination on anterior side of embryo. Dotted lines: illuminated region. All scalebars, 50 μ m.

To test whether cortical myosin II gradients were also sufficient to control nuclear spreading, we locally recruited RhoGEF2::CRY2 to different cortical regions of the embryo along the AP axis and assessed whether flows and nuclear movements could be induced in a predictable manner. Specifically, we reasoned that, if RhoGEF2::CRY2 was recruited to one pole, cortical flows would be directed toward that pole, while mid-embryo cytoplasmic flows and nuclear movements would be directed toward the opposite pole. In wild type embryos, flows at the cortex at cycle 6 were directed towards

a point along the AP axis that corresponded to the center of the nuclear cloud (Figure 30F). In the middle of the embryo, flows were directed out from the center of the nuclear cloud and towards the poles (Figure 30G). Upon light-mediated recruitment of RhoGEF2 to the anterior pole of the embryo, myosin II was recruited to the activated area (Figure 31J-K), and cortical flows were now re-directed towards the anterior pole (Figure 30H). As expected, mid-embryo flows displayed unidirectional flows toward the posterior side of the embryo (Figure 30I) and nuclei were consequently shuttled to the posterior side of the embryo (Figure 30J, top 2 panels, Video S7 in Deneke et al., 2019). By simultaneously measuring cortical flow velocities and nuclear movement velocities in anteriorly-activated embryos, we observed that, as the cortex moves toward the anterior pole (negative velocity), nuclei move at a similar rate towards the posterior pole (positive velocity) (Figure 30J, red line vs. blue points, respectively). Taken together, these results demonstrate that the positioning of myosin II at the cortex and the consequent gradients that are formed upon activation of contractility determine the geometry of the cortical and cytoplasmic flows, which in turn control the movement and distribution of nuclei in the embryo.

3.3.7 Viscous dynamics captures the large-scale features of cytoplasmic flows

The cytoplasm is a complex medium that features at least two phases, an active actomyosin gel and a fluid cytosol (Mogilner and Manhart, 2018). The permeation of the fluid through the gel is important in a number of biological phenomena, which have

motivated the development of multi-phase models, for example poroelastic, that are poised to capture the relative motion and conditions for equilibration between the two phases (Charras et al., 2005; Mitchison et al., 2008). Our experiments suggest a simpler physical model for *Drosophila* cytoplasmic flows. Indeed, while relative motion between the actomyosin gel and the cytosol is possible and expected at small scales, our data show that the motion of the two phases in *Drosophila* embryos is strongly correlated on timescales of tens of seconds (Figures 26 and 29; Figure 27A-C and Figure 28A-C). Furthermore, the general circulation patterns of the flow in Figure 30G are on spatial scales comparable to the embryo size, which are larger than the expected microscopic length scales. These observations argue that the large-scale dynamics of the bulk flow is consistent with the phases being equilibrated, and that the dynamics may then lend to an approximate description by a single, effectively continuum phase. In principle, such phase should be modeled as a viscoelastic fluid (Mogilner and Manhart, 2018). Yet, our optogenetic experiments argue that contractility effects in the bulk, which are responsible for elastic behaviors, are small (Figure 30B-D). We conclude that the simplest physical model that recapitulates our experimental observations has an active actomyosin gel generating cortical contractions at the boundary of the embryo, which, in turn, drive a large-scale flow in the bulk that can be described by a single effective fluid that is passive and incompressible.

The flow of such fluid is characterized by its Reynolds number, which for our observed flows is small ($Re = \frac{VL}{\nu} \approx 10^{-5}$, where $V \approx 0.3\mu\text{m}/\text{s}$ is the observed typical velocity of the flow, $L \approx 100\mu\text{m}$ is a characteristic length related to the size of the embryo and $\nu \approx 3 \cdot 10^6\mu\text{m}^2/\text{s}$ is an estimate of the kinematic viscosity (Swaminathan et al., 1997)). A low Reynolds number implies that viscous forces dominate over inertial forces. The resulting viscous dynamics is consistent with the experimentally observed absence of delays between the motion at the cortex and in the bulk (Acheson, 1990). Since the major active mechanisms act near the embryo boundary, mathematically we account for the effects of cortical contractions by boundary conditions. In other words, the flow in the bulk is obtained by solving the fluid dynamics (Stokes) equations for a passive viscous fluid and the effects of cortical activity are introduced by setting the velocity at the boundary. Flows predicted by this procedure are similar to cytoplasmic flows measured experimentally (Figure 29K). Specifically, both direction and speed of the observed and the best-fitted Stokes flow are comparable (Figures 28H-J).

While the above description is appropriate at large scales, deviations are expected at small scales, which we could detect. For instance, the vorticity field features maxima and minima inside the embryos (Figure 29L), which is not possible for a Stokes flow since its extrema can be proved to be restricted at the boundary of the embryo (see Experimental Methods and Figure 28K). Vorticity is the mathematical quantity that

locally measures the rotation of fluid elements with respect to their center of mass, and it involves derivatives of the velocity that highlight characteristic structures at small scales. The observed deviations are likely due to a combination of active mechanisms in the bulk, for instance of the type identified previously for the cytoplasmic actomyosin network (Field et al., 2011; von Dassow and Schubiger, 1994) (Figure 25E-F), and multi-phase effects that are not captured by our simplified model. In summary, our analysis suggests that, at the relatively large scales relevant for nuclear positioning, the flow in the bulk is mainly controlled by viscous effects. As a consequence, despite the complex actomyosin dynamics, the large-scale features of the flow are well captured by the dynamics of a viscous, incompressible fluid passively responding to active contractions at the cortex.

3.3.8 Proper nuclear positioning is required for synchronous cell cycles

Our results point towards a self-organized process by which nuclei drive their positioning in the early *Drosophila* embryo. Nuclei initiate the oscillations of PP1 that drive the recruitment of myosin II at the cortex, which then generates cortical gradients (Figure 32A, left panel). These gradients lead to stereotypical cortical contractions which in turn give rise to mid-embryo cytoplasmic flows that spread nuclei along the AP axis and control to their positioning across the embryo (Figure 32A, middle and right panel). Nuclear positioning locally determines the NC ratio, which regulates multiple aspects of embryonic development, including the cell cycle remodeling events that accompany the

maternal-to-zygotic transition (Farrell and O'Farrell, 2014; Ferree et al., 2016).

Specifically, the NC ratio is a major determinant of the duration of DNA replication and, as a consequence, cell cycle timing. Thus, we predicted that altering nuclear spreading may give rise to differential activation of the DNA replication checkpoint across the embryo. As a consequence, cell cycle timing would be spatially perturbed, resulting in loss of mitotic synchrony as embryos approached the maternal-to-zygotic transition.

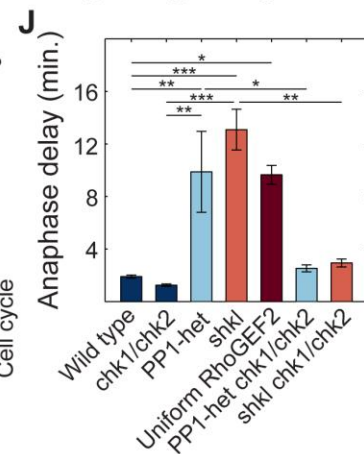
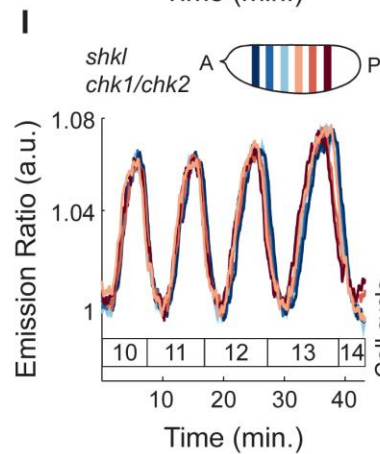
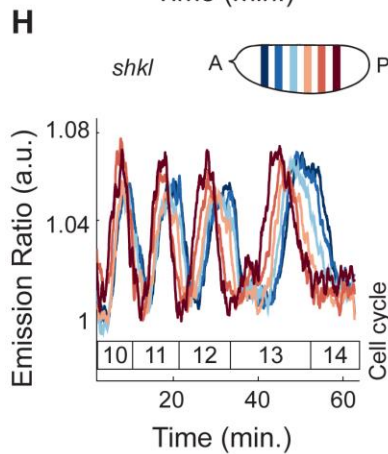
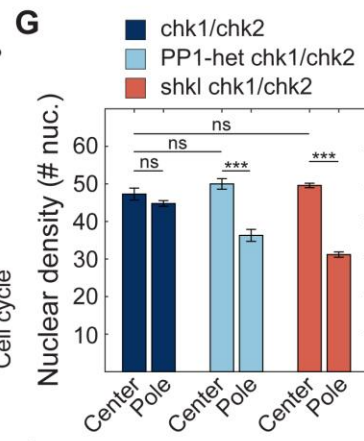
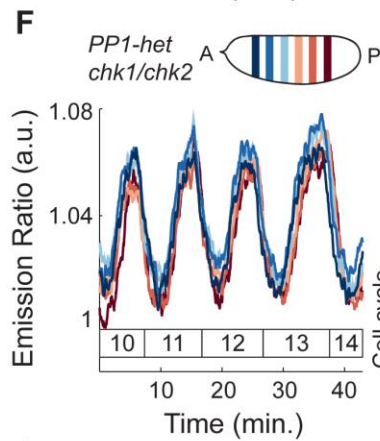
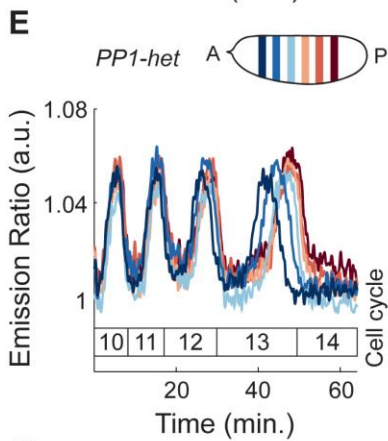
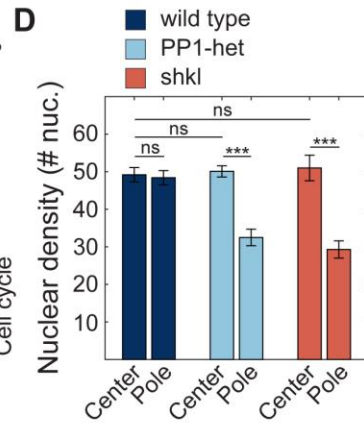
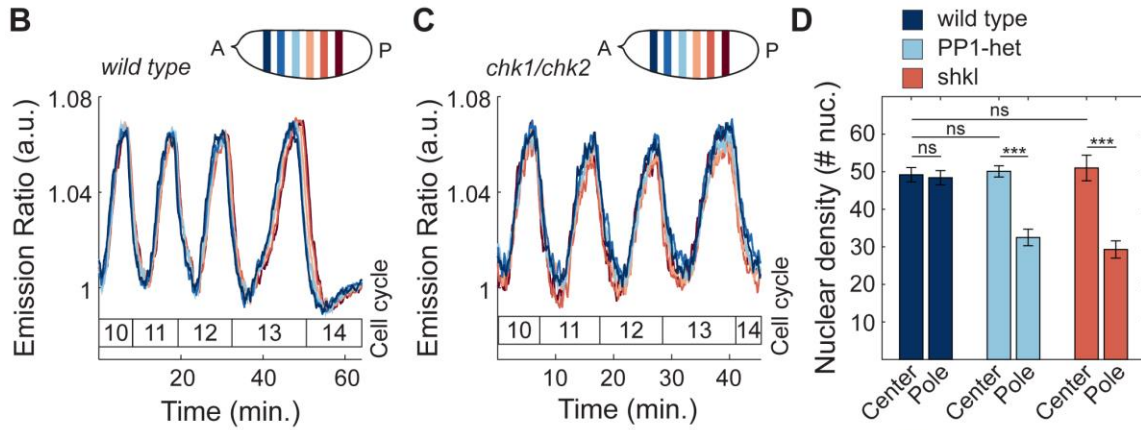
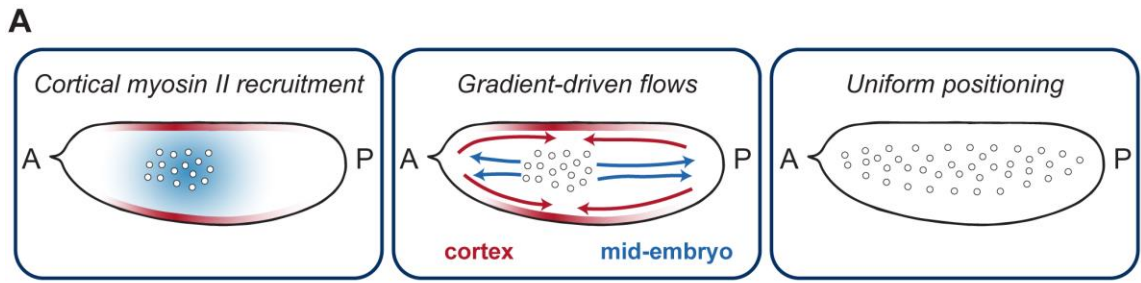


Figure 32: Proper nuclear positioning is required for synchronous cell cycles. A) Model of nuclear spreading in early *Drosophila* embryos. Left embryo: local oscillations of PP1 activity (blue faded region) spread in a damped manner from the nuclear cloud and position myosin II at the cortex (red faded outline). Middle embryo: gradients of myosin II drive cortical contractions (red arrows) which result in mid-embryo cytoplasmic flows (blue arrows). Right embryo: Cytoplasmic flows push nuclei toward poles and distribute them along the AP axis. B-C) Emission ratio of Cdk1/PP1 FRET sensor averaged in different regions of the surface of a wild type (B) and *chk1/chk2* (C) embryo at cell cycles 10-13. D) Nuclear density in a 50 μ m by 50 μ m region in center or pole region of a wild type, PP1-het and *shkl* embryo in cell cycle 13. E-F) Emission ratio of Cdk1/PP1 FRET sensor averaged in different regions of the surface of a PP1-het (E) and PP1-het *chk1/chk2* (F) embryo at cell cycles 10-13. G) Nuclear density in a 50 μ m by 50 μ m region in center or pole region of a *chk1/chk2*, PP1-het *chk1/chk2* and *shkl chk1/chk2* embryo in cell cycle 13. H-I) Emission ratio of FRET sensor averaged in different regions of the surface of a *shkl* (H) and *shkl chk1/chk2* (I) embryo at cell cycles 10-13. J) Quantification of delay between first nucleus to enter anaphase to last nucleus in cell cycle 13. Error bars, sem. * $p < 0.05$, ** $p < 0.001$, *** $p < 0.0001$; a.u., arbitrary units.

In wild type embryos, at cycle 13, the last syncytial cycle, the dynamics of the Cdk1/PP1 biosensor across different regions of the embryos were synchronous (Figure 32B). This synchrony was observed starting from the end of cycle 6/beginning of cycle 7, when nuclei underwent the last axial spreading movement (Figure 20C). In fact, wild type embryos showed uniform nuclear density in the center and pole regions (Figure 32D, navy bars). In a fraction of PP1-heterozygous embryos (7 out of 11), reduced cortical and cytoplasmic flows disrupted nuclear spreading (Figure 32D, light blue bars). This subset of embryos showed significant asynchronies in the blastoderm cell cycles that became very prominent in cycle 13 (Figure 32E). Therefore, by halving the dose of PP1, embryos featured damped, and spatially more confined, oscillations in the Cdk1 to PP1 activity ratio (Figure 22E), reduced cortical contractions (Figure 26F-G) and

cytoplasmic flows (Figure 29E, G), non-uniform positioning and tissue-wide asynchronies (Figure 32D-E). To verify that cell cycle asynchronies in PP1-heterozygous were the result of uneven nuclear distribution, we performed analogous experiments in *shackleton* mutants, a mutant defective in nuclear spreading (Yohn et al., 2003), but not in cell cycle regulation (Experimental Methods; Figure 33A-B). *shkl* mutants showed a non-uniform distribution of nuclei along AP axis (Figure 32D, orange bars) and a significant degree of asynchrony, which increased during blastoderm divisions (Figure 32H). A large spread in the timing of mitosis 13 was also observed in optogenetic RhoGEF2 embryos, in which nuclear spreading was impaired by uniform blue light illumination during cycles 4-8 (Figure 32J, dark red bar). Finally, embryos with nuclear spreading defects often have large regions undergoing an extra mitosis (Figure 33C-D). Collectively, these observations argue that a non-uniform NC ratio generates a lack of tissue-wide synchrony and improper control in the number of nuclear divisions preceding the maternal-to-zygotic transition.

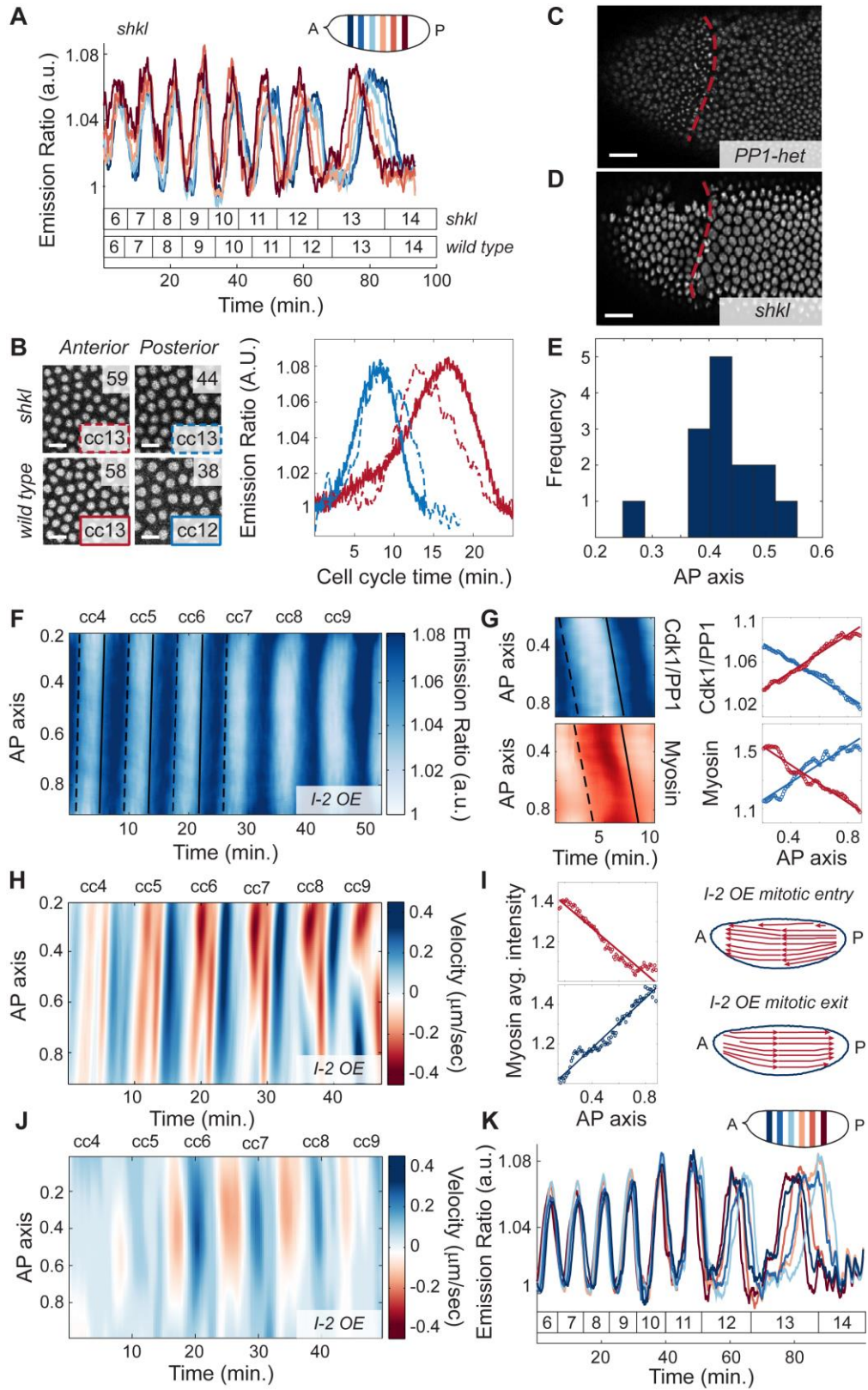


Figure 33: *shackleton* controls nuclear spreading without affecting the cell cycle; characterization of traveling waves of Cdk1/PP1 activity in early embryos. A) Emission ratio of FRET sensor averaged in different regions of the surface of a *shkl* embryo at cell cycles 6-13. Boxes delineate cell cycle timing for *shkl* and wild type embryos. B) Top: nuclear density in anterior and posterior regions of a *shkl* embryo in cell cycle 13. Bottom: nuclear density in anterior and posterior regions of a wild type embryo in cell cycle 12 and 13. Inset, number of nuclei in region. Scale bars, 10 μ m. Right panel: Cdk1 to PP1 activity plotted for wild type cell cycle 12 (blue solid line), wild type cell cycle 13 (red solid line), the anterior side of a *shkl* embryo at cell cycle 13 (red dotted line), and the posterior side of a *shkl* embryo at cell cycle 13 (dotted blue line). C-D) Snapshot of anterior side of a PP1-het (C) and a *shkl* (D) embryo undergoing an extra division. Red dotted line: extra division boundary. Scale bars, 20 μ m. E) Histogram of cell cycle 1 nuclear distribution along AP axis measured from fixed wild type embryos stained with DAPI (n=11). F) Heat map of Cdk1 to PP1 activity along the AP axis of a UAS-I2 overexpressing embryo for cell cycles 4-9. Dashed line: mitotic entry wave front; solid line: mitotic exit wave front. G) Heat maps of Cdk1 to PP1 activity (top left) and myosin levels (bottom left) along the AP axis of a cell cycle 6 UAS-I2 overexpressing embryo with corresponding Cdk1 and myosin gradients during mitotic entry and exit (right panels). Blue points and lines: gradients during mitotic entry with best fit; red points and lines: gradients during mitotic exit with best fit; dashed line: mitotic entry wave front; solid line: mitotic exit wave front. H) Heat map of cortical flow velocity along the AP axis of an embryo with intermediate I-2 overexpression for cell cycles 4-9. I) Myosin intensity profiles across AP axis during mitotic entry (top left panel) and mitotic exit (bottom left panel) of a UAS-I2 embryo. Streamlines showing direction of cortical flows (red arrows) during mitotic entry (top right panel) and exit (bottom right panel) in a UAS-I2 embryo. J) Heat map of cytoplasmic flow velocity along the AP axis of an embryo with intermediate I-2 overexpression for cell cycles 4-9. K) Emission ratio of FRET sensor averaged in different regions of the surface of an embryo with intermediate I-2 overexpression at cell cycles 6-13.

To test the hypothesis that the cell cycle asynchronies in PP1-heterozygous and *shkl* embryos were due to asymmetries in nuclear distribution, we introduced these mutants in genetic backgrounds that made embryos unable to respond to changes in the NC ratio. We generated PP1-heterozygous and *shkl* mutant embryos which were also mutant in *chk1* and *chk2*, the two main effectors kinases of the DNA replication

checkpoint. These genetic manipulations render embryos unable to sense the NC ratio and slow down the cell cycle during the blastoderm divisions (Farrell and O'Farrell, 2014; Sibon et al., 1997). Embryos heterozygous for PP1 and mutant for *chk1* and *chk2* and *shkl/chk1/chk2* triple mutants, while displaying similar nuclear spreading defects as PP1-het and *shkl* embryos (Figure 32G, light blue and orange bars), retained cell cycle synchrony (Figures 32F and 32I). These experiments confirm that uniform nuclear positioning is required for uniform activation of the DNA replication checkpoint and cell cycle synchronization. This is demonstrated by the quantification of the time delay between the first nucleus to enter anaphase and the last nucleus in cell cycle 13. Wild type and *chk1/chk2* mutants showed a delay of at most 2 minutes (Figure 32J, navy blue bars). On the contrary, embryos with perturbations that resulted in non-uniform nuclear spreading, such as PP1-heterozygous, *shkl*, or optogenetic RhoGEF2 embryos exposed to uniform blue light, showed significantly longer anaphase delays of 10-13 minutes (Figure 32J). These delays were reduced to 3-4 minutes in embryos which also lacked *chk1* and *chk2* (Figure 32J), confirming that they were mainly due to asymmetries in the NC ratio.

3.4 Discussion

The cleavage divisions of early embryogenesis require precise coordination of biochemical signals and mechanical properties of the cytoskeleton and of the cytoplasm. We have uncovered how the cell cycle oscillator drives changes in the mechanical

properties of the *Drosophila* embryo, thereby ensuring accurate nuclear positioning and maintenance of mitotic synchrony at the maternal-to-zygotic transition.

Our experiments reveal insights into the spatial regulation of the cell cycle. Previous models of cell cycle synchrony have proposed that nuclei are either coordinated independently by oscillations that are very restricted in space (Su et al., 1998) or that waves synchronize the entire cytoplasm (Chang and Ferrell, 2013). Here, we demonstrate that the spreading of PP1 activity to couple nuclear and cortical dynamics is required for mitotic synchrony. Moreover, forcing the system to trigger wave-like spreading of PP1 throughout the entire embryo is also incompatible with proper nuclear positioning (Figure 33E-J). Thus, we propose that the morphogenetic processes needed for the establishment of mitotic synchrony require that PP1 activity spreads across length scales similar to the distance between nuclei and the cortex.

The functional significance of localized activation of PP1 is to drive the activation of cortical actomyosin in a spatially restricted manner, which results in myosin II gradients closely linked to the position of the nuclear cloud. Myosin II gradients can drive cortical and cytoplasmic flows by causing tension imbalances at the cortex (Mayer et al., 2010). The precise spatiotemporal relationship between the position of nuclei, the cell cycle oscillator and the accumulation of myosin II provide features important for proper positioning. Indeed, cortical flows converging toward the top of the nuclear cloud have exactly the directionality needed to generate cytoplasmic flows

inside the embryo and distribute nuclei along the embryo. Consistently, contractions are only observed prior to uniform nuclear positioning. Once nuclei have filled the embryo, myosin II recruitment becomes uniform and unable to generate significant flows, as demonstrated also by uniform optogenetic activation of Rho signaling (Figure 30). This implies that the self-organized mechanism driving nuclear spreading is intrinsically robust, automatically adjusting the strength and properties of cortical and cytoplasmic flows to the degree of nuclear spreading. Moreover, this mechanism yields accurate nuclear positioning in the face of variability in the position of the nucleus at fertilization (Figure 33E).

Two non-mutually exclusive models had been previously proposed for nuclear spreading. In the local disassembly model actin dynamics in the cytoplasm drive nuclear movements (von Dassow and Schubiger, 1994), while in the cortical contraction model nuclear movements are driven by cortical actomyosin (Royou et al., 2002). These studies relied on pharmacological perturbations, which have the pitfall of influencing both cytoplasmic and cortical components. To distinguish the contribution of the two mechanisms to nuclear spreading, we used optogenetics to precisely control cortical contractility in space and time (Izquierdo et al., 2018). This approach allowed us to demonstrate that nuclear positioning is mainly driven by cortical contractions through the generation of cytoplasmic streaming. Quantitatively, the speed, the direction and the duration of the cytoplasmic flows are very close to the physical parameters needed for

uniform nuclear distribution, suggesting that the generated cortical forces have the correct amplitude to guarantee mitotic synchrony.

Cytoplasmic flows are ubiquitous in biology (Goldstein and van de Meent, 2015; Quinlan, 2016), yet whether they are functionally relevant during early embryogenesis or are an epiphenomenon, simply arising as a consequence of cortical flows, is moot. Here, we have demonstrated an important function for cytoplasmic flows in regulating nuclear spreading, ensuring that all nuclei undergo the same number of divisions and that the cell cycle remains synchronous at the maternal-to-zygotic transition. This synchrony guarantees that all nuclei in the embryo initiate cellularization and gastrulation at the same time, thus favoring proper coordination of morphogenesis.

The integration of biochemical and mechanical signals is a common feature of biological systems and must be achieved across very different spatial and temporal scales. Studying this integration in large embryos allowed us to gain rigorous, quantitative insights on the mechanisms by which biochemical signals and mechanical properties of tissues can be integrated over large spatial scales (order 1 mm). Since both chemical and physical mechanisms of cell communication are emerging as general properties for the regulation of collective tissue dynamics (Deneke and Di Talia, 2018; Gross et al., 2017; Munjal et al., 2015), we speculate that their understanding in the regulation of early embryogenesis reveals general principles for the integration of biochemical and mechanical signals in complex tissues.

3.5 Experimental Methods

3.5.1 Experimental Model and Subject Details

All *Drosophila melanogaster* stocks that were used to generate the lines for this study are described in the Table 3. Flies in a $y^1 w^1$ background were crossed to the desired transgenes and used as wild type controls and are referred to as wild type in the manuscript. For PP1-heterozygous experiments, we used a stock in which 2 genes encoding PP1 α are mutated (*PP1-87B* and *PP1-96A*). To image unfertilized and activated eggs, we crossed males expressing a dominant mutation in $\beta 2$ tubulin (*betaTub85D*), which produces immotile sperm that is unable to fertilize eggs, to wild type females. For all experiments, adult female and male flies were raised at 25°C on standard molasses food. For embryo collection, flies were placed in cages with apple juice agar plates and yeast paste. Embryos were collected on apple juice agar plates after 0–1 hr at 25°C. Genetic crosses and cages of flies expressing optogenetic constructs were kept in the dark.

Table 3: Key Resources used in this Chapter

REAGENT or RESOURCE	SOURCE	IDENTIFIER
Chemicals, Peptides, and Recombinant Proteins		
Citra Solv Concentrated Cleaner & Degreaser	www.citrasolv.com	N/A
Trypan Blue Solution, 0.4%	Gibco	Cat #: 15250061
Halocarbon Oil 27	Sigma	Cat #: 9002-83-9
Deep Golden Amber Filter	www.leefilters.com	No: 135
Experimental Models: Organisms/Strains		
<i>D. melanogaster</i> : <i>w</i> ; <i>Cdk1-FRET</i> ; <i>His2Av-mRFP</i>	S. Di Talia	(Deneke et al., 2016)

<i>D. melanogaster</i> : <i>y[1] w[*]; P{w[+mC]=PTT-GC}CycB[CC01846]</i>	Bloomington Drosophila Stock Center	BDSC: 51568; FlyBase: FBst0051568
<i>D. melanogaster</i> : <i>w[*]; Pp1-87B[87Bg-3] e[1] Pp1alpha-96A[2]/TM6B, Tb[1]</i>	Bloomington Drosophila Stock Center	BDSC: 23699; FlyBase: FBst0023699
<i>D. melanogaster</i> : <i>w[*]; P{w[+mC]=sqh-mCherry.M}3</i>	Bloomington Drosophila Stock Center	BDSC: 59024; FlyBase: FBst0059024
<i>D. melanogaster</i> : <i>w; AniRBD-GFP</i>	T. Lecuit	(Munjal et al., 2015)
<i>D. melanogaster</i> : <i>w*; P{His2Av-mRFP1}II.2</i>	Bloomington Drosophila Stock Center	BDSC: 23651; FlyBase: FBst0023651
<i>D. melanogaster</i> : <i>w*; P{His2Av-mRFP1}III.1</i>	Bloomington Drosophila Stock Center	BDSC: 23650; FlyBase: FBst0023650
<i>D. melanogaster</i> : <i>w;; PCNA-TagRFP-T</i>	S. Di Talia	(Deneke et al., 2016)
<i>D. melanogaster</i> : <i>w[*]; If/Cyo; P[w+, UASp>RhoGEF2-CRY2::mCherry]/TM3, Ser</i>	S. De Renzis	(Izquierdo et al., 2018)
<i>D. melanogaster</i> : <i>w[*]; If/CyO; P[w+, UASp>RhoGEF2-CRY2]/TM3, Ser</i>	S. De Renzis	(Izquierdo et al., 2018)
<i>D. melanogaster</i> : <i>w[*]; P[w+, UASp>CIBN::pmGFP]/Cyo; Sb/TM3, Ser.</i>	S. De Renzis	(Guglielmi et al., 2015)
<i>D. melanogaster</i> : <i>w¹¹¹⁸; P{osk-GAL4::VP16}A11/CyO</i>	Bloomington Drosophila Stock Center	BDSC: 44241; FlyBase: FBst0044241
<i>D. melanogaster</i> : <i>w; grp²⁰⁹ lok³⁰/grp^{z5170} lok³⁰</i>	J. Sekelsky	N/A
<i>D. melanogaster</i> : <i>w;; shk^{GM130}/shk^{GM163}</i>	R. Lehmann	(Yohn et al., 2003)
<i>D. melanogaster</i> : <i>w[*]; P{ry[+t7.2]=neoFRT}82B P{w[+mC]=ovoD1-18}3R/st[1] betaTub85D[D] ss[1] e[s]/TM3, Sb[1]</i>	Bloomington Drosophila Stock Center	BDSC: 2149; FlyBase: FBst0002149
<i>D. melanogaster</i> : <i>Df(3L)AC1, m[roe-1] p[p]/TM3, Sb[1]</i>	Bloomington Drosophila Stock Center	BDSC: 997; FlyBase: FBst0000997
<i>D. melanogaster</i> : <i>y[1] w[1118]; PBac{y[+mDint]=3HPy[+]}I-2[C362]</i>	Bloomington Drosophila Stock Center	BDSC: 16350; FlyBase: FBst0016350
<i>D. melanogaster</i> : <i>w; sqh::GFPmoesinABD</i>	D. Kiehart	N/A

<i>D. melanogaster</i> : <i>w</i> [*]; <i>P</i> { <i>w</i> [+ <i>mC</i>]= <i>UAS-I-2.HA</i> } <i>G</i> ; <i>P</i> { <i>w</i> [+ <i>mC</i>]= <i>UAS-Pp1-87B.HA</i> } <i>H-1/TM6B, Tb</i> [1]	Bloomington Drosophila Stock Center	BDSC: 24101; FlyBase: FBst0024101
<i>D. melanogaster</i> : <i>w</i> [1118];; <i>P</i> { <i>w</i> [+ <i>mC</i>]= <i>GAL4::VP16-nos.UTR</i> } <i>CG6325</i> [<i>MVD1</i>]	Bloomington Drosophila Stock Center	BDSC: 4937; FlyBase: FBst0004937
<i>D. melanogaster</i> : <i>w</i> ; <i>twine-GFP His2Av-mRFP</i>	S. Di Talia	This study
Software and Algorithms		
MATLAB R2018a	Mathworks	N/A
ImageJ	https://imagej.nih.gov/ij/	N/A
Adobe Illustrator CC 2018	Adobe.com	N/A
Ilastik	www.ilastik.org	N/A
JMP	www.jmp.com	N/A

3.5.2 Method Details

3.5.2.1 Embryo Manipulations

Following collection, embryos were dechorionated with 50% bleach for 1 min, rinsed with water and mounted in halocarbon oil on a gas-permeable membrane and covered with a glass coverslip. To visualize cytoplasmic flows, yolk granules were stained by permeabilizing embryos with a solution of 10% CitraSolv in water for 2 minutes and immersing them in Trypan Blue for 1 minute.

3.5.2.2 Microscopy

Imaging experiments were performed with an upright Leica SP8 confocal microscope, a 20×/0.75 numerical aperture oil-immersion objective, an argon ion laser, and a 561-nm diode laser, unless stated otherwise. For the analysis of the Cdk1/PP1 sensor activity at the surface, as well as cortical contractions, we acquired images (800 × 300 pixels, pixel size: 0.56 μm) with a frame rate of 1/2.89 s. For analysis of the Cdk1/PP1

sensor along the axial direction, z-stack images (296×80 pixels, pixel size $1.51 \mu\text{m}$) were acquired in $10 \mu\text{m}$ steps with a frame rate of $1/1.41$ s. For the analysis of cytoplasmic flow, we acquired stacks of raw confocal sections (800×400 pixels, pixel size: $0.727 \mu\text{m}$) of cytoplasm (Trypan Blue) and nuclei (PCNA-TagRFP) with an axial distance of about 50-60 microns and sampling of about 20 seconds. Multiphoton imaging of CyclinB-GFP His2Av-mRFP embryos was performed on an Olympus FV1000 using a $25\times/1.05$ water immersion lens (512×256 pixels, pixel size: $1.25 \mu\text{m}$) with a frame rate of $1/2$ s.

For optogenetic experiments, imaging was performed with a Zeiss LSM 780 NLO confocal microscope equipped with a 561-nm diode laser, and an argon laser. A $32\times/0.85$ NA water immersion objective was used for image acquisition. For sample location, bright field illumination was filtered through a Deep Amber lighting filter. The microscope was controlled through the Zen Black software whereas photo-activation protocols were carried out with the Pipeline Constructor Macro (Izquierdo et al. 2018).

For FRAP experiments, imaging was performed with an upright Leica SP8 confocal, a $20\times/0.75$ numerical aperture oil-immersion objective, an argon ion laser, and a 561-nm diode laser. For embryos co-expressing Cdc25^{Twine}-GFP and His2Av-mRFP, $75 \mu\text{m} \times 75 \mu\text{m}$ square areas were bleached for 1.5 min. with a 488-nm laser (pinhole: 7 AU) spanning $20 \mu\text{m}$ axially. We acquired fluorescence recovery images (800×300 pixels, pixel size: $0.56 \mu\text{m}$, pinhole: 1 AU) with a frame rate of $1/2$ s. For embryos expressing PCNA-TagRFP, $115 \mu\text{m} \times 115 \mu\text{m}$ square areas were bleached for 1.5 min. with both a

488-nm laser and a 561-nm laser (pinhole: 7 AU) spanning 20 μm axially. We acquired fluorescence recovery images (800 \times 300 pixels, pixel size: 0.727 μm , pinhole: 1 AU) with a frame rate of 1/2 s.

3.5.2.3 Production of *endos*^{S68D} and *I-2* mRNA

Endos-S68D ssRNA was synthesized by in vitro transcription of a DNA template containing the T7 promoter sequence on the 5' end. The DNA template was generated by introducing *Endos-S68D* in pBluescript vector via Gibson assembly following PCR amplification of genomic DNA from *w*¹¹¹⁸ flies using Q5 High-Fidelity DNA Polymerase. The S68D point mutation was generated by fusing (in the Gibson assembly reaction) two PCR fragments in which the mutation was incorporated through the primers. Amplified DNA templates were in vitro transcribed (Ambion Megascript Kit) and diluted to a final concentration of 1 mg/mL. The primers used for PCR amplification were: T7-endos-fwd (5' - CTC ACT ATA GAT GAG CTC CGC GGA AGA AAA C - 3'), T7-endos-rev (5' - TCC GCG GAG CTC ATC TAT AGT GAG TCG TAT TAC AAT TC - 3'), endos-S68D-fwd (5' - GCA GAA GGG GCA AAA GTT CTT CGA CGA CGG C - 3'), endos-S68D-rev (5' - AGA ACT TTT GCC CCT TCT GCA GCC TTT TC - 3'), pBSK-T7-fwd (5' - TAT CGA TAA GCT TGA TAT CGG ATT AAG TTG GGT AAC GC - 3'), S68D-pBSK-rev (5' - TGG ATC CCC CGG GCT GCA GGT TAG CTC GTC GCC GGG AAC - 3').

I-2 mRNA was synthesized by in vitro transcription of a DNA template containing the T7 promoter sequence on the 5' end. The DNA template was assembled

by PCR amplification of a pGEX plasmid including human *Inhibitor-2* sequence (gift from S. Kornbluth). Amplified DNA templates were in vitro transcribed (Ambion Megascript Kit) and diluted to a final concentration of 1 mg/mL. The primers used for PCR amplification were: Inh2-T7-fwd (5' – TAA TAC GAC TCA CTA TAG GGA TGG CGG CCT CGA CGG CC - 3'), Inh2-rev (5' – CTA TGA ACT TCG TAA TTT GTT TTG CTG - 3').

3.5.3 Quantification and Statistical Analysis

3.5.3.1 Image analysis

All computational operations and image analysis steps were performed with custom-written MATLAB algorithms with the Image Processing Toolbox unless otherwise noted.

3.5.3.2 Identification of the phosphatase regulating the FRET biosensor

Previous work argued that a mitotic phosphatase must be important in the regulation of the biosensor (Gavet and Pines, 2010). To identify it, we used injection of mRNA encoding inhibitors specific for the two major mitotic phosphatases, PP2A and PP1. To inhibit PP2A, we injected mRNA encoding a mutant version of Endosulfine (Endos-S68D), a phosphomimetic mutant that strongly suppresses PP2A (see below for Methods). Upon injection of *endos*^{S68D} mRNA, we observed significant mitotic exit defects (data not shown). However, the biosensor was still fully dephosphorylated, albeit at a slightly lower rate (Figure 21A). By contrast, injection of mRNA encoding

Inhibitor-2 (I-2) (see below for Methods), a specific inhibitor of PP1 activity when highly over-expressed, caused the biosensor to remain in a phosphorylated state (Figure 21B) and nuclei to arrest in metaphase, consistent with previous observations that PP1 is required for mitotic exit (Wu et al., 2009). The role of PP1 in the dephosphorylation of the biosensor was further supported by genetic manipulations reducing the levels of I-2, which cause a decrease in the level of phosphorylation of the biosensor in mitosis (Figure 23D). We conclude that the Cdk1 biosensor is mainly dephosphorylated by PP1, so we refer to it as Cdk1/PP1 biosensor.

3.5.3.3 Quantification of the Cdk1/PP1 biosensor

The Cdk1/PP1 activity ratio was estimated as in (Deneke et al., 2016). To generate heat maps, the Emission Ratios were averaged over regions of 4.48 μm along the AP axis. Slight differences in the plane of focus across the embryo, as well as small drifts during imaging, cause trends in the data that were reduced using the following procedure. First, we normalized the emission ratio for each region with the average in that region during cell cycle 12, when the amplitude of Cdk1/PP1 oscillations is essentially uniform in space. Then, we de-trended the data by subtracting the dynamics in each region with that obtained using Smoothing Splines with a very high smoothing parameter ($1/p=10^9$) to extrapolate the low frequency behavior of the average FRET signal across the embryo. Normalized and de-trended data were then smoothed in time and space using the Savitsky-Golay filter (3rd order polynomial over 55 points in

time and 1st order polynomial over 7 points in space). Similar smoothing with Savitsky-Golay filters was used to generate the myosin II and Rho activity heat maps.

3.5.3.4 Quantification of cortical and cytoplasmic flows

Stacks of raw confocal sections of Trypan Blue stained yolk granules and nuclear marker (PCNA-TagRFP) were sum-projected and Gaussian-filtered (width of 10 μm and standard deviation 6 μm) in order to increase signal-to-noise ratio as a pre-processing image analysis step. Nuclear tracking was performed by means of Ilastik trained on several embryo datasets. Binary images obtained with segmentation were labeled and centroids were used to extract the position of nuclei which was then fed to a tracking algorithm based on minimum distance criterion. Cytoplasmic velocity fields were measured by means of Particle-Image-Velocimetry. Briefly, stripes of 35 μm (Anterior-Posterior direction) by 15 μm (Dorsal-Ventral or lateral direction) were used as templates and probed within regions of 60 μm by 30 μm to find best correlation spots, with a threshold correlation coefficient of 0.7. PIV was calculated for ten thousand unique points randomly distributed within the embryo at each time interval. A sampling of around 20 to 30 seconds was used to get reliable local displacements yet maintaining high correlations. The obtained velocity fields were time-averaged over a range of 10 seconds and then linearly interpolated on a square grid with 4 μm spacing. One-dimensional heat maps were generated by averaging the AP component of the velocity over the whole embryo and on a stripe 100 μm -thick, centered on the AP axis and

interpolating it on a dense uniformly spaced one dimensional grid with spacing equivalent to 500 points on the length of the embryo. Each time interval was then used as a column in a matrix represented with the appropriate color-map.

Lagrangian trajectories of particles such as those shown in Figures 4 and 5 were computed by seeding uniformly spaced points and integrating numerically the equation $\dot{\mathbf{x}}(t) = \mathbf{v}(\mathbf{x}(t))$ with Euler's scheme using spatially interpolated velocity fields from PIV data at each time interval. Integration was performed for the whole duration of each interphase. Backward integration of particle trajectories along the AP axis was performed by integrating $\dot{\mathbf{x}}(t) = \mathbf{v}(\mathbf{x}(t))$ with the mid-point method backward in time and using interpolated 1-D values of the AP velocity as described above. Integration was performed for the whole duration of each shown dataset. The vorticity $\boldsymbol{\omega} = \nabla \times \mathbf{v}$ was computed using the curl function in MATLAB, after having verified that on simulated Stokes flows maxima and minima are on the boundary, as expected.

3.5.3.5 Validation of cortical and bulk cytoplasmic flow measurements

In order to verify the effectiveness of our approach for visualizing and quantifying cytoplasmic flows, we compared the velocities obtained with PIV of His2Av and yolk granules (stained with Trypan Blue) with those obtained using a Fluorescence Recovery After Photobleaching (FRAP) method on cytosolic proteins (Carroll et al., 2014), which should act as soluble tracers (Cdc25^{Twine}-GFP or PCNA-TagRFP). Particle

Image Velocimetry (PIV) provides an accurate methodology for the reconstruction of flows with high spatiotemporal resolution. However, since PIV is based on cross-correlation between images, it can detect movements of structures with size of at least a few units of digital resolution, in our case not smaller than a few microns. As a consequence, it does not allow the tracking of featureless tracers, such as signals coming from a soluble molecule which is uniformly distributed. Therefore, it is possible that the movement detected with our signal and methods (His2Av, yolk granules and PIV) reflects the movement of larger scale structures, either bound to the actomyosin network or influenced by its mesh size. Indeed, in response to an external impulsive pressure, during blebbing the soluble aqueous component of the cytoplasm (cytosol) and the actomyosin gel have been shown to move relative to each other on timescales of few seconds across several microns (Mitchison et al., 2008). To validate our measurements, we compared the movement obtained for both His2Av-mRFP and yolk granules to that of soluble markers (Cdc25^{Twine}-GFP and PCNA-TagRFP). The latter was assessed by adapting a FRAP method for measuring flow using soluble fluorescent proteins (Carroll et al., 2014). Following photobleaching, the movement of the dark bleached region is described by an advection-diffusion equation. In the absence of advection, the bleached region remains close to its initial location and fluorescence recovery follows purely diffusive dynamics. In the presence of advection, the bleached area is transported by the flow and flow velocity can be obtained by tracking the bleached area (Carroll et al.,

2014). We optimized the bleaching conditions to follow reliably the bleached area for 2-3 minutes and could observe that it moves (Figures 27A-B and Figure 28A-B), strongly supporting that the cytosol is being advected during cell cycles 4-6. To measure velocity, we inferred the position of the bleached area by fitting the front of the fluorescence profile across space with a sigmoidal function of the form: $I(x) = C * \left(1 - \operatorname{erf}\left(\frac{x-a}{w}\right)\right) + B$, where a is the inferred position at a particular time, B is the background, C is the amplitude, and w is the width of the sigmoid, which is linked to diffusion (Figure 27B and Figure 28B). From the derivative of a smoothing spline fit (parameter $p=1/100$) of the position a , we extrapolated velocity as a function of time. Since we performed these experiments in embryos co-expressing Cdc25^{Twine}-GFP and His2Av-mRFP (for cortical flows) and PCNA-TagRFP and stained yolk granules (for cytoplasmic flows), we could directly correlate flow measurements from PIV and FRAP. Figures 27C and 28C show that there is a strong 1:1 agreement between the two measurements, confirming that our PIV-based approaches measure the flow of cytosol both at the cortex and in the bulk of early *Drosophila* embryos.

3.5.3.6 Prediction of cortical velocity from myosin gradients

To determine the relation between cortical flows and myosin spatial distribution, we used a mathematical model previously proposed by (Mayer et al., 2010). To keep presentation self-contained, we repeat the derivation of the model (Mayer et al., 2010).

The central assumption of the model is that cortical tension is proportional to myosin levels and a viscous term, characterizing the physical nature of cortical flows:

$$T(x) = C(x) + \eta \frac{\partial v}{\partial x} \quad (1)$$

where T is the tension, C is the force (contractility) generated by myosin, which we take to be proportional to myosin concentration, and η is the viscosity of the cytoplasm near the cortex. Flows arise from gradients in tension and are related to those gradients through an overdamped relationship characterized by a friction coefficient γ :

$$\frac{dT}{dx} = \gamma v \quad (2)$$

From these relationships, one obtains:

$$\frac{\partial^2 v}{\partial x^2} - \frac{1}{\lambda^2} v = -\frac{1}{\eta} \frac{\partial C}{\partial x} \quad (3)$$

which can be used to fit cortical flows from measured myosin gradients. Myosin spatial profiles were fitted using Smoothing Splines with smoothing parameter $1/p=100$ and gradients were evaluated using the differentiate function in MATLAB. These gradients were then used to solve the equation linking the cortical flow velocity and myosin gradients using standard numerical methods. An important parameter of the model is the length scale: $\lambda \equiv \sqrt{\eta/\gamma}$, which gives the spatial decay length of velocity in response to a step change in myosin levels (contractility), thus providing a length scale

over which actomyosin contractility is correlated. We found that cortical flows can be fit well with $\lambda \sim 100 \mu\text{m}$ and used this value to generate the data shown in Figure 26E.

3.5.3.7 Cytoplasmic F-actin and myosin II dynamics

To understand the dynamics of F-actin and myosin II in the cytoplasm, we imaged embryos expressing Moesin-ABD-GFP (F-actin marker) and myosin II-mCherry in the same embryos at different depths from the surface of the embryo (Figure 25E-F). These imaging experiments show several important features of actomyosin dynamics. First, the dynamics of F-actin and myosin II are strongly correlated both at the cortex and in the cytoplasm (Figure 25E-F). Second, the oscillations at the cortex are much more pronounced than cytoplasmic oscillations (Figure 25E-F). Third, the cytoplasmic and cortical oscillations have different timing. Cytoplasmic F-actin and myosin II levels have dynamics similar to that of the Cdk1/PP1 biosensor and increase during mitosis, as previously observed in vertebrate embryos (Field et al., 2011). On the contrary, cortical levels increase about 2 minutes earlier and are highest in interphase (Figure 25E-F and Figure 24). Finally, spatial regulation of cytoplasmic F-actin and myosin II is also coupled to nuclear positioning with oscillations observed in cytoplasmic regions surrounding nuclei, but not in regions away from the nuclear cloud (Figure 25G-H).

3.5.3.8 Characterization of *shackleton* mutant

The gene *shackleton* (*shkl*) was identified in a screen for mutants affecting the specification of germ cells during early embryonic development (Yohn et al., 2003). It

was found that the decrease in germ cells was probably explained by defects in nuclear spreading, as nuclear positioning at the posterior of the embryo is required for germ cell specification (Yohn et al., 2003). Using imaging of both fixed and living embryos, we confirmed that indeed *shkl* mutant embryos are defective in nuclear spreading (Figure 32D). Since the cell cycle drives nuclear spreading, we asked whether these defects could be due to defects in cell cycle regulation. Three main lines of evidence argue against this scenario: 1. The oscillations of the Cdk1/PP1 biosensor in the region of the nuclei are very similar to those observed in wild type, suggesting that the core of the cell cycle oscillator is not influenced (Figure 33A; Figure 32B, 32H); 2. Cell cycle timing is normal for each NC ratio (Figures 33A-B); 3. No morphological mitotic defects are observed. Collectively, these observations argue that *shkl* does not encode a gene product important for cell cycle regulation. Thus, *shkl* mutants provide an experimental system to test the effect of impaired nuclear spreading on mitotic synchrony.

3.5.3.9 Analysis of traveling waves of Cdk1/PP1 activity

Our experiments indicate an important role for the local spreading of PP1 activity in the coordination of the early cell cycles. To further elucidate the importance of this spatial dynamics, we sought conditions that would force PP1 activity to spread through the entire embryo. We found that embryo-wide oscillations of the Cdk1/PP1 biosensor could be generated in a fraction of embryos, in which expression of an UAS-I-2 construct was driven maternally by the nanos-Gal4 driver (maternal genotype: *w*;

UAS-Inh-2/Cdk1-FRET His2AvRFP; Cdk1-FRET His2AvRFP/nanos-Gal4). Specifically, we observed global oscillations of the Cdk1/PP1 biosensor, which spread through the entire embryo as traveling waves (Figure 33F). Even though the mechanism by which I-2 can facilitate embryo-wide oscillations of PP1 activity is unclear, we speculate that this is due to its function as an inhibitory chaperone, arguing that it might work as an inhibitor during mitotic entry and as an activator during mitotic exit (Heim et al., 2017). Our ability to generate traveling waves of Cdk1/PP1 activity allowed us to test whether such waves are compatible with efficient nuclear spreading and mitotic synchrony. To elucidate how waves of Cdk1/PP1 drive the recruitment of actomyosin at the cortex, we quantified both the biosensor and myosin II dynamics. We found that in these embryos there are traveling waves of myosin II that closely follow the Cdk1/PP1 waves (Figure 33G). In fact, myosin II waves showed the same propagating dynamics as the Cdk1/PP1 waves, as evidenced by comparing the Cdk1/PP1 propagation front during mitotic exit (Figure 33G, dotted line, top left panel) to the myosin II recruitment wave front (Figure 33G, dotted line, bottom left panel), which was shifted by the same time delay of 1-2 minutes observed in wild type. These waves have the consequence of generating alternating myosin II gradients, a gradient in one direction along the anterior-posterior axis at mitotic entry and an opposite one at mitotic exit (Figure 33G, right panel). These alternating gradients generate cortical contractions that are no longer linked to nuclear position. Instead cortical flows are directed toward one pole at mitotic entry and

towards the other pole at mitotic exit (Figure 33H-I). As expected, cytoplasmic flows respond to changes in cortical flows and also show a pattern in which the entire cytoplasm flows towards one pole during mitotic entry and towards the other pole during interphase (Figure 33J). This pattern of cytoplasmic flows would move more or less uniformly the entire nuclear cloud toward alternating poles and would not facilitate nuclear spreading. In fact, we observe a strong disruption of nuclear spreading in many of these embryos with nuclei occupying a small fraction of the surface of the embryo at cell cycle 10. Similar to PP1 heterozygous and *shkl* embryos, non-uniform positioning of nuclei results in significant asynchronies in the cell cycle at the maternal-to-zygotic transition (Figure 33K). Based on all these observations, we conclude that traveling waves in the activity of Cdk1/PP1 are incompatible with mitotic synchrony during early *Drosophila* embryogenesis.

3.5.3.10 Statistical analysis

All statistical analyses were performed using JMP Pro. Statistical comparisons between multiple samples was by one-way ANOVA followed by Tukey's test to compare all pairs. For all measurements, at least three biological replicates were used unless otherwise noted.

4. Conclusions: Chemical waves and cytoplasmic streaming as emerging self-organizing principles in cell and developmental biology

Section 4.3.1 in this Chapter was adapted from a review article titled: “Chemical waves in cell and developmental biology” published in *J. Cell Biol.*, 217 (4) 1193-1204 (2018). doi: 10.1083/jcb.201701158. The authors were Victoria E. Deneke and Stefano Di Talia.

4.1 Summary

The overarching goal of this dissertation was to uncover organization principles of the embryonic cell cycle in *Drosophila melanogaster*. To this end, I focused my studies on cell cycle synchronization, a collective behavior in fly syncytial embryos where organization principles had not been identified. The early development of *Drosophila melanogaster* is characterized by synchronous divisions that span the entire embryo during the blastoderm stage. Even though mitotic waves in *Drosophila* have been observed since the 1980s, the mechanisms that regulate the such waves have remained elusive. Furthermore, how embryo-wide cell cycle synchrony emerges in this system was also unknown.

My first project uncovered the presence of chemical waves of Cdk1 activity during the syncytial blastoderm divisions and their role in synchronizing the nuclear cycles. I found that the activity of Cdk1 during S-phase synchronizes the cell cycle. This concept was initially developed from the observation that Cdk1 activity dynamics

exhibited a bi-phasic activation. During S-phase, Cdk1 activity ramped up slowly and during M-phase, the Cdk1 activity sensor showed a fast activation. Furthermore, the rate of Cdk1 activation in S-phase strongly correlated with the measured wave speed. This suggested to us that the activity of Cdk1 in S-phase was regulating the speed of the wave and therefore synchronizing the divisions. We tested this idea by studying mutants that would affect the activity of Cdk1 during S-phase. In support of our hypothesis, these mutants had altered S-phase Cdk1 activation rates as well as mitotic wave speeds. Conversely, mutants with impaired Cdk1 regulation during M-phase could still propagate waves, although with a speed slower than wild type. This led us to conclude that the rate of Cdk1 activation during S-phase controls the speed of the Cdk1 and mitotic wave. A prediction came out of this conclusion: if the nuclear divisions were actively coupled during S-phase, then introducing a barrier should impede the propagation of the wave through the diffusion barrier. When I introduced a physical barrier in the embryo during S-phase, I was able to confirm our prediction, since the mitotic wave was unable to go through the barrier. If I introduced it in M-phase, however, the wave propagated unperturbed. This last experiment demonstrated that the synchronous divisions are actively coupled in S-phase and that the observed mitotic waves are purely a kinematic process that follow the delays introduced during S-phase. This work emphasized the importance of chemical waves as a long-range communication mechanism in biology.

A follow up to this project was to study the physical basis of Cdk1 waves in *Drosophila* embryos. A thorough analysis of the Cdk1 activity dynamics revealed that the Cdk1 wave did not spread as a traditional bistable wave. Instead, Cdk1 activity profiles showed an upward “sweeping” trend as a function of time. Our collaborator Massimo Vergassola developed a mathematical model that recapitulated the experimental phenomenology. The difference between his model and the bistable model was that his model was only transiently bistable. In other words, the system was evolving as a function of time and the incorporation of this assumption predicted much faster velocities compared to the bistable model. Importantly, the velocities predicted by the new time-dependent model matched the velocities measured experimentally. We termed these new class of waves “sweep waves”, since they exhibit upwardly sweeping gradients of Cdk1 activity, which lead to wave-like spreading. This work led to the identification of a new physical mechanism for the spreading of chemical waves and a re-examination to model biological phenomena with fast timescales using a time-dependent reaction diffusion model.

My second project focused on the emergence of cell cycle synchronization in early fruit fly embryos. This project started from an observation that during the early cell cycles, before nuclei have migrate to the surface of the egg, oscillations in the Cdk1 to PP1 activity sensor could be detected in certain regions at the embryo surface. This was surprising, given that the field always speculated that the activities of these cell cycle

regulators were restricted to the regions immediately surrounding the nuclei.

Furthermore, the regions that showed oscillations corresponded to the location where myosin would accumulate a few minutes later. This led us to hypothesize that the cell cycle oscillations could be regulating the recruitment of cortical myosin. Indeed, by perturbing the spreading of the cell cycle oscillations we saw effects on myosin accumulation. Furthermore, we noticed that local myosin accumulation resulted in coordinated contractions of the embryo cortex and subsequent cytoplasmic flows deep inside that could spread the nuclei along the AP axis. Through a collaboration with Stefano De Renzis at EMBL Heidelberg we were able to directly test our model using an optogenetic RhoGEF2 tool they had developed. Recruiting RhoGEF2 uniformly to the embryo cortex inhibited cortical contractions and flows, showing that the gradients of myosin at the cortex generate cortical and cytoplasmic flows. In addition, recruiting RhoGEF2 to the cortex of one pole of the embryo led to the flow of nuclei to the opposite pole, confirming that local cortical recruitment of myosin is sufficient to generate contractions and flows. Importantly, embryos with impaired spreading along the AP axis exhibited synchrony defects during the syncytial blastoderm divisions, pointing to the role of this morphogenetic process in establishing embryo-wide synchrony by positioning nuclei uniformly. This project provided insights into the spatiotemporal coordination of biochemical and mechanical signals in a large syncytium as well as the emergence of cell cycle synchrony in *Drosophila* embryos.

4.2 Future Directions

4.2.1 Dissect the mechanisms regulating cell cycle synchrony in early syncytial blastoderm

The work presented in Chapter 2 identified the role of Cdk1 chemical waves in synchronizing the cell cycle during S-phase. Specifically, Cdk1 waves arise from double negative feedback between Cdk1 and Chk1 during activation of the DNA replication checkpoint. Nonetheless, the DNA replication checkpoint is primarily activated during cell cycles 12-13, as shown by two pieces of data: 1. Our Chk1 sensor shows that Chk1 activity increases during S-phase of cell cycles 12-13, and 2. *chk1/chk2* mutants show significantly altered wave speeds during cell cycles 12-13. One natural question that arises is: what synchronizes the cell cycle prior to the activation of the DNA replication checkpoint? Are the S-phase waves in cell cycles 10-11 phase waves? A technical challenge that arises in addressing these questions is that S-phase is remarkably short in cell cycles 10-11, lasting only ~4 minutes (Farrell and O'Farrell, 2014). Furthermore, mitotic wave speeds are the fastest in cell cycles 10-11. As a result, measuring differences in the anaphase timing after introducing a ligation barrier in S-phase has been challenging. In order to overcome these technical challenges, I would study Cdk1 waves in colder temperatures in order to slow down the cell cycle. This can be achieved by designing or adapting a microfluidic device that allows for controlled temperature (Falahati and Wieschaus, 2017). One key assumption in this experiment is that decreasing the temperature does not alter the timing of DNA replication checkpoint

activation. By lengthening nuclear cycles to last twice as long, one can then measure whether the mitotic waves become uncoupled after introducing a ligation barrier during S-phase. The next relevant question if the waves are uncoupled during these early cycles would be to elucidate the positive feedback that in addition to diffusion generates Cdk1 waves.

4.2.2 Dissect the mechanisms of regulation of contractility by the cell cycle

In Chapter 3 our studies identified a role for PP1 in recruiting Rho1 to the regions of the cortex that overlie the nuclei. We observed that Rho activity peaks simultaneously with PP1 activity. Follow-up studies should dissect how PP1 regulates Rho1 recruitment during axial expansion. One possibility is that PP1 recruits cytokinetic machinery that can then activate Rho signaling at the cortex. We have now started to assess the local recruitment of cytokinetic machinery to the regions that overlie nuclei. Ect2, a RhoGEF involved in cytokinetic ring formation, is not locally recruited during cortical contractions. However, Annilin, a scaffold protein required for cytokinesis, is recruited to the cortex in a similar way to myosin II. Therefore, further characterization of what other cytokinetic machinery is playing a role in Rho1 recruitment at the cortex is a potential future direction. Additional insights into what molecular mechanisms regulate Rho signaling at the cortex have come from genetically mapping the *shackleton* (*shkl*) mutant, which exhibited impaired nuclear spreading. Whole genome sequencing of two *shkl* alleles identified *cullin-5* as a potential candidate for *shkl*. Cullin-5 is an E3

ubiquitin ligase. Furthermore, *cullin-5* mutants fail to complement the *shkl* gene. One of the well-characterized targets of Cullin-5 is Src kinase, which has several important functions including signaling to cytoskeletal machinery. Therefore, one hypothesis that emerges from our mutant studies is that Rho signaling could be activated through the Cul5-Src pathway. This can be studied by determining whether overexpression of a constitutively active Src can inhibit cortical contractions, or alternatively, if knockdown of Src can rescue the *shkl* mutant spreading defects. In summary, a combination of genetic tools as well as live imaging of tagged protein candidates can begin to uncover the precise molecular mechanism by which cell cycle signaling recruits actomyosin to a specific region of the cortex.

4.2.3 Dissect the self-organizing principles of nuclear positioning

One of the major themes of Chapter 3 was the self-organizing mechanism by which nuclei ensure their uniform positioning along the AP axis. Before the nuclei have spread, PP1 recruits Rho and myosin locally, which generates cortical and cytoplasmic flows with the precise directionality needed to distribute nuclei across the embryo. Once nuclei have filled the embryo, myosin II recruitment becomes uniform and unable to generate significant flows, providing an automatic stopping mechanism. In order to test the robustness of this system, future studies can use the optogenetic RhoGEF2 system to shuttle nuclei to the one side of the embryo and record the endogenous response to such perturbation. If the spreading mechanism is indeed self-organized and robust, I expect

nuclei to be able to generate a series of endogenous contractions that will result in uniform spreading despite the starting position. Another way to further characterize the organizing nature of the flows is to test the role of geometry or embryo shape on the flows. Given the integration of biochemical and mechanical cues in this process, it is conceivable that embryo curvature or geometry could affect the direction and magnitude of the flows. Round fruit fly embryos have been generated by knocking down the cadherin Fat2 in oocyte somatic cells, which inhibits polarized oocyte elongation (Viktorinova et al., 2009). If nuclei are properly positioned in round embryos, a follow-up study should determine how the interplay between cell cycle signals, cortical cytoskeletal machinery and embryo shape can maintain the self-organizing properties described in Chapter 3.

4.2.4 Dissect the physical properties of cytoplasmic flows

Flows predicted by mathematical modelling of the cytoplasm as a passive viscous fluid (Stokes) responding to forces at the cortex were similar to the flows measured experimentally. Nonetheless, there were deviations at small scales, which suggests that there may be additional effects that governs the physical properties of the cytoplasmic flows. One possibility is that disassembly of the actin network around nuclei during each cell cycle could also regulate the flows at a smaller and local scale. Future studies can model flows using a combination of Stokes and local fluidization of the cytoplasm and determine whether they can account for the small deviations that

were previously observed. In order to assess the contribution of nuclei to the magnitude and direction of cytoplasmic flows, I would induce flows in unfertilized but activated eggs that express optogenetic RhoGEF2 and assess whether these flows are entirely predicted by Stokes flows. Additionally, one can assess the contribution of nuclei by shuttling nuclei to one side of the embryo and determine whether the deviations from Stokes in a fertilized egg are correlated with nuclear position.

4.2.5 Dissect the role of cytoplasmic flows on morphogen gradient formation and patterning

In Chapter 3, we found that cytoplasmic flows move large objects in the egg such as nuclei and yolk granules, but also soluble cytoplasm. An intriguing follow-up study would be to investigate the effects of cytoplasmic flows on gradient formation and patterning. An initial experiment would be to measure Bicoid gradients in wild type and nuclear spreading mutants such as *shackleton* or in optogenetic RhoGEF2 embryos where cortical contractions have been inhibited. Furthermore, other downstream patterning effects can be characterized in these conditions such as *eve* stripe formation, etc. These studies may uncover a previously unidentified role for cytoplasmic flows.

4.3 Perspectives

4.3.1 Chemical waves as a general strategy to organize cellular dynamics in space and time

The multiplicity of biological processes described in Chapter 1 suggests that chemical waves are ubiquitous in living systems. Their role in spreading biological

signals rapidly across a large range of spatial and temporal scales is well established, as is the case in the coordination of embryonic cleavage divisions (Bement et al., 2015; Chang and Ferrell, 2013; Deneke et al., 2016). Conversely, the role of chemical waves in the coordination of cellular dynamics in larger and more complex tissues remain largely unexplored. More specifically, the mechanisms by which cellular transitions are coordinated in space and time and whether collective coordination of processes, such as cell proliferation, is required for normal development remain unclear. Cellular processes in complex tissues are often coordinated by the dynamics of signaling pathways, which are well described by reaction-diffusion models (Murray, 2002). Since waves are commonly observed in this class of mathematical models, it is very likely that more examples of chemical waves will emerge. Recent advancements in imaging methodologies (e.g. intravital imaging) (Weissleder and Nahrendorf, 2015) and the development of molecular biosensors for several signaling pathways (Regot et al., 2014) will allow us to identify waves in a wider range of cellular and developmental processes. A wavefront traveling with little distortion and at constant speed provides sharp and accurate spatiotemporal responses to dynamical signals. These properties might be highly desirable in tissues in which cell differentiation and growth are tightly coupled, as discussed for somitogenesis and eye imaginal disc development.

It will also be fundamental to dissect whether these waves of signaling will emerge as a key mechanism of regulation of tissue morphogenesis and dynamics or

arise simply as a by-product of the feedback mechanisms required to regulate biological dynamics. In some biological contexts, waves arising from the combination of diffusion and non-linear dynamics could pose problems by generating unwanted signals that propagate through tissues (e.g. the fibrillation waves observed during heart contractions (Pandit and Jalife, 2013)) and biological systems might have evolved mechanisms to suppress them. In this review, we have mainly focused on the ability of reaction-diffusion systems to generate sharp wavefronts. However, in two and three dimensions, waves of more complex geometries, for example spirals, can arise and such waves of cAMP signaling have been observed during aggregation of the slime mold (Alcantara and Monk, 1974; Siegert and Weijer, 1995). Noise also can influence the properties of waves. For example, in a bistable system, noise could affect the transition time from the low to the high state and, in principle, initiate unwanted waves. These noise-driven events could be suppressed by precise temporal regulation, so that the initiation of the wave is controlled by an additional input, such as cyclin synthesis in the mitotic waves. The effect of noise on time-dependent bistable waves remains unclear, while for time-independent systems it can be shown that bistable waves, but not unstable waves, are insensitive to noise (van Saarloos, 1998).

From a theoretical standpoint, biology has inspired the development of several reaction-diffusion models. In fact, the first well-understood example of a wave in a reaction-diffusion equation was elaborated by Fisher and Kolmogorov-Petrovsky-

Piskunov to describe the spatiotemporal spread of an allele through a population (Fisher, 1937; Kolmogorov, 1991). Physicists have also been very interested in waves arising in reaction-diffusion systems (often known in physics as Ginzburg-Landau equations), as they capture the behavior of systems undergoing phase transitions (van Saarloos, 1998). For that reason, a great body of theoretical work has been developed and provides the foundation for modeling biological systems. However, physical and biological systems often display fundamentally different characteristics, e.g. biological systems tend to change rapidly with time and are often far from thermodynamic equilibrium. We, therefore, expect that the unique properties of biological systems and our unprecedented ability to measure signaling dynamics in living systems will inspire new theoretical work and reveal important new insights on both the physical and molecular mechanisms by which chemical waves can arise in biology.

4.3.2 The role of cytoplasmic flows in cellular and tissue organization

Even though cytoplasmic flows have been described in a variety of systems, it has been challenging to identify their precise biological functions. In plant cells, cytoplasmic streaming determines plant cell size, which is thought to result from increased metabolic rates in these large cells (Goldstein and van de Meent, 2015). In *Drosophila* oogenesis, it is speculated that cytoplasmic streaming mixes all the contents of the cytoplasm which generates a uniform chemical environment important for early development (Quinlan, 2016). Therefore, these studies suggest that cytoplasmic

streaming is mostly suited for large cells, where diffusion alone cannot transport molecules in the same amount of time. In the case of axial expansion in early *Drosophila* embryos, the role of cytoplasmic flows is to spread nuclei across the AP axis, which could not be accomplished by diffusion alone. Active transport is used to move nuclei in other systems such as skeletal muscle (Roman and Gomes, 2018), but it is unclear how such a mechanism could ensure uniform spreading in fruit fly embryos, since the nuclei at the periphery of the cloud move to a further extent than the nuclei at the center. Whether the flows in *Drosophila* embryos also transport morphogens that can then affect patterning remains to be determined.

Cytoplasmic flows exhibit a high degree of order in the observed flow, resulting in rotational or fountain-like patterns. These patterns could result from inherent self-organizing properties of the cytoskeletal network (Woodhouse and Goldstein, 2013). In fact, cytoplasmic droplets extracted from algae spontaneously induced flows, pointing towards a self-organizing property in the system (Goldstein and van de Meent, 2015). In addition, cytoplasmic streaming can be considered an organizing mechanism in large cells by homogeneously mixing the cytoplasm or by facilitating polarity maintenance, as has been suggested previously (Quinlan, 2016). Therefore, as scientists keep uncovering new examples of cytoplasmic flows in large cells, it will be key to identify their biological function as well as organizing properties.

References

- Acheson, D.J. (1990). *Elementary fluid dynamics* (Oxford; New York: Clarendon Press; Oxford University Press).
- Alcantara, F., and Monk, M. (1974). Signal propagation during aggregation in the slime mould *Dictyostelium discoideum*. *J Gen Microbiol* 85, 321-334.
- Allard, J., and Mogilner, A. (2013). Traveling waves in actin dynamics and cell motility. *Curr Opin Cell Biol* 25, 107-115.
- Allen, N.S., and Allen, R.D. (1978). Cytoplasmic streaming in green plants. *Annu Rev Biophys Bioeng* 7, 497-526.
- Alphey, L., Jimenez, J., White-Cooper, H., Dawson, I., Nurse, P., and Glover, D.M. (1992). *twine*, a *cdc25* homolog that functions in the male and female germline of *drosophila*. *Cell* 69, 977-988.
- Ammerman, A.J., and Cavalli-Sforza, L.L. (1971). Measuring the Rate of Spread of Early Farming in Europe. *Man* 6, 674-688.
- Anderson, G.A., Gelens, L., Baker, J.C., and Ferrell, J.E., Jr. (2017). Desynchronizing Embryonic Cell Division Waves Reveals the Robustness of *Xenopus laevis* Development. *Cell Reports* 21, 37-46.
- Antunes, M., Pereira, T., Cordeiro, J.V., Almeida, L., and Jacinto, A. (2013). Coordinated waves of actomyosin flow and apical cell constriction immediately after wounding. *J Cell Biol* 202, 365-379.
- Aoki, K., Kondo, Y., Naoki, H., Hiratsuka, T., Itoh, R.E., and Matsuda, M. (2017). Propagating Wave of ERK Activation Orients Collective Cell Migration. *Dev Cell* 43, 305-317 e305.
- Ataullakhanov, F.I., Guria, G.T., Sarbash, V.I., and Volkova, R.I. (1998). Spatiotemporal dynamics of clotting and pattern formation in human blood. *Biochim Biophys Acta* 1425, 453-468.
- Aulehla, A., Wiegraebe, W., Baubet, V., Wahl, M.B., Deng, C., Taketo, M., Lewandoski, M., and Pourquie, O. (2008). A beta-catenin gradient links the clock and wavefront systems in mouse embryo segmentation. *Nat Cell Biol* 10, 186-193.

- Baggaley, A.W., Sarson, G.R., Shukurov, A., Boys, R.J., and Golightly, A. (2012). Bayesian inference for a wave-front model of the neolithization of Europe. *Phys Rev E Stat Nonlin Soft Matter Phys* 86, 016105.
- Baker, J., Theurkauf, W.E., and Schubiger, G. (1993). Dynamic changes in microtubule configuration correlate with nuclear migration in the preblastoderm *Drosophila* embryo. *J Cell Biol* 122, 113-121.
- Baker, N.E. (2007). Patterning signals and proliferation in *Drosophila* imaginal discs. *Curr Opin Genet Dev* 17, 287-293.
- Balazsi, G., van Oudenaarden, A., and Collins, J.J. (2011). Cellular decision making and biological noise: from microbes to mammals. *Cell* 144, 910-925.
- Barnhart, E.L., Allard, J., Lou, S.S., Theriot, J.A., and Mogilner, A. (2017). Adhesion-Dependent Wave Generation in Crawling Cells. *Curr Biol* 27, 27-38.
- Belousov, B.P. (1958). A periodic reaction and its mechanism. *Sb Ref Radiats Med Medgiz* 154.
- Bement, W.M., Leda, M., Moe, A.M., Kita, A.M., Larson, M.E., Golding, A.E., Pfeuti, C., Su, K.C., Miller, A.L., Goryachev, A.B., *et al.* (2015). Activator-inhibitor coupling between Rho signalling and actin assembly makes the cell cortex an excitable medium. *Nat Cell Biol* 17, 1471-1483.
- Benink, H.A., and Bement, W.M. (2005). Concentric zones of active RhoA and Cdc42 around single cell wounds. *J Cell Biol* 168, 429-439.
- Bers, D.M. (2002). Cardiac excitation-contraction coupling. *Nature* 415, 198-205.
- Bischof, J., Brand, C.A., Somogyi, K., Majer, I., Thome, S., Mori, M., Schwarz, U.S., and Lenart, P. (2017). A cdk1 gradient guides surface contraction waves in oocytes. *Nat Commun* 8, 849.
- Brown, E.B., Wu, E.S., Zipfel, W., and Webb, W.W. (1999). Measurement of Molecular Diffusion in Solution by Multiphoton Fluorescence Photobleaching Recovery. *Biophysical Journal* 77, 2837-2849.

- Carroll, N.J., Jensen, K.H., Parsa, S., Holbrook, N.M., and Weitz, D.A. (2014). Measurement of flow velocity and inference of liquid viscosity in a microfluidic channel by fluorescence photobleaching. *Langmuir* 30, 4868-4874.
- Chang, J.B., and Ferrell, J.E., Jr. (2013). Mitotic trigger waves and the spatial coordination of the *Xenopus* cell cycle. *Nature* 500, 603-607.
- Charras, G.T., Yarrow, J.C., Horton, M.A., Mahadevan, L., and Mitchison, T.J. (2005). Non-equilibration of hydrostatic pressure in blebbing cells. *Nature* 435, 365-369.
- Collins, S.R., Yang, H.W., Bonger, K.M., Guignet, E.G., Wandless, T.J., and Meyer, T. (2015). Using light to shape chemical gradients for parallel and automated analysis of chemotaxis. *Mol Syst Biol* 11, 804.
- Cooke, J., and Zeeman, E.C. (1976). A clock and wavefront model for control of the number of repeated structures during animal morphogenesis. *J Theor Biol* 58, 455-476.
- Cordeiro, J.V., and Jacinto, A. (2013). The role of transcription-independent damage signals in the initiation of epithelial wound healing. *Nat Rev Mol Cell Biol* 14, 249-262.
- Dashkevich, N.M., Ovanesov, M.V., Balandina, A.N., Karamzin, S.S., Shestakov, P.I., Soshitova, N.P., Tokarev, A.A., Pantelev, M.A., and Ataullakhanov, F.I. (2012). Thrombin activity propagates in space during blood coagulation as an excitation wave. *Biophys J* 103, 2233-2240.
- Deneke, V.E., and Di Talia, S. (2018). Chemical waves in cell and developmental biology. *J Cell Biol* 217, 1193-1204.
- Deneke, V.E., Melbinger, A., Vergassola, M., and Di Talia, S. (2016). Waves of Cdk1 Activity in S Phase Synchronize the Cell Cycle in *Drosophila* Embryos. *Dev Cell* 38, 399-412.
- Deneke, V.E., Puliafito, A., Krueger, D., Narla, A., De Simone, A., Primo, L., Vergassola, M., De Renzis, S., and Di Talia, S. (2019). Self-organized nuclear positioning synchronizes the cell cycle in *Drosophila* embryos. *Cell*, in press.
- Devreotes, P.N., Bhattacharya, S., Edwards, M., Iglesias, P.A., Lampert, T., and Miao, Y. (2017). Excitable Signal Transduction Networks in Directed Cell Migration. *Annu Rev Cell Dev Biol* 33, 103-125.

- Di Talia, S., She, R., Blythe, S.A., Lu, X., Zhang, Q.F., and Wieschaus, E.F. (2013). Posttranslational control of Cdc25 degradation terminates drosophila's early cell-cycle program. *Current Biology* 23, 127-132.
- Di Talia, S., and Wieschaus, E.F. (2012). Short-term integration of Cdc25 dynamics controls mitotic entry during *Drosophila* gastrulation. *Developmental cell* 22, 763-774.
- Edgar, B.A., Kiehle, C.P., and Schubiger, G. (1986). Cell cycle control by the nucleocytoplasmic ratio in early *Drosophila* development. *Cell* 44, 365-372.
- Edgar, B.A., Sprenger, F., Duronio, R.J., Leopold, P., and O'Farrell, P.H. (1994). Distinct molecular mechanisms regulate cell cycle timing at successive stages of *Drosophila* embryogenesis. *Genes & development* 8, 440-452.
- El-Sherif, E., Zhu, X., Fu, J., and Brown, S.J. (2014). Caudal Regulates the Spatiotemporal Dynamics of Pair-Rule Waves in *Tribolium*. *PLoS Genetics* 10, e1004677.
- Falahati, H., and Wieschaus, E. (2017). Independent active and thermodynamic processes govern the nucleolus assembly in vivo. *Proc Natl Acad Sci U S A* 114, 1335-1340.
- Farrell, J.A., and O'Farrell, P.H. (2013). Mechanism and regulation of Cdc25/twine protein destruction in embryonic cell-cycle remodeling. *Current Biology* 23, 118-126.
- Farrell, J.A., and O'Farrell, P.H. (2014). From egg to gastrula: how the cell cycle is remodeled during the *Drosophila* mid-blastula transition. *Annual review of genetics* 48, 269-294.
- Farrell, J.A., Shermoen, A.W., Yuan, K., and O'Farrell, P.H. (2012). Embryonic onset of late replication requires Cdc25 down-regulation. *Genes & development* 26, 714-725.
- Fasulo, B., Koyama, C., Yu, K.R., Homola, E.M., Hsieh, T.S., Campbell, S.D., and Sullivan, W. (2012). Chk1 and Wee1 kinases coordinate DNA replication, chromosome condensation, and anaphase entry. *Molecular Biology of the Cell* 23, 1047-1057.
- Ferree, P.L., Deneke, V.E., and Di Talia, S. (2016). Measuring time during early embryonic development. *Semin Cell Dev Biol* 55, 80-88.
- Ferrell, J.E., Jr., and Ha, S.H. (2014). Ultrasensitivity part III: cascades, bistable switches, and oscillators. *Trends Biochem Sci* 39, 612-618.

- Field, C.M., Wuhr, M., Anderson, G.A., Kueh, H.Y., Strickland, D., and Mitchison, T.J. (2011). Actin behavior in bulk cytoplasm is cell cycle regulated in early vertebrate embryos. *J Cell Sci* 124, 2086-2095.
- Fisher, R.A. (1937). The wave of advance of advantageous genes. *Annals of Eugenics* 7, 355-369.
- Foe, V.E., and Alberts, B.M. (1983). Studies of nuclear and cytoplasmic behaviour during the five mitotic cycles that precede gastrulation in *Drosophila* embryogenesis. *J Cell Sci* 61, 31-70.
- Foe, V.E.O., G.M.; Edgar, B.A. (1993). Mitosis and morphogenesis in the *Drosophila* embryo : point and counterpoint. In *The Development of Drosophila melanogaster* (Cold Spring Harbor Laboratory Press), pp. 149-300.
- Fogarty, P., Campbell, S.D., Abu-Shumays, R., Phalle, B.d.S., Yu, K.R., Uy, G.L., Goldberg, M.L., and Sullivan, W. (1997). The *Drosophila* grapes gene is related to checkpoint gene *chk1/rad27* and is required for late syncytial division fidelity. *Current Biology* 7, 418-426.
- Gavet, O., and Pines, J. (2010a). Activation of cyclin B1-Cdk1 synchronizes events in the nucleus and the cytoplasm at mitosis. *J Cell Biol* 189, 247-259.
- Gavet, O., and Pines, J. (2010b). Progressive Activation of CyclinB1-Cdk1 Coordinates Entry to Mitosis. *Developmental Cell* 18, 533-543.
- Gelens, L., Anderson, G.A., and Ferrell, J.J.E. (2014). Spatial trigger waves: positive feedback gets you a long way. *Molecular biology of the cell* 25, 3486-3493.
- Gilmour, D., Rembold, M., and Leptin, M. (2017). From morphogen to morphogenesis and back. *Nature* 541, 311-320.
- Goldstein, R.E., and van de Meent, J.W. (2015). A physical perspective on cytoplasmic streaming. *Interface Focus* 5, 20150030.
- Gomez, C., Ozbudak, E.M., Wunderlich, J., Baumann, D., Lewis, J., and Pourquie, O. (2008). Control of segment number in vertebrate embryos. *Nature* 454, 335-339.

- Graham, C.F., and Morgan, R.W. (1966). Changes in the cell cycle during early amphibian development. *Developmental Biology* 14, 439-460.
- Grallert, A., Boke, E., Hagting, A., Hodgson, B., Connolly, Y., Griffiths, J.R., Smith, D.L., Pines, J., and Hagan, I.M. (2015). A PP1-PP2A phosphatase relay controls mitotic progression. *Nature* 517, 94-98.
- Gregor, T., Fujimoto, K., Masaki, N., and Sawai, S. (2010). The onset of collective behavior in social amoebae. *Science* 328, 1021-1025.
- Gross, P., Kumar, K.V., and Grill, S.W. (2017). How Active Mechanics and Regulatory Biochemistry Combine to Form Patterns in Development. *Annu Rev Biophys* 46, 337-356.
- Hara, K. (1971). Cinematographic observation of "surface contraction waves" (SCW) during the early cleavage of axolotl eggs. *Wilhelm Roux Arch Entwickl Mech Org* 167, 183-186.
- Harvey, S.L., Enciso, G., Dephoure, N., Gygi, S.P., Gunawardena, J., and Kellogg, D.R. (2011). A phosphatase threshold sets the level of Cdk1 activity in early mitosis in budding yeast. *Molecular biology of the cell* 22, 3595-3608.
- Hatanaka, K., and Okada, M. (1991). Retarded nuclear migration in *Drosophila* embryos with aberrant F-actin reorganization caused by maternal mutations and by cytochalasin treatment. *Development* 111, 909-920.
- Heim, A., Rymarczyk, B., and Mayer, T.U. (2017). Regulation of Cell Division. In *Vertebrate Development: Maternal to Zygotic Control*, F. Pelegri, M. Danilchik, and A. Sutherland, eds. (Cham: Springer International Publishing), pp. 83-116.
- Hiratsuka, T., Fujita, Y., Naoki, H., Aoki, K., Kamioka, Y., and Matsuda, M. (2015). Intercellular propagation of extracellular signal-regulated kinase activation revealed by in vivo imaging of mouse skin. *Elife* 4, e05178.
- Hodgkin, A.L., and Huxley, A.F. (1952). A quantitative description of membrane current and its application to conduction and excitation in nerve. *J Physiol* 117, 500-544.
- Holt, L.J., Krutchinsky, A.N., and Morgan, D.O. (2008). Positive feedback sharpens the anaphase switch. *Nature* 454, 353-357.

- Huang, J., and Raff, J.W. (1999). The disappearance of cyclin B at the end of mitosis is regulated spatially in *Drosophila* cells. *The EMBO Journal* 18, 2184-2195.
- Hubaud, A., and Pourquie, O. (2014). Signalling dynamics in vertebrate segmentation. *Nat Rev Mol Cell Biol* 15, 709-721.
- Hubaud, A., Regev, I., Mahadevan, L., and Pourquie, O. (2017). Excitable Dynamics and Yap-Dependent Mechanical Cues Drive the Segmentation Clock. *Cell*.
- Idema, T., Dubuis, J.O., Kang, L., Manning, M.L., Nelson, P.C., Lubensky, T.C., and Liu, A.J. (2013). The syncytial *Drosophila* embryo as a mechanically excitable medium. *PLoS One* 8, e77216.
- Inagaki, N., and Katsuno, H. (2017). Actin Waves: Origin of Cell Polarization and Migration? *Trends Cell Biol* 27, 515-526.
- Ishihara, K., Nguyen, P.A., Wühr, M., Groen, A.C., Field, C.M., and Mitchison, T.J. (2014). Organization of early frog embryos by chemical waves emanating from centrosomes. *Philosophical transactions of the Royal Society of London Series B, Biological sciences* 369.
- Izquierdo, E., Quinkler, T., and De Renzis, S. (2018). Guided morphogenesis through optogenetic activation of Rho signalling during early *Drosophila* embryogenesis. *Nat Commun* 9, 2366.
- Jackman, M., Pines, J., Nigg, E.A., and Lindon, C. (2003). Active cyclin B1-Cdk1 first appears on centrosomes in prophase. *Nature Cell Biology* 5, 143-148.
- Jiang, Y.J., Aerne, B.L., Smithers, L., Haddon, C., Ish-Horowicz, D., and Lewis, J. (2000). Notch signalling and the synchronization of the somite segmentation clock. *Nature* 408, 475-479.
- Kamino, K., Fujimoto, K., and Sawai, S. (2011). Collective oscillations in developing cells: insights from simple systems. *Dev Growth Differ* 53, 503-517.
- Kane, D.A., and Kimmel, C.B. (1993). The zebrafish midblastula transition. *Development* 119, 447-456.
- Karsenti, E. (2008). Self-organization in cell biology: a brief history. *Nat Rev Mol Cell Biol* 9, 255-262.

- Kimmel, C.B., Ballard, W.W., Kimmel, S.R., Ullmann, B., and Schilling, T.F. (1995). Stages of embryonic development of the zebrafish. *Dev Dyn* 203, 253-310.
- Kirchner, J., Gross, S., Bennett, D., and Alphey, L. (2007). Essential, overlapping and redundant roles of the *Drosophila* protein phosphatase 1 alpha and 1 beta genes. *Genetics* 176, 273-281.
- Kolmogorov, A.N. (1991). Selected works of A.N. Kolmogorov (Dordrecht ; Boston: Kluwer Academic).
- Kondo, S., and Miura, T. (2010). Reaction-diffusion model as a framework for understanding biological pattern formation. *Science* 329, 1616-1620.
- Kuramoto, Y. (1986). *Chemical Oscillations, Waves, and Turbulence*. Springer-Verlag 1984 66, 296-296.
- Laughlin, R.B. (2015). Critical waves and the length problem of biology. *Proc Natl Acad Sci U S A* 112, 10371-10376.
- Lauschke, V.M., Tsiairis, C.D., Francois, P., and Aulehla, A. (2013). Scaling of embryonic patterning based on phase-gradient encoding. *Nature* 493, 101-105.
- Lee, J., Kumagai, A., and Dunphy, W.G. (2001). Positive regulation of Wee1 by Chk1 and 14-3-3 proteins. *Molecular Biology of the Cell* 12, 551-563.
- Lindner, B., García-Ojalvo, J., Neiman, A., and Schimansky-Geier, L. (2004). Effects of noise in excitable systems. *Physics Reports* 392, 321-424.
- Lippincott-Schwartz, J., Snapp, E., and Kenworthy, A. (2001). Studying protein dynamics in living cells. *Nat Rev Mol Cell Biol* 2, 444-456.
- López-Avilés, S., Novák, B., Uhlmann, F., and Kapuy, O. (2009). Irreversibility of mitotic exit is the consequence of systems-level feedback. *Nature* 459, 592-595.
- Luther, R. (1906). Raumlliche fortplanzung chimischer reaktionen. *Z Elektrochemie* 12, 596-600.

- Machacek, M., Hodgson, L., Welch, C., Elliott, H., Pertz, O., Nalbant, P., Abell, A., Johnson, G.L., Hahn, K.M., and Danuser, G. (2009). Coordination of Rho GTPase activities during cell protrusion. *Nature* 461, 99-103.
- Maitre, J.L., Turlier, H., Illukkumbura, R., Eismann, B., Niwayama, R., Nedelec, F., and Hiiragi, T. (2016). Asymmetric division of contractile domains couples cell positioning and fate specification. *Nature* 536, 344-348.
- Maroto, M., Dale, J.K., Dequeant, M.L., Petit, A.C., and Pourquie, O. (2005). Synchronised cycling gene oscillations in presomitic mesoderm cells require cell-cell contact. *Int J Dev Biol* 49, 309-315.
- Martins, T., Kotadia, S., Malmanche, N., Sunkel, C.E., and Sullivan, W. (2013). Strategies for outcrossing and genetic manipulation of *Drosophila* compound autosome stocks. *G3* 3, 1-4.
- Masamizu, Y., Ohtsuka, T., Takashima, Y., Nagahara, H., Takenaka, Y., Yoshikawa, K., Okamura, H., and Kageyama, R. (2006). Real-time imaging of the somite segmentation clock: revelation of unstable oscillators in the individual presomitic mesoderm cells. *Proc Natl Acad Sci U S A* 103, 1313-1318.
- Mayer, M., Depken, M., Bois, J.S., Julicher, F., and Grill, S.W. (2010). Anisotropies in cortical tension reveal the physical basis of polarizing cortical flows. *Nature* 467, 617-621.
- McClelland, M.L., Farrell, J.A., and O'Farrell, P.H. (2009). Influence of Cyclin Type and Dose on Mitotic Entry and Progression in the Early *Drosophila* Embryo. *The Journal of Cell Biology* 184, 639-646.
- Meinhardt, H. (1982). *Models of biological pattern formation* (London ; New York: Academic Press).
- Merrill, P.T., Sweeton, D., and Wieschaus, E. (1988). Requirements for autosomal gene activity during precellular stages of *Drosophila melanogaster*. *Development* 104, 495-509.
- Mitchison, T.J., Charras, G.T., and Mahadevan, L. (2008). Implications of a poroelastic cytoplasm for the dynamics of animal cell shape. *Semin Cell Dev Biol* 19, 215-223.
- Miyawaki, A. (2011). Proteins on the move: insights gained from fluorescent protein technologies. *Nat Rev Mol Cell Biol* 12, 656-668.

- Mochida, S., Maslen, S.L., Skehel, M., and Hunt, T. (2010). Greatwall phosphorylates an inhibitor of protein phosphatase 2A that is essential for mitosis. *Science* 330, 1670-1673.
- Mogilner, A., and Manhart, A. (2018). Intracellular Fluid Mechanics: Coupling Cytoplasmic Flow with Active Cytoskeletal Gel. *Annual Review of Fluid Mechanics* 50, 347-370.
- Morgan, D.O. (2007). *The cell cycle: principles of control* (Sunderland, MA; London: Published by New Science Press in association with Oxford University Press; Distributed inside North America by Sinauer Associates, Publishers).
- Munjal, A., Philippe, J.M., Munro, E., and Lecuit, T. (2015). A self-organized biomechanical network drives shape changes during tissue morphogenesis. *Nature* 524, 351-355.
- Murray, J.D. (2002). *Mathematical biology* (New York: Springer).
- Newman, S.M., and Schubiger, G. (1980). A morphological and developmental study of *Drosophila* embryos ligated during nuclear multiplication. *Developmental Biology* 79, 128-138.
- Novak, B., and Tyson, J.J. (1993). Modeling the Cell Division Cycle: M-phase Trigger, Oscillations, and Size Control. *Journal of Theoretical Biology* 165, 101-134.
- O'Farrell, P.H. (2015). Growing an Embryo from a Single Cell: A Hurdle in Animal Life. *Cold Spring Harb Perspect Biol* 7.
- O'Farrell, P.H., Stumpff, J., and Su, T.T. (2004). Embryonic cleavage cycles: how is a mouse like a fly? *Current biology* : CB 14, R35-R45.
- Oates, A.C., Morelli, L.G., and Ares, S. (2012). Patterning embryos with oscillations: structure, function and dynamics of the vertebrate segmentation clock. *Development* 139, 625-639.
- Ogura, Y., and Sasakura, Y. (2016). Developmental Control of Cell-Cycle Compensation Provides a Switch for Patterned Mitosis at the Onset of Chordate Neurulation. *Dev Cell* 37, 148-161.

- Ogura, Y., and Sasakura, Y. (2017). Emerging mechanisms regulating mitotic synchrony during animal embryogenesis. *Dev Growth Differ.*
- Pancieria, T., Azzolin, L., Cordenonsi, M., and Piccolo, S. (2017). Mechanobiology of YAP and TAZ in physiology and disease. *Nat Rev Mol Cell Biol* 18, 758-770.
- Pandit, S.V., and Jalife, J. (2013). Rotors and the dynamics of cardiac fibrillation. *Circ Res* 112, 849-862.
- Perry, J.A., and Kornbluth, S. (2007). Cdc25 and Wee1: analogous opposites? *Cell division* 2, 12.
- Pomerening, J.R., Kim, S.Y., and Ferrell, J.E. (2005). Systems-Level Dissection of the Cell-Cycle Oscillator: Bypassing Positive Feedback Produces Damped Oscillations. *Cell* 122, 565-578.
- Price, D., Rabinovitch, S., O'Farrell, P.H., and Campbell, S.D. (2000). *Drosophila wee1* Has an Essential Role in the Nuclear Divisions of Early Embryogenesis. *Genetics* 155, 159-166.
- Quinlan, M.E. (2016). Cytoplasmic Streaming in the *Drosophila* Oocyte. *Annu Rev Cell Dev Biol* 32, 173-195.
- Rabinowitz, M. (1941). Studies on the cytology and early embryology of the egg of *Drosophila melanogaster*. *Journal of Morphology* 69, 1-49.
- Rankin, S., and Kirschner, M.W. (1997). The surface contraction waves of *Xenopus* eggs reflect the metachronous cell-cycle state of the cytoplasm. *Curr Biol* 7, 451-454.
- Regot, S., Hughey, J.J., Bajar, B.T., Carrasco, S., and Covert, M.W. (2014). High-sensitivity measurements of multiple kinase activities in live single cells. *Cell* 157, 1724-1734.
- Riedel-Kruse, I.H., Muller, C., and Oates, A.C. (2007). Synchrony dynamics during initiation, failure, and rescue of the segmentation clock. *Science* 317, 1911-1915.
- Rodrigues, F.A., Peron, T.K.D.M., Ji, P., and Kurths, J. (2016). The Kuramoto model in complex networks. *Physics Reports* 610, 1-98.
- Roignant, J.Y., and Treisman, J.E. (2009). Pattern formation in the *Drosophila* eye disc. *Int J Dev Biol* 53, 795-804.

- Roman, W., and Gomes, E.R. (2018). Nuclear positioning in skeletal muscle. *Semin Cell Dev Biol* 82, 51-56.
- Royou, A., McCusker, D., Kellogg, D.R., and Sullivan, W. (2008). Grapes(Chk1) Prevents Nuclear CDK1 Activation by Delaying Cyclin B Nuclear Accumulation. *The Journal of Cell Biology* 183, 63-75.
- Royou, A., Sullivan, W., and Karess, R. (2002). Cortical recruitment of nonmuscle myosin II in early syncytial *Drosophila* embryos: its role in nuclear axial expansion and its regulation by Cdc2 activity. *J Cell Biol* 158, 127-137.
- Samarage, C.R., White, M.D., Alvarez, Y.D., Fierro-Gonzalez, J.C., Henon, Y., Jesudason, E.C., Bissiere, S., Fouras, A., and Plachta, N. (2015). Cortical Tension Allocates the First Inner Cells of the Mammalian Embryo. *Dev Cell* 34, 435-447.
- Sander, K. (1971). Pattern formation in longitudinal halves of leaf hopper eggs (Homoptera) and some remarks on the definition of "Embryonic regulation". *Wilhelm Roux Archiv für Entwicklungsmechanik der Organismen* 167, 336-352.
- Serra-Picamal, X., Conte, V., Vincent, R., Ester, Tambe, D.T., Bazellieres, E., Butler, J.P., Fredberg, J.J., and Trepap, X. (2012). Mechanical waves during tissue expansion. *Nature Physics* 8, 628-634.
- Shermoen, A.W., McClelland, M.L., and O'Farrell, P.H. (2010). Developmental Control of Late Replication and S Phase Length. *Current Biology* 20, 2067-2077.
- Shimojo, H., and Kageyama, R. (2016). Making Waves toward the Shore by Synchronicity. *Dev Cell* 36, 358-359.
- Shinagawa, A., Konno, S., Yoshimoto, Y., and Hiramoto, Y. (1989). Nuclear Involvement in Localization of the Initiation Site of Surface Contraction Waves in *Xenopus* Eggs. *Development, Growth & Differentiation* 31, 249-255.
- Sibon, O.C., Stevenson, V.A., and Theurkauf, W.E. (1997). DNA-replication checkpoint control at the *Drosophila* midblastula transition. *Nature* 388, 93-97.
- Siebert, F., and Weijer, C.J. (1995). Spiral and concentric waves organize multicellular *Dictyostelium* mounds. *Curr Biol* 5, 937-943.

Soroldoni, D., Jorg, D.J., Morelli, L.G., Richmond, D.L., Schindelin, J., Julicher, F., and Oates, A.C. (2014). Genetic oscillations. A Doppler effect in embryonic pattern formation. *Science* 345, 222-225.

Stricker, S.A. (1999). Comparative biology of calcium signaling during fertilization and egg activation in animals. *Dev Biol* 211, 157-176.

Strogatz, S.H. (2000a). From Kuramoto to Crawford: exploring the onset of synchronization in populations of coupled oscillators. *Physica D: Nonlinear Phenomena* 143, 1-20.

Strogatz, S.H. (2000b). *Nonlinear dynamics and chaos : with applications to physics, biology, chemistry, and engineering* (Cambridge, MA: Westview Press).

Stumpff, J., Duncan, T., Homola, E., Campbell, S.D., and Su, T.T. (2004). *Drosophila Wee1 Kinase Regulates Cdk1 and Mitotic Entry during Embryogenesis*. *Current Biology* 14, 2143-2148.

Su, T.T., Sprenger, F., DiGregorio, P.J., Campbell, S.D., and O'Farrell, P.H. (1998). Exit from mitosis in *Drosophila* syncytial embryos requires proteolysis and cyclin degradation, and is associated with localized dephosphorylation. *Genes Dev* 12, 1495-1503.

Suel, G.M., Garcia-Ojalvo, J., Liberman, L.M., and Elowitz, M.B. (2006). An excitable gene regulatory circuit induces transient cellular differentiation. *Nature* 440, 545-550.

Swaminathan, R., Hoang, C.P., and Verkman, A.S. (1997). Photobleaching recovery and anisotropy decay of green fluorescent protein GFP-S65T in solution and cells: cytoplasmic viscosity probed by green fluorescent protein translational and rotational diffusion. *Biophys J* 72, 1900-1907.

Takada, S., Kwak, S., Koppetsch, B.S., and Theurkauf, W.E. (2007). *grp (chk1)* replication-checkpoint mutations and DNA damage trigger a Chk2-dependent block at the *Drosophila* midblastula transition. *Development* 134, 1737-1744.

Tanaka, H., Stone, H.A., and Nelson, D.R. (2017). Spatial gene drives and pushed genetic waves. *Proc Natl Acad Sci U S A* 114, 8452-8457.

Tsai, T.Y., Theriot, J.A., and Ferrell, J.E., Jr. (2014). Changes in oscillatory dynamics in the cell cycle of early *Xenopus laevis* embryos. *PLoS Biol* 12, e1001788.

- Tsaiiris, C.D., and Aulehla, A. (2016). Self-Organization of Embryonic Genetic Oscillators into Spatiotemporal Wave Patterns. *Cell* 164, 656-667.
- Turing, A.M. (1952). The chemical basis of morphogenesis. *Philosophical Transactions of the Royal Society of London Series B, Biological Sciences* 237, 37.
- Tyson, J.J., and Keener, J.P. (1988). Singular Perturbation Theory of Spiral Waves in Excitable Media. *Physica D* 32.
- van Saarloos, W. (1998). Three basic issues concerning interface dynamics in nonequilibrium pattern formation. *Physics Reports* 301, 9-43.
- van Saarloos, W. (2003). Front propagation into unstable states. *Physics Reports* 386, 29-222.
- Vergassola, M., Deneke, V.E., and Di Talia, S. (2018). Mitotic waves in the early embryogenesis of *Drosophila*: Bistability traded for speed. *Proc Natl Acad Sci U S A* 115, E2165-E2174.
- Vicker, M.G., and Grutsch, J.F. (2008). Dual chemotaxis signalling regulates *Dictyostelium* development: intercellular cyclic AMP pulses and intracellular F-actin disassembly waves induce each other. *Eur J Cell Biol* 87, 845-861.
- Viktorinova, I., Konig, T., Schlichting, K., and Dahmann, C. (2009). The cadherin Fat2 is required for planar cell polarity in the *Drosophila* ovary. *Development* 136, 4123-4132.
- von Dassow, G., and Schubiger, G. (1994). How an actin network might cause fountain streaming and nuclear migration in the syncytial *Drosophila* embryo. *J Cell Biol* 127, 1637-1653.
- Wang, J., Han, X., and Zhang, Y. (2012). Autoregulatory Mechanisms of Phosphorylation of Checkpoint Kinase 1. *Cancer Research* 72, 3786-3794.
- Weiner, O.D., Marganski, W.A., Wu, L.F., Altschuler, S.J., and Kirschner, M.W. (2007). An actin-based wave generator organizes cell motility. *PLoS Biol* 5, e221.
- Weissleder, R., and Nahrendorf, M. (2015). Advancing biomedical imaging. *Proc Natl Acad Sci U S A* 112, 14424-14428.

- Winfree, A.T. (1972). Spiral waves of chemical activity. *Science* 175, 634-636.
- Winfree, A.T. (2001). *The geometry of biological time*, Vol 12.;12; (New York: Springer).
- Woodhouse, F.G., and Goldstein, R.E. (2013). Cytoplasmic streaming in plant cells emerges naturally by microfilament self-organization. *Proc Natl Acad Sci U S A* 110, 14132-14137.
- Wu, J.Q., Guo, J.Y., Tang, W., Yang, C.S., Freel, C.D., Chen, C., Nairn, A.C., and Kornbluth, S. (2009). PP1-mediated dephosphorylation of phosphoproteins at mitotic exit is controlled by inhibitor-1 and PP1 phosphorylation. *Nat Cell Biol* 11, 644-651.
- Xiao, S., Tong, C., Yang, Y., and Wu, M. (2017). Mitotic Cortical Waves Predict Future Division Sites by Encoding Positional and Size Information. *Dev Cell* 43, 493-506 e493.
- Xu, S., and Chisholm, A.D. (2011). A Galphaq-Ca(2)(+) signaling pathway promotes actin-mediated epidermal wound closure in *C. elegans*. *Curr Biol* 21, 1960-1967.
- Yang, H.W., Collins, S., and Meyer, T. (2016). Locally excitable Cdc42 signals steer cells during chemotaxis. *Nat Cell Biol* 18, 191-201.
- Yohn, C.B., Pusateri, L., Barbosa, V., and Lehmann, R. (2003). l(3)malignant brain tumor and three novel genes are required for *Drosophila* germ-cell formation. *Genetics* 165, 1889-1900.
- Yuan, K., Farrell, J.A., and O'Farrell, P.H. (2012). Different cyclin types collaborate to reverse the S-phase checkpoint and permit prompt mitosis. *Journal of Cell Biology* 198, 973-980.
- Zalokar, M., and Erk, I. (1976). Division and migration of nuclei during early embryogenesis of *Drosophila melanogaster*, Vol 25.
- Zhabotinsky, A.M. (1964). Periodic course of oxidation of malonic acid in solution (investigation of the kinetics of the reaction of Belousov), Vol 9.
- Zhang, Y., and Hunter, T. (2014). Roles of Chk1 in cell biology and cancer therapy. *International Journal of Cancer* 134, 1013-1023.

Biography

Victoria E. Deneke completed her undergraduate degree in Chemical Engineering at the University of Notre Dame in May of 2013. In August 2013, she began her Ph.D. studies at Duke University under the Program in Cell and Molecular Biology (CMB). In summer of 2014 she joined the Di Talia lab and affiliated with the Department of Cell Biology.

During her time at Duke, she has been the recipient of several academic fellowships and honors, including: HHMI International Student Research Fellowship (2016), Schlumberger Faculty for the Future Fellowship (2015), Duke BioCoRE Scholar (2013), Boehringer Ingelheim Fonds Travel Grant (2018), JCB Norton B. Gilula Travel Award (2018), Journal of Developmental Biology Travel Award (2018), ASCB Travel Award (2017), and Duke Regeneration Next Travel Award (2017). Victoria was also one of the co-founders of Duke INSPIRE.

In the Di Talia lab, Victoria was the first author of 2 research publications and 2 reviews articles: “Measuring time during early embryonic development” published in *Seminars in Cell and Developmental Biology* in July 2016, “Waves of Cdk1 activity in S-phase synchronize the cell cycle in *Drosophila* embryos” published in *Developmental Cell* in August 2016, “Chemical Waves in Cell and Developmental Biology” published in *Journal of Cell Biology* in January of 2018, and “Self-organized nuclear positioning synchronizes the cell cycle in *Drosophila* embryos” accepted in *Cell* in March 2019.

Victoria also contributed to the publication “Mitotic waves in the early embryogenesis of *Drosophila*: bistability traded for speed” published in *Proceedings of the National Academy of Sciences* in February 2018.